E.O. Paton Electric Welding Institute of the National Academy of Science of Ukraine
International Association “Welding”

The Paton Welding Journal

12
2024

International Scientific-Technical and Production Journal ♦ Founded in January 2000 (12 Issues Per Year)

EDITORIAL BOARD

Editor-in-Chief
Igor Krivtsun
E.O. Paton Electric Welding Institute of the NASU, Kyiv, Ukraine

Deputy Editor-in-Chief
Michael Gasik
Aalto University, Espoo, Finland

Deputy Editor-in-Chief
Jacob Kleiman
Integrity Testing Laboratory, Markham, Canada

Editorial Board Members

Serhii Akhonin
E.O. Paton Electric Welding Institute of the NASU, Kyiv, Ukraine

Chunlin Dong
Guangzhou Jiao Tong University, China

Shiyi Gao
China-Ukraine Institute of Welding,
Guangdong Academy of Sciences, Guangzhou, China

Len Gelman
The University of Huddersfield, UK

Andrey Gumenyuk
Bundesanstalt für Materialforschung und –prüfung (BAM),
Berlin, Germany

Vitalii Knysh
E.O. Paton Electric Welding Institute of the NASU, Kyiv, Ukraine

Volodymyr Korzhyk
E.O. Paton Electric Welding Institute of the NASU, Kyiv, Ukraine

Victor Kvasnytskyi
NTUU «Igor Sikorsky Kyiv Polytechnic Institute», Ukraine

Yuliia Kvasnytska
Physico-Technological Institute of Metals and Alloys
of the NASU, Kyiv, Ukraine

Leonid Lobanov
E.O. Paton Electric Welding Institute of the NASU, Kyiv, Ukraine

Eric Macdonald
The University of Texas at El Paso, USA

Anatoliy Maistrenko
V. Bakul Institute for Superhard Materials
of the NASU, Kyiv, Ukraine

Serhiy Maksymov
E.O. Paton Electric Welding Institute of the NASU, Kyiv, Ukraine

Dhanesh G. Mohan
School of Engineering University of Sunderland England,
United Kingdom

João Pedro Oliveira
Universidade NOVA de Lisboa, Portugal

Valerii Peremitko
Dniprovsky State Technical University, Kamianske, Ukraine

Valeriy Pozniakov
E.O. Paton Electric Welding Institute of the NASU, Kyiv, Ukraine

Uwe Reisgen
Welding and Joining Institute, Aachen, Germany

Massimo Rogante
Rogante Engineering, Civitanova Marche, Italy

Cezary Senderowski
Mechanics and Printing Institute, Warsaw University
of Technology, Poland

Magdalena Speicher
Kempten University of Applied Sciences, Germany

Mattias Thuvander
Chalmers University of Technology, Goteborg, Sweden

Valentyn Uchanin
Karpenko Physico-Mechanical Institute of the NASU, Lviv, Ukraine

Gerald Wilhelm
University of Applied Sciences of Munich, Germany

Yongqiang Yang
South China University of Technology, Guangzhou, China

Executive Editor
Oleksandr Zelnichenko
International Association “Welding”, Kyiv, Ukraine

Address of Editorial Office
E.O. Paton Electric Welding Institute, 11 Kazymyr Malevych Str., 03150, Kyiv, Ukraine
Tel.: (38044) 205 23 90, E-mail: patonpublishinghouse@gmail.com; journal@paton.kiev.ua
https://patonpublishinghouse.com/eng/journals/tpwj

The Journal was registered by the National Council of Ukraine on Television and Radio Broadcasting on 09.05.2024, carrier identifier R30-04569. ISSN 0957-798X (Print), ISSN 3041-2293 (Online). DOI: http://dx.doi.org/10.37434/tpwj

Subscriptions, 12 issues per year:
348 Euro — annual subscription for the printed (hard copy) version, air postage and packaging included;
288 Euro — annual subscription for the electronic version (sending issues in pdf format or providing access to IP addresses).

Representative Offices of “The Paton Welding Journal”:

BRAZIL, Arc Dynamics
Address: Nova Iguacu, Rio de Janeiro, Brazil
Daniel Adolpho, Tel.: +55 21 9 6419 5703, E-mail: dadolpho@arcdynamics.com.br

BULGARIA, Bulgarian Welding Society
Address: Blvd. Asen Yordanov No.10, Sofia 1592, Bulgaria
Pavel Popgeorgiev, Tel.: +359 899 96 22 20, E-mail: office@bws-bg.org

CHINA, China-Ukraine Institute of Welding, Guangdong Academy of Sciences
Address: Room 210, No. 363 Changxing Road, Tianhe, Guangzhou, 510650, China
Zhang Yupeng, Tel.: +86-20-61086791, E-mail: patonjournal@gwi.gd.cn

POLAND, PATON EUROPE Sp. z o. o.
Address: ul. Kapitałowa 4, 35-213, Rzeszów, Poland
Anton Stepakhno, Tel.: +38067 509 95 67, E-mail: Anton.Stepakhno@paton.ua

The content of the Journal includes articles received from authors from around the world in the field of welding, cutting, cladding, soldering, brazing, coating, 3D additive technologies, electrometallurgy, material science, NDT and selectively includes translations into English of articles from the following journals, published in Ukrainian:

- «Avtomatychne Zvaryuvannya» (Automatic Welding), https://patonpublishinghouse.com/eng/journals/as;
- «Suchasna Elektrometalurhiya» (Electrometallurgy Today), https://patonpublishinghouse.com/eng/journals/sem;
- «Tekhnichna Diahnostyka ta Neruinivnyi Kontrol» (Technical Diagnostics & Nondestructive Testing), https://patonpublishinghouse.com/eng/journals/tdnk.

© E.O. Paton Electric Welding Institute of NASU, 2024
© International Association “Welding” (Publisher), 2024

CONTENTS

ORIGINAL ARTICLES

---

*Translated Article(s) from “Avtomatychne Zvaryuvannya” (Automatic Welding), No. 6, 2024.

**Translated Article(s) from “Tekhnichna Diahnostyka ta Neruinivnyi Kontrol” (Technical Diagnostics & Nondestructive Testing), No. 3, 2024.

***Translated Article(s) from “Tekhnichna Diahnostyka ta Neruinivnyi Kontrol” (Technical Diagnostics & Nondestructive Testing), No. 4, 2024.

Indexing: The electronic edition of the Journal is stored in the V.I. Vernadsky National Library of Ukraine (eVerLib), included in the OPEN UKRAINIAN CITATION INDEX database and international databases: CROSSREF, EBSCO, Google Scholar, INDEX COPERNICUS, IET Inspec, ULRICHSWEB.

DOI: https://doi.org/10.37434/tpwj2024.12.01

COATING FOR MEDICAL APPLICATION PRODUCED BY MICROPLASMA SPRAYING FROM Zr–Nb ALLOY

S.Yu. Maksymov[1], **S.G. Voinarovych**[1], **S.N. Kaliuzhnyi**[1], **O.N. Kyslytsia**[1],
I.S. Sviridova[1], **L. Alontseva**[2], **Ridvan Yamanoglu**[3]

[1]E.O. Paton Electric Welding Institute of the NASU
11 Kazymyr Malevych Str., 03150, Kyiv, Ukraine
[2]D. Serikbayev East Kazakhstan Technical University
19 Serikbayev Str., 070004, Ust-Kamenogorsk, Kazakhstan
[3]Department of Metallurgical and Materials Engineering,
Faculty of Engineering, Kocaeli University, Kocaeli 41001, Turkey

ABSTRACT

The work deals with the technology of microplasma spraying of biocompatible coatings from Zr–Nb alloy and their properties. On the surface of a porous Zr–Nb coating with the most developed surface microrelief, the presence of both open macropores of up to 300 μm in size and micropores of up to 10 μm in size was revealed. The X-ray phase analysis of the formed Zr–Nb coatings showed the presence of phases of α-solid solution of Zr, oxide (ZrO_2), nitride (ZrN) and carbide ($ZrNbC_2$). The corrosion resistance of a microplasma Zr–Nb coating and Ti6Al4V alloy in a solution of 0.9 % NaCl, which simulates the environment of the human body, was determined. It is assumed that Zr–Nb alloy coatings produced by microplasma spraying on the surfaces of existing Ti6Al4V alloy endoprostheses will allow for the future improvement in corrosion resistance and osseointegration between the bone and the implant.

KEYWORDS: microplasma spraying, biocompatible coating, Zr–Nb alloy, surface morphology, adhesion strength, corrosion resistance

INTRODUCTION

Currently, the titanium-based alloy of the Ti6A14V alloying system is the most widely used in the manufacture of orthopaedic implants [1]. However, the bioinertness of the surface of Ti6A14V alloy implants negatively affects the formation of a functional bonding between the implant and the bone [2]. In addition, long-term operation of Ti6A14V alloy implants in close contact with human bone and soft surrounding tissues leads to the release of alloying elements such as vanadium and aluminium and the manifestation of pathological reactions in the body. For example, aluminium interferes with bone mineralization, leading to structural deficiencies, while vanadium is highly cytotoxic and can cause allergic reactions [3].

Since the implant surface is the first to interact with the surrounding living tissue after implantation, the characteristics of the implant surface (such as its topography, hydrophilicity, roughness, etc.) play a dominant role both in the interaction of cells with the metal implant as well as in the subsequent processes of its osseointegration [4].

It is possible to increase the biocompatibility of existing Ti6A14V alloy implants by modifying their surface to provide appropriate functionality. Thus, applying coating on the implant surface is one of the most important technological techniques to provide the surface with chemical and physical properties that will contribute to the overall increase in the biocompatibility of the entire implanted product. Among the methods that are being actively researched and are becoming widespread in the application of biocompatible coatings from powders and wires, microplasma spraying (MPS) is distinguished [5, 6].

Zirconium-based alloys are increasingly being used as materials to improve the biocompatibility of implants due to their unique properties, such as the formation of an internal bone-like layer of apatite on their surface in the body, lower artefactuality in diagnostics by means of magnetic resonance imaging due to low magnetic susceptibility, as well as their excellent overall biocompatibility, high mechanical properties and corrosion resistance in body biological fluids [7, 8].

In addition to the chemical composition of the coating, the process of osseointegration is significantly influenced by the developed relief of its surface, the presence and size of open pores in the coating [9].

In [10], it is reported that a pore size of more than 100 μm is necessary for a successful bone formation process, while the recommended pore size should be about 300 μm. A similar pore size in the range of 200–400 μm is reported in [11] as a one promoting osteoblast adhesion, migration, and proliferation. The morphology of the surface microstructure also contributes to the conditions for cell adhesion on it. It was determined that microscale topography has a number of advantages. For example, the micron size of the open pores can improve the roughness and surface area, as well as increase the contact between the implant and the bone. This effect of interaction between the implant and the bone, as was shown by the research results, largely contributes to osseointegration. In addition, the microlevel topography can block and stabilise fibrin flow, which can attract osteoprogenitor cells to colonise at the implant-bone interface. Most importantly, microscale surface topography can improve initial cell adhesion and differentiation [12].

Thus, V.E. Li confirms that micro- and nanoroughness of the contacting surface with the bone work synergistically to increase the efficiency of osseointegration of orthopaedic implants [13]. The results of histological studies show that a rougher surface relief promotes osseointegration processes [14].

K. Matsuzaka evaluated the effect of implant surface on the proliferation of osteoblast-like cells and showed that cells are fixed on surfaces depending on their relief, and their predominant number was observed on protrusions over 5 μm [15].

It is also indicated in [16] that with an increase in the surface roughness of the coating from R_a = 3.7 μm to 56.1 μm, the bonding of a titanium implant with a bone tissue increases by 4 times (from 5.38 ± 1.96 to 21.63 ± 2.51 MPa, respectively).

At present, the recommended average surface roughness for titanium orthopaedic implants is in a wide range (0.07–100 μm) [17], but systematic study of the effect of surface roughness on biocompatibility was not conducted. The authors of [17] indicated that the optimal range of surface roughness of orthopaedic implants should be 20–25 μm. Although an increase in the roughness index improved the adhesion and cell proliferation on the surface of Ti13Nb13Zr alloy samples in their experiment, it also increased the areas with stress concentration, worsening the bending strength and contributing to the formation of cracks. In [18], it is noted that the high roughness R_a = = 118.19 ± 9.06 μm of the surface of orthopaedic titanium implants can interfere with cell proliferation. It is assumed that a decrease in the rate of cell proliferation on base samples with increased roughness may be the result of an unfavourable biological reaction to increased interaction with titanium. Thus, the poor osseointegration of titanium implants may be caused by the effect of titanium on the surrounding tissues.

The literature presents different approaches to the selection of the optimal range of surface roughness of orthopaedic implants. Accordingly, using the recommended indices of roughness, in the future it will be necessary to investigate the produced surfaces for biocompatibility.

Table 1. Limit values of the studied parameters of the MPS process of Zr–Nb coating

Parameters	max (+)	min (–)
Current I, A	26	16
Plasma-forming gas flow rate Q_m, l/h	240	160
Spraying distance H, mm	120	40
Wire feed rate V_w, m/min	4.8	2.9

THE AIM

of this work is to investigate the elemental composition of the surface of the coating applied by microplasma spraying of Zr–Nb alloy wire onto the Ti6A14V alloy base, its topography, index of corrosion resistance in the environment similar to the human body, and adhesion strength to the base.

MATERIALS, EQUIPMENT, AND EXPERIMENTAL PROCEDURES

The formation of Zr–Nb alloy coatings from a wire with a diameter of 0.3 mm was carried out on a set of the MPS-004 equipment for microplasma spraying [19] on samples of Ti6A14V alloy.

Previously, as a result of the analysis of the calculated feed rate of Zr–Nb alloy wire, the required amount of heat of the microplasma jet, and practical experience in producing biocompatible coatings in the MPS-004 installation, the limit values of the MPS mode parameters were determined (Table 1) for further study of their influence on the process of forming biocompatible coatings from Zr–Nb alloy.

When determining the limit values of the MPS technological parameters, it was taken into account that at a current below 16 A and a plasma gas flow rate of less than 160 l/h, the thermal and gas-dynamic characteristics of the jet would not be sufficient to ensure the melting process of a 0.3 mm diameter Zr–Nb wire with its stable dispersion [19]. Therefore, the criteria for the limit values of the mode parameters were also selected taking into account the possibility of ensuring of both spraying as well as coating formation processes.

X-ray diffraction studies and chemical analysis were performed in the D8 ADVANCE Bruker diffractometer (Bruker, USA). The coatings were scanned at a voltage of 30 kV and at a magnification of ×200.

The surface morphology of the formed coatings was studied by analysing the obtained images in the Philips SEM515 using BE+SE sensors, an acceleration voltage of 20 kV and an electrode heating current of 40 mA.

Photos of the 3D profiles of the coating surfaces were obtained by means of the Huvitz HDS-2520 optical profiler (Gyeonggi, Republic of Korea) with a resolution of ± 0.1 μm at optical magnification of

Table 2. Chemical composition of Zr–Nb coating surface produced at MPS parameters $I = 16$ A; $Q_m = 160$ l/h; $H = 40$ mm; $V_w = 2.9$ m/min

<table>
<tr><td rowspan="7">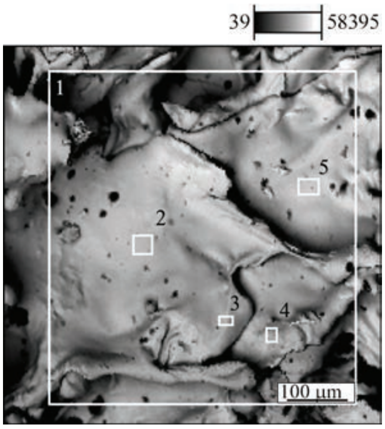 </td><td rowspan="2">Scanning area</td><td colspan="4">Content of chemical elements, at.%</td></tr>
<tr><td>Al</td><td>Ca</td><td>Zr</td><td>Nb</td></tr>
<tr><td>1</td><td>0.4</td><td>0.3</td><td>97.2 ± 0.9</td><td>2.1 ± 0.3</td></tr>
<tr><td>2</td><td>0.2</td><td>–</td><td>98.1 ± 0.8</td><td>1.7 ± 0.3</td></tr>
<tr><td>3</td><td>0.2</td><td>–</td><td>97.5 ± 0.8</td><td>2.3 ± 0.3</td></tr>
<tr><td>4</td><td>0.3</td><td>0.4 ± 0.1</td><td>97.5 ± 0.8</td><td>1.8 ± 0.3</td></tr>
<tr><td>5</td><td>0.2</td><td>–</td><td>97.7 ± 0.8</td><td>2.1 ± 0.3</td></tr>
</table>

×5, ×20, and ×50. The scanning area for each measurement was randomly selected to ensure reproducibility of the measurements and was approximately 700×500 µm^2. Area roughness parameters were chosen because they provide more informative values than line parameters.

The study of the 3D surface topography and the surface roughness parameter of the coatings over the area of 2D maps was carried out using Mountains® 9 software (Digital Surf, Besançon, France). The arithmetic mean deviation of the surface roughness profile (S_{α}) of the coatings was determined within a standard deviation of ± 0.1 µm in accordance with ISO 25178-2:2021.

The corrosion resistance of the coatings on 20×15×2 mm samples was studied for 1 h in a concentrated solution of 0.9 % NaCl with a concentration of ions close to human blood plasma. In the configuration of the electrical circuit, the samples under study acted as working electrodes, while the reference electrode was a platinum electrode. The Tafel extrapolation values were used to determine the corrosion current density (I_{corr}) and corrosion potential (E_{corr}). The polarisation curves were obtained in a solution of 0.9 % NaCl at 20 °C in the voltage range of –250–+250 mV and a scanning rate of 1 mV/s.

The adhesion strength of the coating to the base was determined using the static uniaxial tensile method in accordance with ASTM C633-13:2021. The number of tested coated samples was not less than 5 pcs. Tensile tests of each set of bonded sample assemblies were performed in a universal mechanical machine 2054 P-5 (SPC TechMash) at the same loading speed of 2 mm/min.

RESEARCH RESULTS AND DISCUSSION

The studies of the chemical composition of the surface of Zr–Nb coatings (Table 2) showed that they are similar to the initial material, which includes Zr, the average value of which is about 97.6 ± 0.82 at.% and Nb 2 ± 0.3 at.%, which corresponds to the industrial zirconium KTZ-125 alloy. Also, a small amount of Al and Ca was recorded, the content of which was less than 1 at.%, which can be considered as impurities in the composition of Zr–Nb alloy.

X-ray phase studies of Zr–Nb wire and surfaces of coated samples are presented in the form of X-ray diffraction patterns (Figure 1).

Comparing the X-ray diffraction patterns, it was found that complete melting of Zr–Nb wire in the microplasma jet and subsequent cooling of the dispersed particles on the surface of the base leads to the formation of coatings consisting of α-solid Zr solution with the presence of ZrO_2 oxide, ZrN nitride and $ZrNbC_2$ carbide inclusions.

The intensity of the peaks on the X-ray diffraction pattern and the similarity of the detected phases do not change with the variation of the MPS mode parameters and are observed on all coated samples. In terms of inclusion content in the coating, ZrO_2 phase prevails, which will further act as an inhibitor of the dissolution rate of the coating when it contacts with the surrounding fluids of the human body. The detected ZrN phase indicates the nitrogen saturation of

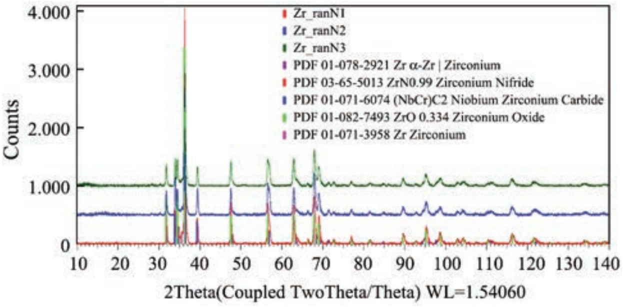

Figure 1. X-ray diffraction pattern of Zr–Nb coatings at MPS parameters: mode *1* — $I = 26$ A, $Q_m = 240$ l/h, $H = 120$ mm, $V_w = 4.8$ m/min; mode 2 — $I = 26$ A, $Q_m = 160$ l/h, $H = 40$ mm, $V_w = 4.8$ m/min; mode 3 — $I = 16$ A, $Q_m = 160$ l/h, $H = 40$ mm, $V_w = 2.9$ m/min

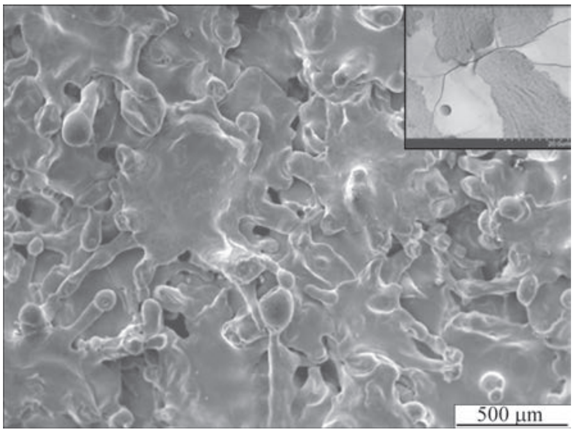

Figure 2. SEM morphology of Zr–Nb coating surface produced at MPS parameters $I = 16$ A; $Q_m = 160$ l/h; $H = 40$ mm; $V_w = 2.9$ m/min

the atomised particles when moving in the microplasma jet at a temperature of 670 K. This indicates that protection in the form of blowing a microplasma flux with atomised Zr particles by a stream of argon process gas is not sufficient to effectively separate them from atmospheric gases during coating formation. The presence of $ZrNbC_2$ inclusions in biocompatible coatings can contribute to an increase in the hardness of these coatings, but at the same time reduce their plasticity and adhesion strength to the base, as well as inclusions of oxides and nitrides.

It is known that both the size and pore content in the volume of the structure of Zr–Nb coatings as well as the microrelief of their surface layers are affected by the state and deformation of dispersed particles forming the coating, which in turn is determined by the parameters of the MPS mode [20]. The volume porosity content in the structure of Zr–Nb coatings was in the range of (2.8 ± 0.1) – (20.3 ± 2.0) %, while the highest volume porosity content in Zr–Nb coatings was formed on the mode with parameters $I = 16$ A; $Q_m = 160$ l/h; $H = 40$ mm; $V_w = 2.9$ m/min [20].

The study of the surface morphology of Zr–Nb coatings (Figure 2) showed that it is characterised by heterogeneity with many surface branches in the form of depressions and protrusions and open macropores of up to 300 ± 50 µm in size. Due to the dispersed particles, which were completely molten, Zr–Nb coatings were formed from disc-like splats. Due to the presence of residual stress in splats, the surface of Zr–Nb coatings had microcracks that formed due to rapid heat transfer and cooling processes. The formed cracks lead to the stress relaxation in the coating, while the porosity itself can be a way to reduce the modulus of elasticity of the coating and bring it closer to the bone, but it is also a dangerous factor that intensifies the degradation process at the interface between the coating and the base [21].

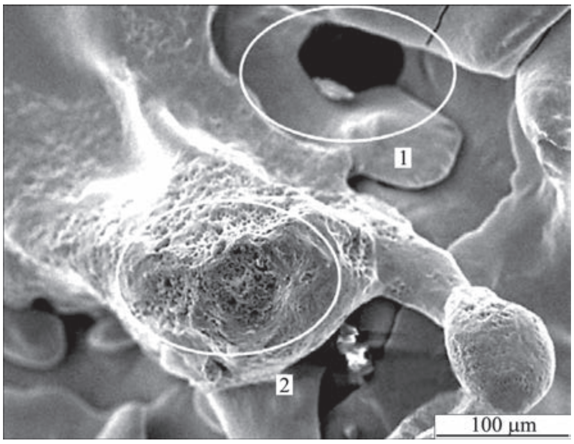

Figure 4. Morphology of the surface with macro- (*1*), micro- (*2*) pores of Zr–Nb coating formed at MPS parameters $I = 16$ A; $Q_m = 160$ l/h; $H = 40$ mm; $V_w = 2.9$ m/min

The surfaces of Zr–Nb coatings with the most pronounced microrelief had a roughness of $S_{\alpha} = 17 \pm 0.1$ µm (Figure 3).

A similar index of surface roughness, which promotes osseointegration processes, was obtained in [22] for a biocompatible titanium coating.

The study of the morphology of the surfaces of Zr–Nb coatings revealed not only open macropores up to 300 µm in size, but also micropores of up to 10 µm in size, which were located on the apexes of the coating protrusions formed from partially deformed dispersed particles from Zr–Nb wire (Figure 4).

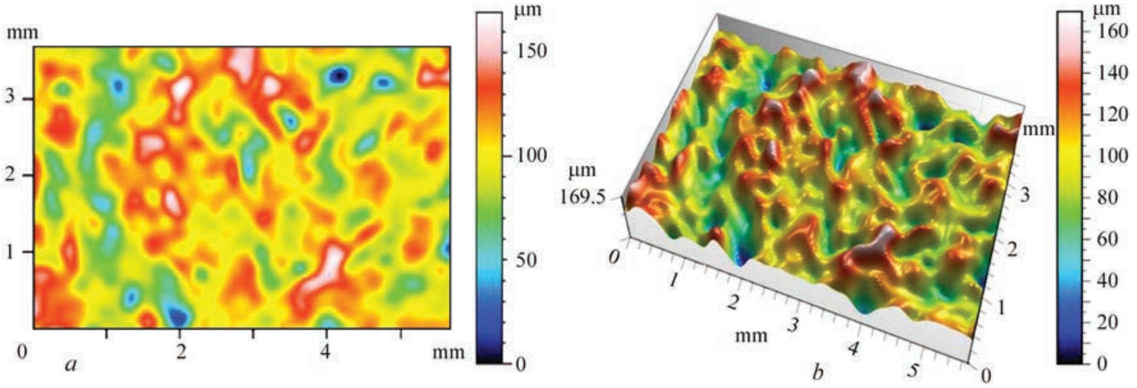

Figure 3. 2D (*a*) and 3D (*b*) topography of the surface microrelief of Zr–Nb coating produced at MPS parameters $I = 16$ A; $Q_m = 160$ l/h; $H = 40$ mm; $V_w = 2.9$ m/min

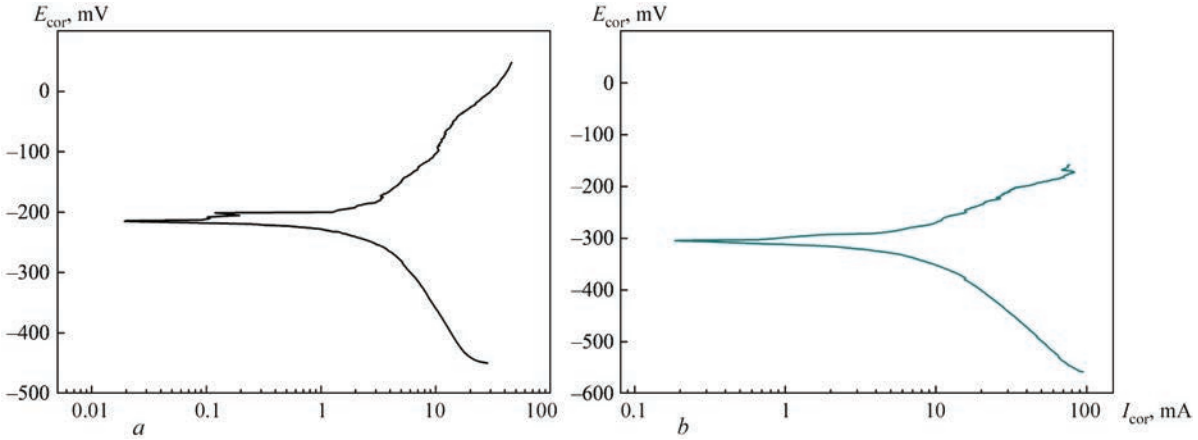

Figure 5. Polarisation diagrams of the dependence of the anode corrosion current density of Zr–Nb-coated samples (*a*) and Ti6A14V alloy base samples (*b*)

According to the literature, the results of the detected roughness and porosity will allow increasing the biocompatibility of the coating surface and ensuring a stronger bone-implant bonding due to the presence of places for fixation of the bone matrix and acceleration of the osseointegration process [23].

The carried out studies of the adhesion strength of Zr–Nb alloy coatings applied to the surface of Ti6A14V alloy samples showed that its average value for coatings with a thickness of 300 ± 10 μm with a volume pore content of 20.3 ± 2.0 % was 26 ± 2.1 MPa. Since there is currently no standard that defines the required adhesion strength of biocompatible Zr–Nb coatings with a porous structure to the surface of implants, their comparison was performed in accordance with the established requirement in the international quality standard ISO 13179-1:2021 for porous titanium coatings produced by plasma spraying on Ti6A14V alloy surfaces. According to the requirement of ISO 13179-1:2021, the average tear strength of a biocompatible coating should be more than 22 MPa. Therefore, the established adhesion of 26 ± 2.1 MPa, which characterises the adhesion strength of Zr–Nb coating to Ti6A14V alloy base, meets the requirements of ISO 13179-1:2021.

The results of studies of the corrosion resistance of Zr–Nb coating produced by the MPS method and from Ti6A14V alloy of the base after gas-abrasive treatment are presented in the form of polarisation diagrams (Figure 5).

From the analysis of polarisation curves, it was found that the plateau of the corrosion potential of Zr–Nb coating was about 216 mV and was in a more positive region of values than for Ti6A14V alloy base, which was 310 mV. Thus, the corrosion resistance of Zr–Nb-coated sample was higher than that of Ti6A14V alloy, which is explained by the presence of a protective surface oxide layer of ZrO_2, which reduces the corrosion rate by minimising the release of ions into the biological environment and promotes the process of osseointegration. Based on these characteristics, zirconium and its alloys were proposed as candidates for permanent implants [24].

An increased corrosion resistance mechanism is also facilitated by a film of niobium oxide (Nb_2O_5), which is formed along the boundaries of zirconium dioxide crystals and promotes “healing” of defects in the protective zirconium oxide film [25].

For all the studied samples of Zr–Nb coating and Ti6A14V alloy base, the anodic slope of the curve was similar to the cathodic slope of the curve in the polarisation diagram, which indicates that the kinetics of electron transfer for both the anodic and cathodic components is the same for both cases. The lower value of corrosion current density on Zr–Nb-coated samples (Figure 5, *a*) indicates a significantly lower rate of the corrosion process, which confirms the better efficiency of the surface layer protection by ZrO_2 oxide film. The similar results are given in [26] on the example of protecting the surfaces of magnesium alloys from corrosion in the human body, where ZrO_2 oxide film is recognised as more effective than TiO_2.

From the obtained results of the corrosion behaviour of the studied samples and their analysis, it was found that biocompatible Zr–Nb coatings produced by the MPS method will allow for much more effective corrosion resistance in biological solutions and an increase in the corrosion resistance of Ti6A14V alloy, which is currently most commonly used in the manufacture of implants.

CONCLUSIONS

1. It was determined that using the microplasma spraying method on the mode with parameters $I = = 16$ A, $Q_m = 160$ l/h, $H = 40$ mm, $V_w = 2.9$ m/min, the formation of Zr–Nb coating with the most developed microrelief with a roughness of $S_a = 17 \pm 0.1$ μm is ensured. In addition, the presence of both macropores of up to 300 μm in size

and micropores of up to 10 μm in size was found on the surface of a porous Zr–Nb coating.

2. X-ray diffraction studies of Zr–Nb coatings showed that they consist of an α-solid solution of Zr with the presence of oxide (ZrO_2 — prevailing number), nitride (ZrN) and carbide ($ZrNbC_2$) inclusions.

3. The obtained indices of corrosion resistance of Zr–Nb alloy coating samples in a solution of 0.9 % NaCl showed that the plateau of the coating corrosion potential was in a more positive region of values than for Ti6A14V alloy samples, which implies the formation of a passive layer that is a protective barrier against corrosion. The lower corrosion current density on Zr–Nb coating samples indicates their higher electrochemical resistance to corrosion and indicates a significantly lower rate of the corrosion process, which confirms the better efficiency of the surface layer protection by ZrO_2 oxide film.

4. As a result of the study of the adhesion strength of Zr–Nb coatings with a thickness of 300 ± 10 μm with a porous structure (pore content was 20.3 ± 2.0 % in the coating volume) with the surface of Ti6A14V alloy samples, an average adhesion strength of 26 ± 2.1 MPa was obtained, which meets the requirements of ISO 13179-1:2021 (over 22 MPa) and allows them to be used in accordance with the requirements of biocompatible titanium coatings on implant surfaces.

ACKNOWLEDGEMENT

The published results were obtained within the framework of the project No. 183/0070 dated 01.08.2024 “Development of innovative biocompatible antibacterial coatings and technology for their application to orthopaedic implants for using in the treatment of injuries in military personnel and civilians” with the grant support of the National Research Foundation of Ukraine within the framework of the competition “Science for Strengthening the Defence Capability of Ukraine”.

REFERENCES

1. Abd-Elaziem, W., Darwish, M.A., Hamada, A., Daoush, W.M. (2024) Titanium-based alloys and composites for orthopaedic implants applications: A comprehensive review. *Materials & Design,* **241**, 112850. DOI: https://doi.org/10.1016/j.matdes.2024.112850
2. Quinn, J., McFadden, R., Chan, C.-W., Carson, L. (2020) Titanium for orthopaedic applications: An overview of surface modification to improve biocompatibility and prevent bacterial biofilm formation. *Science*, 23(**11**), 101745. DOI: https://doi.org/10.1016/j.isci.2020.101745
3. Tepla, T., Pleshakov, E., Sieniawski, J., Bohun, L. (2022) Causes of degradation of titanium dental implants. *Ukrainian J. of Mechanical Engineering and Mater. Sci.*, 8(**4**), 31–40. DOI: https://doi.org/10.23939/ujmems2022.04.031
4. Wang, H., Liu, J., Wang, C. et al. (2020) The synergistic effect of 3D-printed microscale roughness surface and nanoscale feature on enhancing osteogenic differentiation and rapid osseointegration. *J. of Mater. Sci. & Technology*, **63**, 18–26. DOI: https://doi.org/10.1016/j.jmst.2019.12.030
5. Alontseva, D.L., Ghassemieh, E., Voinarovych, S. et al. (2019) Characterisation of the microplasma spraying of biocompatible coating of titanium. *J. of Microscopy*, 279(**3**), 148–157. DOI: https://doi.org/10.1111/jmi.12849
6. Woźniak, A., Staszuk, M., Reimann, Ł. et al. (2021) The influence of plasma-sprayed coatings on surface properties and corrosion resistance of 316L stainless steel for possible implant application. *Archives of Civil and Mechanical Engineering*, 21(**4**), 148. DOI: https://doi.org/10.1007/s43452-021-00297-1
7. Mehjabeen, A., Song, T., Xu, W. et al. (2018) Zirconium alloys for orthopaedic and dental applications. *Advanced Engineering Materials*, 20(**9**), 1800207. DOI: https://doi.org/10.1002/adem.201800207
8. Zhou, F.Y., Wang, B.L., Qiu, K.J. et al. (2012) Microstructure, mechanical property, corrosion behavior, andin vitrobiocompatibility of Zr–Mo alloys. *J. of Biomedical Materials Research Pt B: Applied Biomaterials*, 101B(**2**), 237–246. DOI: https://doi.org/10.1002/jbm.b.32833
9. Stich, T., Alagboso, F., Křenek, T. et al. (2021) Implant-bone-interface: Reviewing the impact of titanium surface modifications on osteogenic processes in vitro and in vivo. *Bioengineering & Translational Medicine*, **7**, e10239. DOI: https://doi.org/10.1002/btm2.10239
10. Cheikho, K., Laurent, C., Ganghoffer, J.F. (2022) An advanced method to design graded cylindrical scaffolds with versatile effective cross-sectional mechanical properties. *J. of the Mechanical Behavior of Biomedical Materials*, **125**, 104887. DOI: https://doi.org/10.1016/j.jmbbm.2021.104887
11. Wang, R., Ni, S., Ma, L., Li, M. (2022) Porous construction and surface modification of titanium-based materials for osteogenesis: A review. *Frontiers in Bioengineering and Biotechnology*, **10**, 973297. DOI: https://doi.org/10.3389/fbioe.2022.973297
12. Wang, H., Liu, J., Wang, C. et al. (2020) The synergistic effect of 3D-printed microscale roughness surface and nanoscale feature on enhancing osteogenic differentiation and rapid osseointegration. *J. of Mater. Sci. & Technol.*, **63**, 18–26. DOI: https://doi.org/10.1016/j.jmst.2019.12.030
13. Li, B.E., Li, Y., Min, Y. et al. (2015) Synergistic effects of hierarchical hybrid micro/nanostructures on the biological properties of titanium orthopaedic implants. *RSC Advances*, 5(**61**), 49552–49558. DOI: https://doi.org/10.1039/c5ra05821j
14. Cheng, B., Niu, Q., Cui, Y. et al. (2017) Effects of different hierarchical hybrid micro/nanostructure surfaces on implant osseointegration. *Clinical Implant Dentistry and Related Research*, 19(**3**), 539–548. DOI: https://doi.org/10.1111/cid.12471
15. Matsuzaka, K., Frank Walboomers, X., Yoshinari, M. et al. (2003) The attachment and growth behavior of osteoblast-like cells on microtextured surfaces. *Biomaterials*, 24(**16**), 2711–2719. DOI: https://doi.org/10.1016/s0142-9612(03)00085-1
16. Nakashima, Y., Hayashi, K., Inadome, T. et al. (1997) Hydroxyapatite-coating on titanium arc sprayed titanium implants. *J. of Biomedical Materials Research*, 35(**3**), 287–298. DOI: https://doi.org/10.1002/(sici)1097-4636(19970605)35:3%3C287::aid-jbm3%3E3.0.co;2-d
17. Jahani, B. (2021) The effects of surface roughness on the functionality of Ti13Nb13Zr orthopedic implants. *Biomedical J. of Scientific & Technical Research*, 38(**1**), 30058–30067. DOI: https://doi.org/10.26717/bjstr.2021.38.006104
18. Lewallen, E.A., Trousdale, W.H., Thaler, R. et al. (2021) Surface roughness of titanium orthopaedic implants alters the

biological phenotype of human mesenchymal stromal cells. *Tissue Engineering Pt A*, **27**, 1503–1516. DOI: https://doi.org/10.1089/ten.tea.2020.0369

19. Borisov, Yu.S., Kislitsa, A.N., Vojnarovich, S.G. (2006) Peculiarities of the process of microplasma wire spraying. *The Paton Welding J.*, **4**, 21–25.
20. Voinarovych, S.G., Alontseva, D.L., Kyslytsia, O.N. et al. (2021) Fabrication and characterization of Zr microplasma sprayed coatings for medical applications. *Advances in Mater. Sci.*, 21(**2**), 93–105. DOI: https://doi.org/10.2478/adms-2021-0013
21. Fousova, M., Vojtech, D., Jablonska, E. et al. (2017) Novel approach in the use of plasma spray: Preparation of bulk titanium for bone augmentations. *Materials*, 10(**9**), 987. DOI: https://doi.org/10.3390/ma10090987
22. Alontseva, D., Ghassemieh, E., Voinarovych, S. et al. (2020) Manufacturing and characterisation of robot assisted microplasma multilayer coating of titanium implants: Biocompatible coatings for medical implants with improved density and crystallinity. *Johnson Matthey Technology Review*, 64(**2**), 180–191. DOI: https://doi.org/10.1595/205651320x15737283268284
23. Cheikho, K., Laurent, C., Ganghoffer, J.F. (2022) An advanced method to design graded cylindrical scaffolds with versatile effective cross-sectional mechanical properties. *J. of the Mechanical Behavior of Biomedical Materials*, **125**, 104887. DOI: https://doi.org/10.1016/j.jmbbm.2021.104887
24. Rosalbino, F., Macciò, D., Scavino, G. (2023) Corrosion behaviour of Zr–Ag alloys for dental implant application. *Mater. Sci. and Applications*, 14(**11**), 501–514. DOI: https://doi.org/10.4236/msa.2023.1411033
25. Kirichenko, V.G. (2015) *Nuclear physics of metal sciences of power engineering alloys.* Chapt. 1, Kharkiv, KhNU [in Russian].
26. Peron, M., Bertolini, R., Cogo, S. (2022) On the corrosion, stress corrosion and cytocompatibility performances of ALD TiO_2 and ZrO_2 coated magnesium alloys. *J. of the Mechanical Behavior of Biomedical Materials*, **125**, 104945. DOI: https://doi.org/10.1016/j.jmbbm.2021.104945

ORCID

S.Yu. Maksymov: 0000-0002-5788-0753,
S.G. Voinarovych: 0000-0002-4329-9255,
S.N. Kaliuzhnyi: 0000-0002-8132-3930,
O.N. Kyslytsia: 0000-0001-8894-4660,
I.S. Sviridova: 0009-0005-6302-3423,
L. Alontseva: 0000-0003-1472-0685,
Ridvan Yamanoglu: 0000-0002-4661-8215

CONFLICT OF INTEREST

The Authors declare no conflict of interest

CORRESPONDING AUTHOR

S.Yu. Maksymov
E.O. Paton Electric Welding Institute of the NASU
11 Kazymyr Malevych Str., 03150, Kyiv, Ukraine.
E-mail: serge.voy@gmail.com

SUGGESTED CITATION

S.Yu. Maksymov, S.G. Voinarovych, S.N. Kaliuzhnyi, O.N. Kyslytsia, I.S. Sviridova, L. Alontseva, R.Yamanoglu (2024) Coating for medical application produced by microplasma spraying from Zr–Nb alloy. *The Paton Welding J.*, **12**, 3–9.
DOI: https://doi.org/10.37434/tpwj2024.12.01

JOURNAL HOME PAGE

https://patonpublishinghouse.com/eng/journals/tpwj

Received: 09.09.2024
Received in revised form: 29.10.2024
Accepted: 26.12.2024

DOI: https://doi.org/10.37434/tpwj2024.12.02

FEATURES OF EXPLOSION WELDING OF ODS STEEL FOR FAST NEUTRON REACTOR SHELLS

P.S. Shlonskyi, Feng Gao

Liaoning Xin Huayang Weiye Equipment Manufacturing Company Ltd No. 1 Road,
Tieling high-tech industrial development zone, Liaoning province, China

ABSTRACT

The paper investigates the possibility of explosion welding of plates and disks made of dispersion-strengthened low-plastic steel with oxides. In order to prevent the appearance of cracks on the surface of the plates, low-temperature (up to 200 °C) heating was applied to the flyer plate. In a wide range of explosion welding parameters with reference to the weldability window (WW), the microstructure of the resulting joint is shown for 2 mm thick and 50 diameter discs, that were laser welded into carbon and stainless steel plates. A tensile strength test was conducted for the obtained joints, it was possible to achieve a joint strength of 75 % of the strength of the base metal. Explosion welding of 100×50×3 mm plates was performed, the border of the joint zone has a typical wavy shape for explosion welding. Using energy dispersive X-ray spectroscopy, the chemical composition of inclusions in the joint zone was determined, and it was established that silicates are present in the joint zone. It is shown that the application of low-temperature heating allows welding plates from ODS steel with the help of explosion energy.

KEYWORDS: ODS-steel, explosion welding, weldability window, low-temperature heating, microstructure

INTRODUCTION

A distinctive feature of nuclear energy has always been the need for new structural materials for nuclear power plants.

Nanotechnology has been used in this field since before the prefix “nano” was used, since the created fuel and structural materials were largely based on a qualitative change in the properties of materials during the transition to the nanometric size range [1, 2].

The areas of application of nanotechnology in nuclear power are very diverse and cover almost the entire range of problems of the nuclear fuel cycle and the emerging fusion cycle. One of them is the creation of nanodispersed materials for structural and functional purposes, namely, ferritic-martensitic steels or nanodispersed ODS steels. The basis of such steel is Eurofer powder, to which tenths of a mass percentage of Y_2O_3 are added [3].

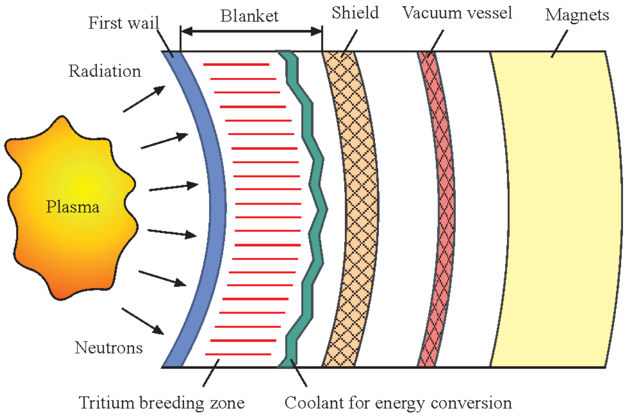

Figure 1. Schematic representation of the arrangement of materials in a tokamak [6]

Ferritic-martensitic steels are the main candidates for modern materials for fast reactor pressure vessels due to their satisfactory resistance to radiation and radiation swelling (with high-temperature irradiation by large neutron fluxes in austenitic steels and alloys based on Ni, Ti, Mo, Zr, Be, vacancy pores originate and grow, and mobile interstitial atoms move to edge dislocations and grain boundaries, which leads to a noticeable increase of the volume of metal — radiation swelling [4]). However, these steels can suffer from grain and/or matrix creep at temperatures above 550 °C.

To achieve the goal of operating innovative reactor systems at higher temperatures, it is necessary to consider the use of ODS steels. It is possible to use these steels for the blanket (Figure 1), which will increase the operating temperature to ~850 °C [3, 5, 6]. The blanket is a very thermally and radiation-intensive system of the international thermonuclear reactor — ITER, its purpose is to capture high-energy neutrons produced during a thermonuclear reaction, in it the neutrons are slowed down, releasing heat, which is removed by the cooling system.

A schematic representation of the arrangement of materials in a thermonuclear reactor is shown in Figure 1.

Evaluation of various (conventional and alternative) production methods, studies of mechanical properties and material degradation due to irradiation are widely carried out both in China and around the world (USA, Japan, Europe Union, Ukraine). Another pressing issue for ODS steels is the development methods for their inseparable connection by welding.. It is known that welding processes can adversely change the microstructure and, consequently, the mechanical properties of the base material. Therefore, understanding the microstructural changes caused by weld-

Table 1. Chemical components of ODS-steel(s)

Alloy	C	Si	Mn	Cr	V	W	Ta	Y_2O_3
Eurofer	0.12	0.06	0.42	8.87	0.19	1.1	0.14	0.3 or 0.5
Other elements weight (%) Nb, Mo, Ni, Cu, Al, Co limited by values ppm.								

ing and their impact on mechanical properties, as well as evaluating preventive measures, is of great importance to improve the quality of the received joint.

The joining of ODS steels is a challenging task, as traditional fusion welding processes, such as electron beam welding and non-consumable electrode welding, can not only change the characteristic microstructure of the base material, but also destroy Y_2O_3 particles, which can affect to the mechanical characteristics of material's at high temperatures.

The explosion welding (EW) is a process in which there is no need for a heat source, and an indissoluble joint is formed due to the mechanical (kinetic) energy of the impacting plates [7, 8]. Therefore, this method can be classified as "cold", i.e., not requiring heating to the melting point or close to it. The zone of thermal influence during explosion welding under optimal conditions relative to the thickness of the plates to be welded is small and amounts to several tens of micrometers. The duration of high temperatures is also short. This method can be used to join almost any metal and alloy to each other or through a layer of another metal.

Therefore, it is of interest to investigate the possibility of using explosive welding to join ODS steels with an estimate of the weldability window.

An important achievement of the hydrodynamic theory is the introduction of the concept of the WW [9–11]. The first ideas about the position of the weldability window boundaries were developed in the early 1970s. A significant contribution to the study of flow classification in the "V_c–γ" coordinate plane was made by A.A. Deribas and colleagues. Within the framework of the hydrodynamic approach, when designing the welding mode, it is necessary to ensure that the trajectory of the working point on the coordinate plane during the explosion welding process does not leave the part of the weldability window that corresponds to the modes of formation of a high-quality joint. The position of the boundaries of the weldability window is individual for each metal combination and is set experimentally.

For materials with low plasticity and high strength, EW with low-temperature heating is widely used in practice [12]. A successful example of such application can be considered the paper [13], which describes the development of the bimetallic composite manufacturing technology "high-speed steel P6M5 + carbon or low-alloy steel" for tool production. The viscous-brittle transition was most clearly determined in impact toughness tests and occurred in the temperature range of 125–175 °C. Therefore, EW of ODS-steel expedient to perform with low-temperature heating up to 200 °C, which will probably increase its plasticity and which is lower than the temperature of complete decomposition of saltpeter (210 °C), the main component of the explosive.

Table 2. Mechanical properties ODS-steel(s)

σ_y, MPa	σ_t, MPa	Uniform elongation δ, %	Total elongation δ, %
1060±45	1135±50	3.2±0.3	12.8±0.9

The aim of this work was for the first time in world practice to investigate the fundamental possibility of obtaining a welded joint between ODS steels using low-temperature heated explosion welding, to study its microstructure and strength.

INVESTIGATION PROCEDURE

For this work, ODS steel, manufactured in the European Union, so-called Eurofer ODS (0.3 wt.% Y_2O_3), was used in the form of a hot-rolled sheet of 260×225×3 mm, the size of the cut plates was 100×50 mm. The samples for research were obtained from the rod and had the shape of round discs with a thickness and diameter of 2 and 50 mm, respectively. The chemical composition and mechanical properties of ODS steel are shown in Tables 1 and 2, respectively.

Metallographic studies of the structure of metals after SH were carried out using a metallographic microscope MMO-1600 with a magnification of up to 1600×. The microstructure was photographed with a CMOS camera (KONUS, Italy) with a USB socket.

Since the disks are only 50 mm in diameter, they were welded into stainless steel plates (Figure 2) (throwing disk) and carbon steel (base disk) using la-

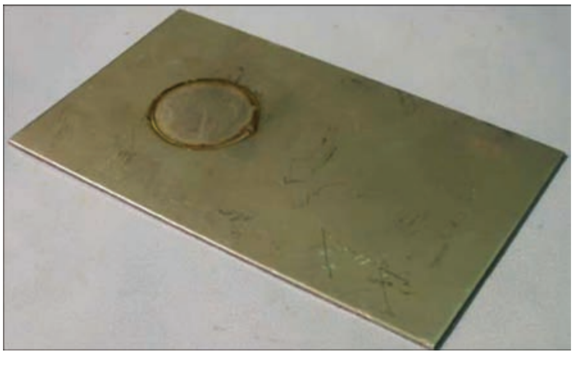

Figure 2. Steel disk ODS welded into stainless steel plate

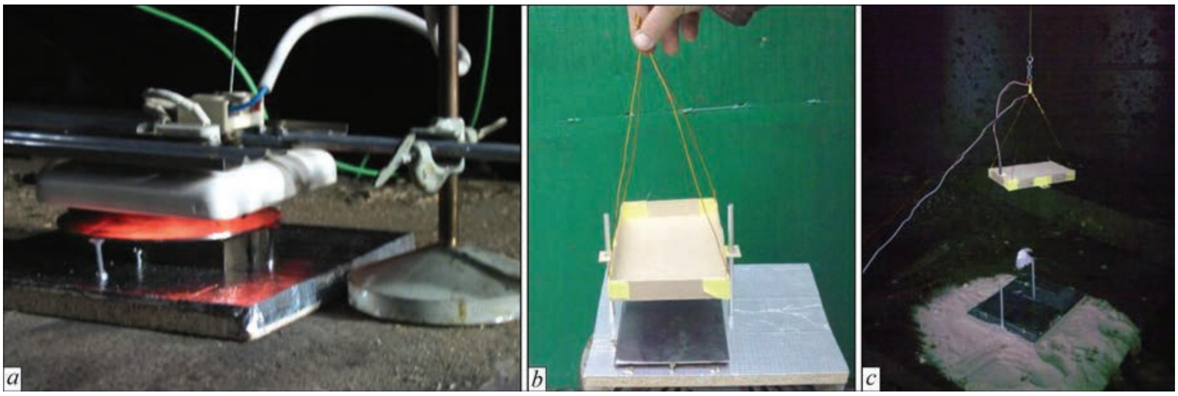

Figure 3. Additional operations during EW of the disk from ODS steels with low-temperature heating: *a* — heating; *b* — explosive box with bottom and guides; *c* — box filled with explosive ready for remote installation

ser welding. The discs were welded in order to move the initial and final unbonding zone their limits.

Figure 3 shows photographs of additional operations and devices for the implementation of the technology EW with heating. To heat the plate to be thrown, we used ceramic infrared heaters of the panel type manufactured by the German company Elstein (Figure 3, *a*). The temperature on the surface of the plate was measured using a four-channel thermometer Voltcraft K204 (measuring range from –200 to +1370 °C) with a K-type thermocouple.

In order to reduce the time for the formation of the charge, the box for the explosive substance was made with the bottom of Figure 3, *b*. That made it possible to pour the explosive powder into the box in advance and, after heating, quickly install it on the surface of the plate that is thrown. Guide rods were installed on the sides of the plates to be welded, and wings with holes were attached to the sides of the box (Figure 3, *b*), so the centering of the charge relative to the plates was ensured remotely. In Figure 3, *c* shows a cardboard box filled with an explosive and a detonator, which will be remotely lowered onto the plates which will be welded.

In order to determine the weldability range of ODS steel, experiments were conducted with the following initial angles α between the plates: –2.00°, 0.00°, +2.00° and +4.00° and the corresponding contact point velocities V_c (welding): 3881.00 $m{\cdot}s^{-1}$, 2875.00 $m{\cdot}s^{-1}$, 2290 $m{\cdot}s^{-1}$ and 1904.00 $m{\cdot}s^{-1}$. The welding gap was 4.8 mm. The plates with welded ODS-steel disks after WW are shown in Figure 4. A defect in the form of a crack, which can be observed in Figure 4, this is not a EW defect, the ODS-steel disks are welded together well, the delamination occurred in the laser welding zone.

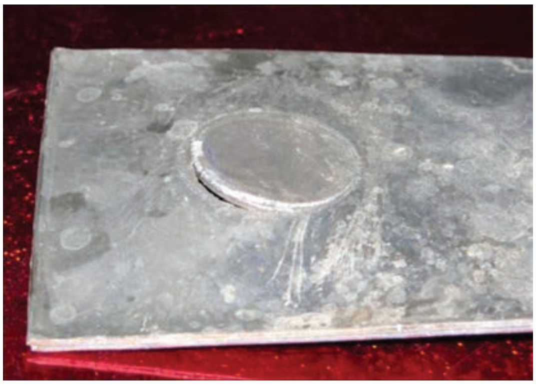

Figure 4. Plate welded with disks made of ODS-steel after EW

RESULTS AND DISCUSSION

After explosion welding, the samples were subjected to metallographic studies. The microstructure of the ODS-steel joint zone at different modes with reference to the weldability window (WW) is shown in Figure 5.

The left part of the weldability window is represented by the microstructure image Nos 1, 2. Very large strain shifts are observed there, either with almost no waves in No. 1 or with long waves at the interface between the ODS steel disks No. 2.

Regular waves with an amplitude of approximately 100 μm and the absence of melts in the image of microstructure No. 3 indicate that it is in this regime that the best conditions for the EW ofODS-steel are realized.

In the image of microstructure No. 4, you can see that the wave amplitude becomes smaller compared to No. 3. This is because the velocity of the impact point has increased to approximately 4000.00 m/s. Therefore, due to the heat generated at high welding speeds, vortices, the so-called "pockets", begin to form.

Thus, it can be said that the optimal detonation speed for welding ODS steel is 2875 $m{\cdot}s^{-1}$, and the welding gap is 4.8 mm, which provides a impact velocity of about 750 $m{\cdot}s^{-1}$.

In the image of microstructure No. 4, you can see the marks after measuring the microhardness near the joint zone and in the "pockets". However, the microhardness values are close: 440 *HV* near the interface and 420 *HV* in the "pockets".

After conducting research on samples with disks, plates made of ODS steel measuring 100×50×3 mm were welded. Welding was performed with heating up to 200 °C, the welding mode was as follows: welding gap — 4 mm; explosive mixture of Ammonite 6ZhV

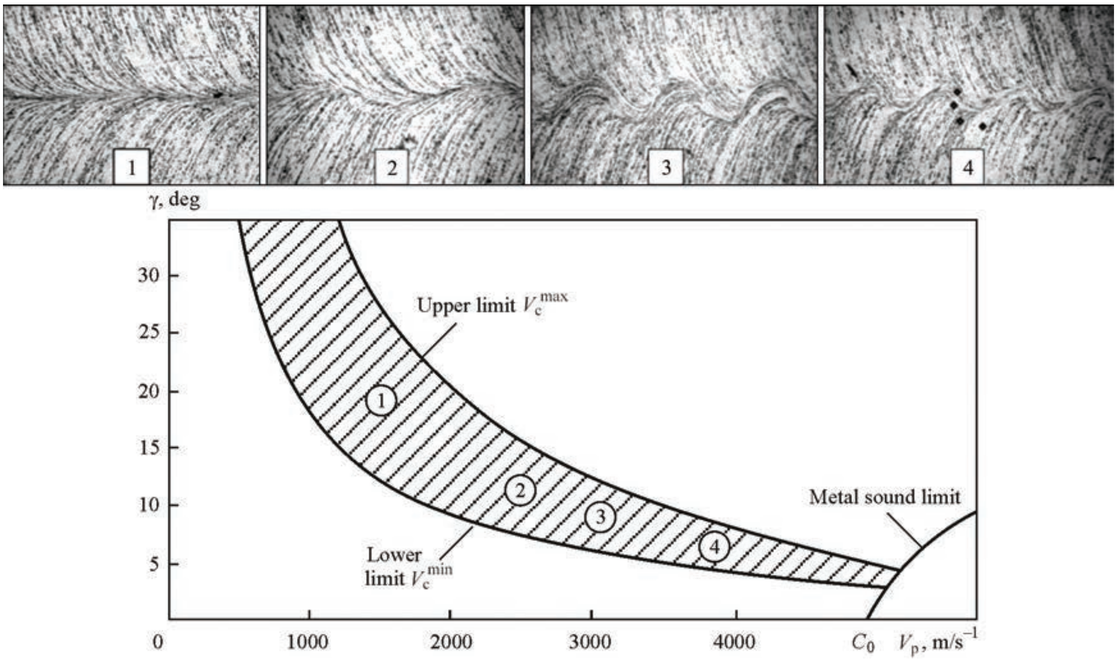

Figure 5. Microstructure of the welding zone of ODS-steel disks under different welding modes (*a*) with reference to the WE (*b*). 1 — $\alpha = +4{,}00°$, $V_c = 1904.00$ m·s^{-1}; 2 — $\alpha = +2°$, $V_c = 2290$ m·s^{-1}; 3 — $\alpha = 0.00°$, $V_c = 2875$ m·s^{-1}; 4 — $\alpha = -2°$, $V_c = 3881.00$ m·s^{-1}

with sand 60 %/40 %. As a result, it was possible to successfully weld the plates together and obtain the sample shown in Figure 6. A section was cut out of the obtained sample to study the microstructure of the joint zone. The image of the ODS-steel + ODS-steel microstructure is shown in Figure 7.

After etching, the cross-section of the sample has a typical wavy shape at the interface and light inclusions (indicated by red arrows). Energy dispersive X-ray spectroscopy (EDX) of Figure 8 showed that these inclusions are silicates, Table 3. The locations of the EDX analysis are indicated by arrows and numbers.

A possible explanation for the presence of silicates on the surface between the plates is that due to the short length of the plates to be welded, complete cleaning of the surfaces by the cumulative jet did not occur. Studying the effect of these inclusions on the mechanical properties of the material welded by the blast and the presence of silicates in subsequent samples is of interest for further research.

Since EW of ODS steel is performed with low-temperature heating, it is interesting to theoretically estimate the temperature that will be in the zone of joint formation and test its tensile strength.

During EW, the metal layers adjacent to the contact surface are heated by several mechanism [8]:

- large plastic shear deformations of the surface layers;
- capture of the cumulative flow (the so-called “back jet”) during welding in the mode with the formation of waves [7, 14];
- heating from shock compressed air in the welding gap.

In our case, the first two mechanisms are essential, since the length of the workpieces is short.

The degree of heating depends on the choice of the EW mode. Heating from shear deformations is always present, but in the case of EW with wave formation, its intensity is increased due to the presence of the tangential component V_t of the velocity of surface contact. The larger V_t, the greater

Figure 6. Sample of the ODS-steel + ODS-steel obtained by EW

Figure 7. The microstructure of the EW zone of ODS-steel plates

Figure 8. The locations of EDX analysis are indicated by arrows and numbers

the shear deformation and heating. Therefore, the magnitude of the V_t component and the heating intensity change cyclically with a period equal to the wavelength.

Plastic shear deformations due to V_t and the capture of cumulative flow are responsible for the formation of melts in the so-called "pockets". The volume of the vortex zone content increases as the mode moves away from the lower boundary of the WW, and as it approaches the upper boundary, the melts can form a continuous layer, which deprives the joint of strength. At the same time, the greater the relative elongation of the weld gap (the ratio of its length to width), the greater the proportion of the cumulative flow that is trapped in the vortex zone. In our case (ODS + ODS), there are no clearly defined vortices yet, but the micrographs already show quite significant melt zones (light) Figure 7.

At present, there are no methods for engineering calculation of thermal fields at the EW (especially in the mode with wave formation). There is a known technique for the experimental determination of thermal fields, which requires measurements of plastic deformation fields in samples taken from metal layers. This technique, developed at the Volgograd State Technical University, is cumbersome and expensive, and is rarely used.

The existing understanding of the heating intensity in the modes of explosive welding used in our experiments is as follows. The plates to be welded can be conditionally divided into three zones by thickness:

- a formation zone of bonding (FZB) adjacent to the contact surface, the thickness of which is assumed to be equal to the amplitude of the welding waves;
- a transition zone of the same thickness order as the FZB;
- the main layer of the plate.

The thickness of the first two zones combined is an order of magnitude less than the thickness of the plates to be welded (in our case, they occupy approximately 12–15 % of the thickness). The main volume of the plate is heated by tens of degrees Celsius during the EW process. The temperature field equalization in the welded sample generally takes tens of microseconds. The temperature of the throwing plate and the contact zone after alignment can reach 100 °C, provided there is no preheating.

Table 3. Results of EDX analyses of the inclusions

Location	Chemical composition, wt.%						
	W	Si	Ca	V	Cr	Mn	Fe
Base metal	1.0	0.1	–	0.2	9.3	0.6	88.8
Point 1	0.9	0.3	–	–	9.7	–	89.1
Point 2	–	4.6	–	0.7	13.1	–	81.6
Point 3	–	7.1	0.5	–	9.0	–	83.3

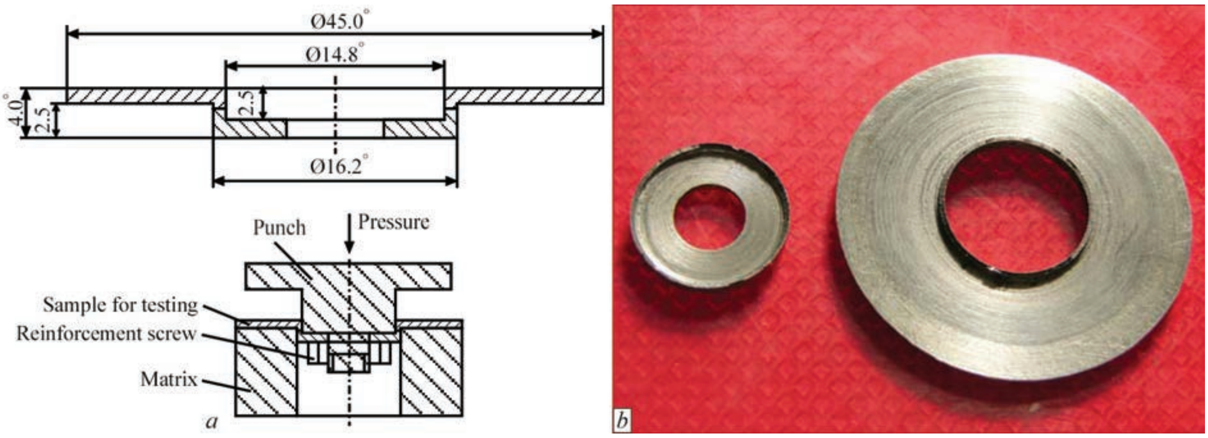

Figure 9. Scheme of the sample and assembly for ODS-steel tensile tests (*a*) and the view of the ODS-steel samples after the tests (*b*)

The temperature of the joint formation zone reaches its maximum on the contact surface. In our case, in some areas of the contact surface, it reaches the melting point. The average temperature of the joint formation zone for ordinary metals can be 550–750 °C. In our case of a high-strength metal and rather high velocities of plate throwing (750 m/s) and detonation (2850 m/s), it is likely to be 800–900 °C.

The maximum temperature reached in the transition zone varies with its thickness for ordinary metals in the range from 100 to 200–400 °C, in our case, possibly to a higher temperature.

Thus, it can be assumed that preheating to 200 °C of ODS steel plates to be welded by explosion will not have a significant impact on their mechanical properties after EW.

Tensile strength tests were performed for ODS steels welded by explosion according to the scheme shown in Figure 9, *a*, *b* shows a sample after tear tests. The tensile strength for ODS steels welded by explosion in mode 3 was 851 MPa.

CONCLUSIONS

1. The research and development work carried out has shown that explosive welding of ODS steel to an ODS disk has a wide weldability window within the contact point speed range of 2000.00 to 4000.00 m/s. The highest joint strength achieved for ODS steel is 75 % of the strength of the base metal.

2. The extremely high strength and low ductility of ODS-steel requires preliminary low-temperature heating (up to 200 °C) of the plate that is thrown, as well as the use of welding modes with an increased speed of the contact point, compared with ordinary steels.

3. The structure of ODS-steel is quite attractive for the study of high-speed deformation and the mechanism of explosion welding, so the development of further research and development work looks quite interesting and perspective.

REFERENCES

1. Azarenkov, N.A., Voevodin, V.N., Kirichenko, V.G., Kovtun, G.P. (2010) Nanostructured materials in nuclear energy. *News of Kharkiv National University V.N. Karazin, Ser. Physical “Nuclei, Particles, Fields”*, **887**, 4–24.
2. Solntsev, Yu.P. (1993) *Radiation-resistant materials*. Moscow, Energoatomizdat [in Russian].
3. Esteban, G.A., Peca, A., Legarda, F., Lindau, R. (2007) Hydrogen transport and trapping in ODS-Eurofer. *Fusion Eng. and Design*, **82**, 2634–2640.
4. Kirichenko, V.G., Litovchenko, S.V. (2012) *Metallography and metallurgy of steels*: *1. Alloys and nanomaterials in nuclear power engineering*: Textbook. Kharkiv, V.N. Karazin Kharkiv National University.
5. Kompaniets, T.N. (2009) On the problem of steel selection for the demo reactor. *Issues of Atomic Science and Technology, Thermonuclear Fusion Series*, **3**, 16–24.
6. Suri, A.K., Krishnamurthy, N., Batra, I.S. (2008) Materials issues in fusion reactors. In: *Proc. of Conf. on 23rd National Symp. on Plasma Sci. & Technology (PLASMA-2008), 10–13 December 2008, Bhabha Atomic Research Center, Trombay, Mumbai, India. J. of Phys. Conf. Ser*, **208**, 1–15. DOI: https://doi.org/10.1088/1742-6596/208/1/012001
7. Kudinov, V.M., Koroteev, A.Ya. (1978) *Explosion welding in metallurgy*. Moscow, Metallurgiya [in Russian].
8. Lysak, V.I., Kuzmin, S.V. (2005) *Explosion welding*. Moscow, Mashinostroenie [in Russian].
9. Loyer, A., Hay, D.R., Cagnon, G. (1975) Weldability windows and the selection of explosive welding process parameters. In: *Proc. of 5th Inter. Conf. on High Energy Rate Fabrication, Denver, Colorado*, S. l., s. a., 4.3.1–4.3.14.
10. Petushkov, V.G., Simonov, V.A., Sedykh, V.S., Fadeenko, Yu.I. (1997) *Welding and surfacing reviews*. Vol. 3, Pt 4: Explosion welding criteria. Ed. by B.E. Paton. Harwood, Harwood Academic Publ.
11. Deribas, A.A. (1974) Classification of flows arising during Oblique collisions of metal plates. In: *Proc. of II Inter. Symp. On Use of Explosion Energy for Production of Metal Materials with New Properties, Marianske Lazne, Czechoslovakia, October 9–12, 1973*. Pardubice, Vol. 1., 28–43.
12. Dobrushin, L.D., Illarionov, S.Yu., Shlenskiy, P.S., Fadeenko, Yu.I. (2010) Explosion welding with moderate preheating (Brief review). *Izvestiya VolGTU*, **5**, 63–65 [in Russian].
13. Belyaev, V.I., Busel, N.A., Kravtsov, V.B. (1983) Application of explosion energy for obtaining a bimetallic cutting tool based on high-speed steel. In: *Application of explosion energy in welding equipment*. Kyiv, PWI, 86–88.
14. Cowan, G., Holtzman, A. (1963) Flow configuration in colliding plates. *J. of Aplied Physics*, 34(**4**), 928–939.

ORCID

P.S. Shlonskyi: 0000-0002-3566-1752

CONFLICT OF INTEREST

The Authors declare no conflict of interest

CORRESPONDING AUTHOR

P.S. Shlonskyi
Liaoning Xin Huayang Weiye Equipment
Manufacturing Company Ltd No. 1 Road,
Tieling high-tech industrial development zone,
Liaoning province, China.
E-mail: shlensk@ukr.net

SUGGESTED CITATION

P.S. Shlonskyi, Feng Gao (2024) Features of explosion welding of ODS steel for fast neutron reactor shells. *The Paton Welding J.*, **12**, 10–15.
DOI: https://doi.org/10.37434/tpwj2024.12.02

JOURNAL HOME PAGE

https://patonpublishinghouse.com/eng/journals/tpwj

Received: 25.09.2024
Received in revised form: 23.10.2024
Accepted: 18.12.2024

DOI: https://doi.org/10.37434/tpwj2024.12.03

FORMATION OF POROUS COATINGS ON TITANIUM ALLOYS BY THE METHOD OF PLASMA ELECTROLYTIC OXIDATION IN ALKALINE ELECTROLYTES SATURATED WITH PHOSPHATES AND BIO-ADDITIVES

N.Yu. Imbirovych[1], **O.Yu. Povstyanoy**[1], **K.J. Kurdzydlowski**[2], **V.V. Tkachuk**[1]

[1]Lutsk National Technical University
75 Lvivska Str., 43018, Lutsk, Ukraine. E-mail: n.imbirovych@lntu.edu.ua
[2]Bialystok University of Technology
45A, Wiejska Str., 15-351 Bialystok, Poland

ABSTRACT

Environmentally friendly electrolytes have been developed to ensure the formation of coatings based on titanium alloys by plasma electrolytic processing, which contain phosphates in the form of sodium pyrophosphate ($Na_4P_2O_7$) and sodium hexamethophosphate ($Na_6P_6O_{18}$), calcium-containing components in the form of calcium hydroxide and hydroxylapatite, as well as a bio-additive in the form of diatomite in different concentrations. The study of the stages of PEO coating formation is presented with the help of time dependences of the voltage change on the anode during the processing. The presented dependencies made it possible to establish the optimal ratio of I_a/I_c current density, at which uniform coatings are formed. The through-thickness porosity of the synthesized PEO-coatings in different modes was determined through experimental studies. It is shown that coatings formed in an electrolyte with phosphates are characterized by the maximum rate of such porosity (0.75 %), while high water absorption is characteristic of coatings formed in an electrolyte with diatomite, which is 1.21 % against 0.6 %. Such values satisfy the conditions of biocompatibility of the materials.

KEYWORDS: plasma electrolytic oxidation; synthesis, biocompatibility, coating, porosity, thickness

INTRODUCTION

Plasma electrolytic oxidation (PEO), also known as microarc oxidation (MAO) or anode spark deposition (ASD), is a cost effective and ecofriendly technology, which allows forming an oxide on the surface of aluminium, magnesium, titanium, zirconium, tantalum, niobium, hafnium and other light metals and their alloys [1–5]. More over, the thus formed oxide coatings are characterized by a controlled morphology, high microhardness, wear- and corrosion resistance, excellent strength of adhesion to the base, high dielectric and thermal properties [6–14].

During PEO discrete spark discharges appear on the surface, when the applied voltage exceeds the critical values (known as the voltage of breakdown of the oxide semiconductor film). The discharge occurs as a result of the loss of the oxide film dielectric stability in the low electric conductivity region. This process is accompanied by sparking [15] and gas evolution [16, 17]. The microdischarge leads to high temperature and pressure in the local region that allows forming oxide coatings, which consist not only of the stoichiometric composition of the processed metal oxides, but also from more complex oxides, containing compounds, which form as a result of plasma-chemical reactions of the metal with the electrolyte components [18]. Although the microdischarge phenomena and their influence on the formation mechanism, composition, morphology and other properties of oxide PEO-coatings on aluminium and magnesium have been sufficiently researched, the correlated studies of titanium have not been fully conducted.

Titanium is a widely used metal in engineering, owing to its properties, such as high strength, low density, high melting temperature and good biocompatibility [19–21]. The effectiveness of using titanium alloys in implantology was studied for a long time [22, 23]. The high biocompatibility is due to titanium ability to form on its surface a protective oxide layer in fractions of a second, due to which it does not corrode and does not release free metal ions, which can cause pathological processes in the vicinity of the implant. Due to that, the tissues adjacent to the prosthesis remain free from metal ions [24].

Titanium alloys are used as prosthesis of shoulder, hip and knee joints, as well as for manufacturing plates for fracture splicing. Titanium lightness also determines its wide application for medical instruments [25, 26]. However, after bone replacement surgery, at least 17.5 % of the cases require repeated operation [27]. Incomplete osteointegration and bacterial infection are a threat for normal implant survival. The authors of [28] describe effective application of coatings with a wide porosity range in their work. This effect leads to higher osteointegration [29].

It is known that the main disadvantages of the titanium alloys are poor machinability, high coefficient of friction, relatively low modulus of elasticity, while a low chemical activity and strength of adhesion to the muscle tissues and the bone are also added for implantology. These facts can lead to resorption of the bones in their vicinity [30, 31].

An efficient method to prevent this effect is predeposition of a bactericidal layer on the material surface. Arash Fattah-alhosseini et al. report that a lot of attention should be given to coating nontoxicity that may lead to appearance of multidistant pathogens [32, 33]. A possible solution to this problem is surface modifications which improve the implant osteointegration, or reduce the bacterial infection. In view of the above, application of compositions with antimicrobial properties in the bone plastics is promising [34, 35]. These are exactly the requirements satisfied by PEO as a promising method with the possibility of modification of the light alloy surface with various calcium-containing components, phosphates and bio-additives [36–39].

THE OBJECTIVE

of this work is development of the technology of saturation of oxide PEO-coatings based on a titanium alloy with phosphates and diatomaceous soil (diatomite) to increase their porosity and roughness.

INVESTIGATION PROCEDURE

The object of study are coatings based on Ti–6Al–4V titanium alloy (class 5), which was synthesized by the method of plasma electrolytic oxidation. Round flat samples of the following dimensions: 20 mm diameter, 5 mm thickness were tested. The electrolyte was an aqueous solution based on potassium hydroxide (KOH), calcium hydroxide ($Ca(OH)_2$), sodium silicate ($Na_2O(SiO_2)_n$), sodium pyrophosphate ($Na_4P_2O_7$), sodium hexamethophosphate ($Na_6P_6O_{18}$) at their different concentration (0.5–20 g/l). To clarify the influence of bioactive natural materials on the coating properties, calcium hydroxylapathite ($Ca_{10}(PO_4)_6(OH)_2$) and diatomite (main component is SiO_2) were added to the electrolyte in the amount of 1 and 20 g/l, respectively. PEO modes were characterized by the ratio of the anode to cathode currents, I_a and I_c, respectively, and by processing duration.

In this work we considered the characteristics of a microdischarge at plasma electrolytic oxidation through determination of electrophysical parameters of the coating synthesis. Coating morphology was studied in Tagarno Prestige FHD microscope, Xplus controller and 3D laser scanning microscope Keyence VHX 7000. Coating roughness was analyzed in keeping with DSTU ISO 4287:2012 by the following parameters: R_a — arithmetic mean deviation of the profile, R_z — height of profile unevenness over 10 points. Coating density was determined by pycnometric method (DSTU ISO 2811-1:2019), through-thickness porosity and water absorption – by hydrostatic weighing (DSTU B A.1.1-49–94).

EXPERIMENTAL RESULTS AND THEIR ANALYSIS

Derived dependencies (Figure 1) allowed establishing that coating formation is influenced by the current density ratio.

In order to establish the influence of phosphates and calcium-containing components on the stages of the process of synthesis of oxide-ceramic coatings, voltage change in time was studied in electrolytes without phosphates and with their addition.

In electrolyte with 2g/l KOH + 3 g/l $Na_2O(SiO_2)_n$, initial voltages at which the coating is formed, are equal to 73–160 V (Figure 1). Here, at the stage of the first 10 min, the voltages rise faster, that is attributable to the presence of an oxide film with unipolar conductivity on the titanium alloy surface. This is exactly why this film should be removed to ensure the conditions for deposition of coatings on such alloys. In the presence of high voltages on the electrode, electron injection into the oxide layer takes place. This is what accounts for the initial voltage rise, found in all the studied systems.

The obtained results suggest that the anode voltage is influenced by the current density, which is set to be stable during synthesis. Thus, synthesizing the coating at I_a/I_c = 10/5 A/dm^2, mean voltage value at which the coating is formed, is equal to 82.5 V. If we set the

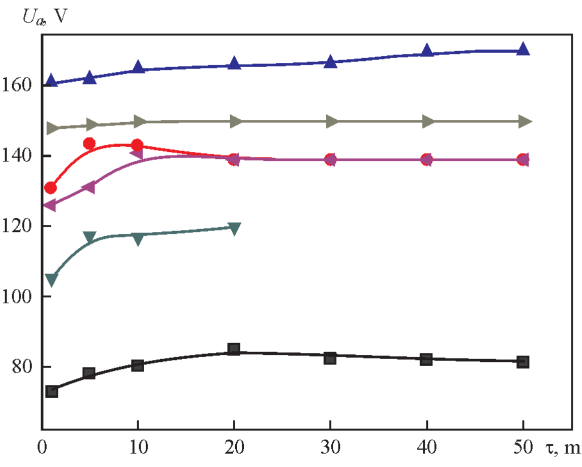

Figure 1. Electrophysical parameters of PEO-alloy Ti–6Al–4V in an electrolyte of 2 g/l KOH + 3 g/l $Na_2O(SiO_2)_n$, at current density ratios of 2, 1.5 and 1.25 and synthesis time of 20 and 50 min: ■ — I_a/I_c = 10/5 A/dm^2; ● — I_a/I_c = 75/60 A/dm^2; ▲ — I_a/I_c = 50/40 A/dm^2; ▼ — I_a/I_c = 150/100 A/dm^2; ◀ — I_a/I_c = 150/120 A/dm^2; ▶ — I_a/I_c = 100/80 A/dm^2

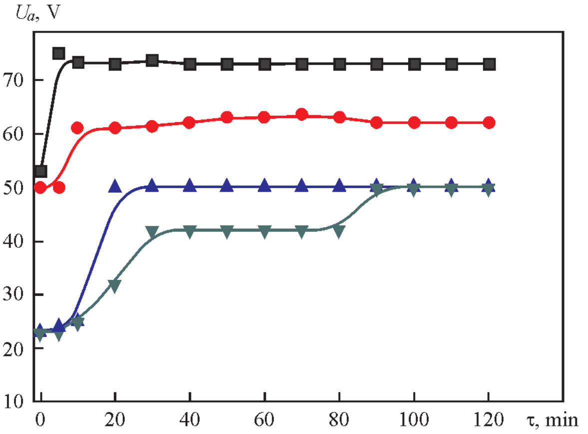

Figure 2. Electrophysical parameters of PEO-alloy Ti–6Al–4V in electrolytes of 3 g/l KOH + 2 g/l $(Na_2O(SiO_2)_n$ (■, ▲) and 5 g/l KOH + 5 g/l $(Na_2O(SiO_2)_n$ (●, ▼) at synthesis time of 120 min at I_a/I_c = 10/10 (▲, ▼) and 20/20 A/dm² (■, ●)

current density ratio I_a/I_c = 150/100 A/dm², the initial anode voltage of synthesis rises by 32 V, and the mean voltage value, at which the coating forms, rises by 35.8 V. Increase of anode current density 15 times and that of cathode 24 times (I_a/I_c = 150/120 A/dm²) leads to voltage rise at the start of synthesis by 53 V, and the mean value of voltage at which the coating forms in this mode, rises by another 3.9 V, compared to voltage of the start of PEO process in the same mode.

Note that the oxide film breakdown is followed by the process of metal oxidation in the high-temperature channel with running of plasma-chemical reactions on the anode. Such a process is represented by the rectilinear section on the curve of voltage dependence on synthesis time.

Figure 2 shows the dependencies of synthesis voltage change in phosphate free electrolytes with the ratio I_a/I_c = 10/10 and I_a/I_c 20/20 A/dm². One can see from the derived dependencies that the electrolytes with a higher concentration ensure higher conductivity, leading to decrease of voltage of the studied system.

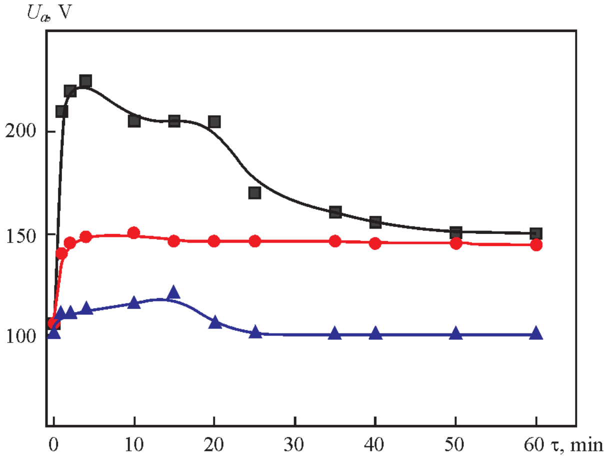

Figure 3. Electrophysical parameters of PEO-alloy Ti–6Al–4V in an electrolyte of the composition of 0.5 g/l KOH + 0.5 g/l $Ca(OH)_2$ + $Na_2O(SiO_2)_n$ + 0.5 g/l $Ca(OH)_2$ + 0.5 g/l $Na_6P_6O_{18}$ + 0.5 g/l $Na_4P_2O_7$ at I_a/I_c = 20/20 (■), 15/10 (●) and 10/10 A/dm² (▲)

Increase of current density leads to increase of anode voltage, electron injection into the oxide layer being provided at smaller energy losses for the breakdown channel at current density ratio I_a/I_c = 20/20 A/dm².

For coating saturation with phosphates, an electrolyte with components of sodium pyrophosphate ($Na_4P_2O_7$) and sodium hexamethaphosphate ($Na_6P_6O_{18}$) was developed. Derived dependencies of synthesis voltage change in time are presented in Figure 3.

Synthesis of oxide PEO-coatings in an electrolyte with phosphates leads to a rapid rise of anode voltage. Among the given results, we should single out the mode with current density ratio I_a/I_c = 1.5, at which uniform coatings are formed.

Having obtained the results on the dependencies at current density ratio of 15/10 A/dm³ in the electrolyte with added salts, it was found that the anode voltage coincides with the voltage, which is recorded at titanium alloy synthesis in a sodium salt free electrolyte, containing calcium hydroxide [1]. Thus, it becomes clear that sodium salts increase the conductivity of the working environment.

Coating saturation with calcium-containing components was performed through addition of hydroxyl apatite (HAp) and diatomite to the electrolyte. Electrophysical parameters of coating formation in such electrolytes are shown in Figure 4. Derived dependencies allowed establishing that the coatings form uniformly with addition of hydroxylapatite and diatomite. Thus, the developed electrolytes provide satisfactory conductivity. As one can see from the presented dependencies, oxide film breakdown in an electrolyte with HAp requires a large margin of energy which cannot be said about coating formation in an electrolyte with diatomite, where a rapid increase of anode voltage is absent. Providing a higher ratio of current density in the system, namely 20/20 A/dm², compared to 10/10 A/dm², leads to decrease of voltage, at which coating synthesis occurs, by approximately 25 V. The same regularity is preserved also for coating synthesis in an electrolyte with diatomite (Figure 4).

It should be also noted that diatomite addition to electrolyte leads to increase of electric conductivity of the working medium that reduces the anode voltage during PEO.

In order to establish the degree of hydrogen ion activity in electrolyte medium or the degree of their acidity, pH level of the medium was determined before the coating synthesis process, and after completion of the process of titanium alloy surface treatment. Thus, it was found that before the start of coating synthesis the electrolyte pH was equal to 12.6. After

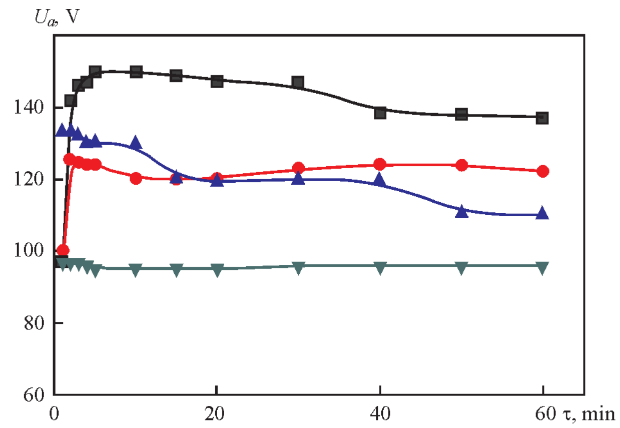

Figure 4. Electrophysical parameters of synthesis of PEO-coating on a titanium alloy in an electrolyte of 5 g/l KOH + 5 g/l $Ca(OH)_2 + 5Na_2O(SiO_2)_n$ + 5 g/l $Ca(OH)_2$ + 5 g/l $Na_6P_6O_{18}$ + 5 g/l $Na_4P_2O_7$ + 1 g/l HAp and 20 g/l KOH + 20 g/l $Ca(OH)_2$ + + $20Na_2O(SiO_2)_n$ + 20 g/l $Na_6P_6O_{18}$ + 20 g/l $Na_4P_2O_7$ + 20 g/l diatomite: ■ — HAp with I_a/I_c = 10/10 A/dm²; ● — HAp with I_a/I_c = 20/20 A/dm²; ▲ — with diatomite I_a/I_c = 10/10 A/dm²; ▼ — with diatomite I_a/I_c = 20/20 A/dm²

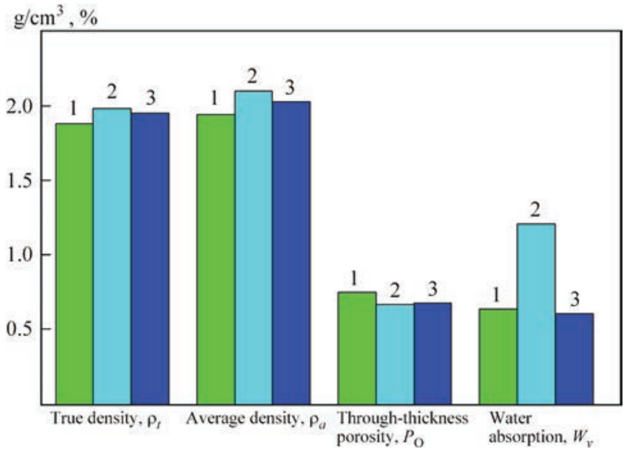

Figure 6. Results on true density, average density, porosity and water absorption of PEO-coatings synthesized in different electrolytes: *1* — 0.5 g/l KOH + 0.5 g/l l.g + $0.5Ca(OH)_2$ + 0.5 g/l $Na_4P_2O_7$ + 0.5 g/l $Na_6P_6O_{18}$; *2* — 20 KOH + 20 g/l l.g + 1 g/l $Ca(OH)_2$ + 20 g/l $Na_4P_2O_7$ + 20 g/l $Na_6P_6O_{18}$ + 20 g/l diatomite; *3* — 3 g/l KOH + 2 g/l l.g + 3 g/l $Ca(OH)_2$

completion of the process of coating deposition on the metal surface pH level increases slightly and is equal to 12.8.

The surface of the coatings produced as a result of PEO is covered by craters and pores and it has a rather high roughness (Figure 5). This is attributable to the features of the synthesis process, which is characterized by constant formation of breakdown channels and their disappearance during the entire PEO duration. Studies of the surface morphology and its roughness revealed that the coatings synthesized in an electrolyte with diatomite (electrolyte with 20 g/l KOH + 20 g/l l.g + 20 g/l $Na_6P_6O_{18}$ + 20 g/l $Na_4P_2O_7$ + 20 g/l diatomite) have greater surface roughness (R_a = 40 µm, R_z = 239 µm), while the coatings synthesized in electrolyte of the following composition 20 g/l KOH + 20 g/l l.g + 20 g/l $Na_6P_6O_{18}$ + 20 g/l $Na_4P_2O_7$ have roughness R_a = 5–137 µm and R_z = 28–100 µm (here l.g — liquid glass). Processing duration also influences surface roughness. So, coatings processed two times longer (60 against 30 min), have 5 times higher surface roughness. Here, owing to the twice longer processing time, surface roughness parameter R_a increases from the value of 20.4 up to 42.1 µm, while roughness parameter R_z varies from 119.7 to 239.4 µm, respectively.

Studies of the coating porosity showed that the coatings are produced with through-thickness porosity of maximum 0.75 %, that is characteristic for

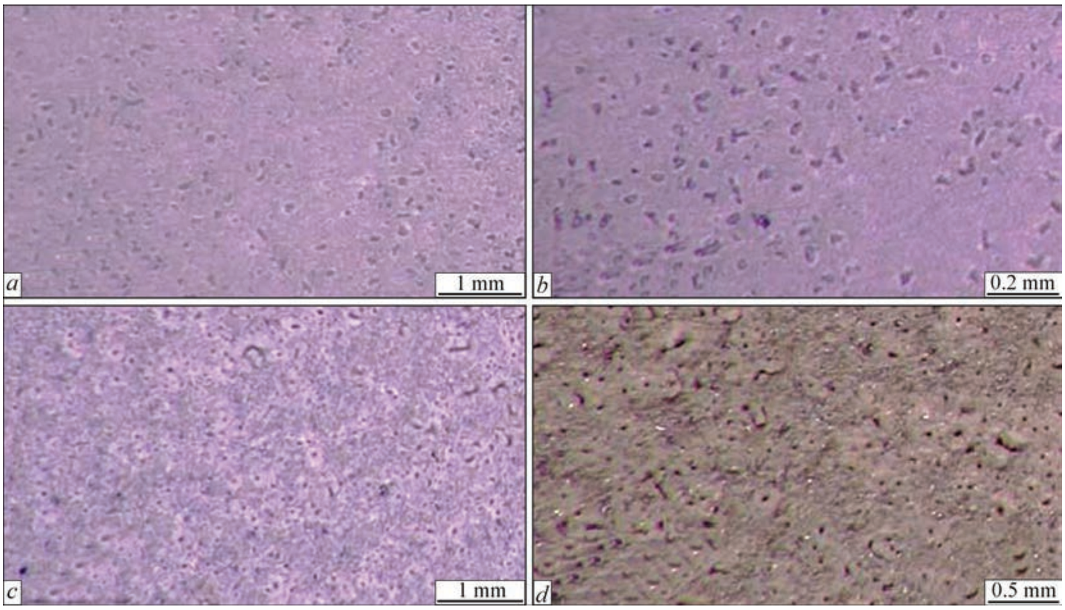

Figure 5. Surface of PEO-coatings synthesized in the following electrolytes: *a* — 5 g/l KOH + 5 g/l l.g + 5 g/l $Ca(OH)_2$ + 5 g/l $Na_6P_6O_{18}$ + 5 g/l $Na_4P_2O_7$; *b* — 5 g/l KOH + 5 g/l l.g + 5 g/l $Ca(OH)_2$ + 5 g/l $Na_6P_6O_{18}$ + 5 g/l $Na_4P_2O_7$ + 1 g/l HAp; *c* — 20 g/l KOH + 20 g/l l.g + 20 g/l $Na_6P_6O_{18}$ + 20 g/l $Na_4P_2O_7$; *d* — 20 g/l KOH + 20 g/l l.g + 20 g/l $Na_6P_6O_{18}$ + 20 g/l $Na_4P_2O_7$ + 20 g/l diatomite

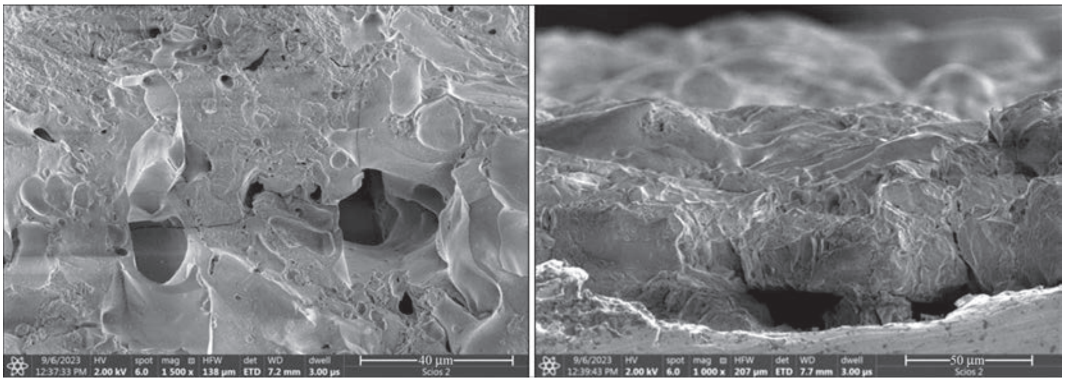

Figure 7. Fractogram of a coating at different magnifications, synthesized on a titanium alloy in the medium of 20 g/l l.g + 20 g/l KOH + 20 g/l $Na_4P_2O_7$ + 20 g/l $Na_6P_6O_{18}$ + 20 g/l diatomite at I_a/I_c = 10/10 A/dm^2, processing time of 30 min

coatings, synthesized in electrolytes with just the phosphates. Open porosity with 0.67 % values is inherent to coatings, synthesized in alkaline electrolyte of 3 g/l KOH + 2g/l liquid glass. The percentage of through-thickness porosity for coatings formed in a diatomite-containing medium decreases only slightly.

Studies of water absorption of the coatings revealed that the most porous of the mentioned coatings form in a diatomite-containing medium. Water absorption for such a kind of coatings is equal to 1.21 %, compared to coatings synthesized in electrolyte with 0.64 % phosphates, and in an alkaline electrolyte, containing just KOH and 0.61 % liquid glass.

Such results indicate that the coatings synthesized in a diatomite-containing electrolyte, are characterized by closed pores that is confirmed by fracture fractogram, shown in Figure 7.

One can see from this fractogram that pores in the coating have different dimensions, are surface melted and thus overlap. Such a result is positive as these are exactly the muscle tissues that can become embedded into the pores, leading to fast implant survival in the living body and shortening of the rehabilitation period.

CONCLUSIONS

1. The influence of the ratio of anode and cathode current density on the anode voltage was established under the conditions of biocoating synthesis by plasma electrolytic oxidation method on a titanium alloy. It was found that at I_a/I_c = 10/5 A/dm^2 in an electrolyte consisting of 2 g/l KOH + 3 g/l liquid glass, the anode voltage during PEO is the lowest, namely ~83 V, while among the selected experimental I_a/I_c ratios the highest value of anode voltage is ensured at I_a/I_c = = 50/40 A/dm^2.

2. Phosphate addition to electrolyte leads to a rapid increase of the anode voltage, which is increased twice, compared to phosphate-free electrolytes.

3. In phosphate electrolytes the coating is synthesized uniformly at the ratio I_a/I_c = 15/10 A/dm^2.

4. Addition of calcium-containing components to the electrolyte with pyrophosphate and sodium hexamethophosphate reduces the system energy consumption and stabilizes the coating formation process that is reflected in its uniformity over the entire surface.

5. Diatomite presence in the electrolyte greatly increases the conductivity of the working medium, that leads to anode voltage drop and removes the section of rapid voltage rise in the first minutes of coating synthesis, that is responsible for the breakdown of the oxide film on the titanium alloy in alkaline electrolytes, which contain only the components of potassium hydroxide and liquid glass.

6. It is found that PEO-coatings with the highest through-thickness porosity, equal to 0.75 %, form in an electrolyte of the composition of 0.5 g/l KOH + 0.5 g/l l.g + 0.5 g/l $Ca(OH)_2$ + 0.5 g/l $Na_6P_6O_{18}$ + 0.5 g/l $Na_4P_2O_7$.

7. Investigations revealed that in the coatings synthesized on a titanium alloy in an electrolyte of the composition of 20 g/l l.g + 20 g/l KOH + 20 g/l $Na_4P_2O_7$ + 20 g/l $Na_6P_6O_{18}$ + 20 g/l diatomite are characterized by a high water absorption, equal to 1.21 %, that is two times higher than this index for coatings, formed in a phosphate electrolyte and in an electrolyte without addition of other components.

REFERENCES

1. Imbirovych, N., Boyarska, I., Povstyanoy, O. et al. (2023) Modification of oxide coatings synthesized on zirconium alloy by the method of plasma electrolytic oxidation. *AIP Conf. Proc.*, 2949(**1**), 020011. DOI: https://doi.org/10.1063/5.0165655
2. Povstyanoy, O., Imbirovich, N., Redko, R. et al. (2024) *Numerical evaluation of the properties of highly efficient titanium porous materials*. Eds by V. Tonkonogyi. Advanced Manufacturing Processes InterPartner 2023. Lecture Notes in Mechanical Engineering. Springer, Cham., 307–317. DOI: https://doi.org/10.1007/978-3-031-42778-7_28
3. Duan, H., Yan, C., Wang, F. (2007) Growth process of plasma electrolytic oxidation films formed on magnesium alloy

AZ91D in silicate solution. *Electrochim. Acta*, 52(**12**), 5002–5009. DOI: https://doi.org/10.1016/j.electacta.2007.02.021

4. Tillous, K., Toll-Duchanoy, T., Bauer-Grosse, E. et al. (2009) Microstructure and phase composition of microarc oxidation surface layers formed on aluminium and its alloys 2214-T6 and 7050-T74. *Surf. Coat. Technol.*, 203(**19**), 2969–2973. DOI: https://doi.org/10.1016/j.surfcoat.2009.03.021
5. Curran, J.A., Clyne, T.W. (2005) Thermo-physical properties of plasma electrolytic oxide coatings on aluminium. *Surf. Coat. Technol*., 199(**2–3**), 168–176. DOI: https://doi.org/10.1016/j.surfcoat.2004.09.037
6. Petrosyanis, A.A., Malyshev, V.N., Fedorov, V.A., Markov, G.A. (1984) Wear kinetics of coatings made by microarcing oxidation. *Trenie i Iznos*, **5**, 350–354.
7. Student, M., Pohrelyuk, I., Padgurskas, J. et al. (2023) Influence of plasma electrolytic oxidation of cast Al-Si alloys on their phase composition and abrasive wear resistance. *Coatings*, 13(**3**), 637. DOI: https://doi.org/10.3390/coatings13030637
8. Yang, X., Ma, A., Liu, J. et al. (2019) Microstructure and corrosion resistance of yellow MAO coatings. *Surface Eng.*, 35(**4**), 334–342. DOI: https://doi.org/10.1080/02670844.2018.1445939
9. Mori, Y., Koshi, A., Jinsun Liao, J. et al. (2014) Characteristics and corrosion resistance of plasma electrolytic oxidation coatings on AZ31B Mg alloy formed in phosphate – Silicate mixture electrolytes. *Corrosion Sci.*, **88**, 254–262. DOI: https://doi.org/10.1016/j.corsci.2014.07.038
10. Nykyforchyn, H.M., Agarwala, V.S., Klapkiv, M.D., Posuvailo, V.M. (2008) Simultaneous reduction of wear and corrosion of titanium, magnesium and zirconium alloys by surface plasma electrolytic oxidation treatment. *Advanced Materials Research*, **38**, 27–35. DOI: https://doi.org/10.4028/www.scientific.net/AMR.38.27
11. Pauporté, T., Finne, J., Kahn-Harari, A., Lincot, D. (2005) Growth by plasma electrolysis of zirconium oxide films in the micrometer range. *Surf. Coat. Technol.*, 199(**2–3**), 213–219. DOI: https://doi.org/10.1016/j.surfcoat.2005.03.003
12. Timoshenko, A.V., Magurova, Yu.V. (2005) Investigation of plasma electrolytic oxidation processes of magnesium alloy MA2-1 under pulse polarisation modes. *Surf. Coat. Technol.*, 199(**2–3**), 135–140. DOI: https://doi.org/10.1016/j.surfcoat.2004.09.036
13. Zhou, H., Li, F., He, B. et al. (2007) Air plasma sprayed thermal barrier coatings on titanium alloy substrates. *Surf. Coat. Technol.*, 201(**16–17**), 7360–7367. DOI: https://doi.org/10.1016/j.surfcoat.2007.02.010
14. Shokouhfar, M., Dehghanian, C., Baradaran, A. (2011) Preparation of ceramic coating on Ti substrate by plasma electrolytic oxidation in different electrolytes and evaluation of its corrosion resistance. *Appl. Surf. Sci*., 257(**7**), 2617–2624. DOI: https://doi.org/10.1016/j.apsusc.2010.10.032
15. Stojadinovic, S., Vasilic, R., Petkovic, M. et al. (2010) Luminescence properties of oxide films formed by anodization of aluminum in 12-tungstophosphoric acid. *Electrochim. Acta*, 55(**12**), 3857–3863. DOI: https://doi.org/10.1016/j.electacta.2010.02.01
16. Snizhko, L.O., Yerokhin, A.L., Pilkington, A. et al. (2004) Anodic processes in plasma electrolytic oxidation of aluminium in alkaline solutions. *Electrochim. Acta*, 49(**13**), 2085–2095. DOI: https://doi.org/10.1016/j.electacta.2003.11.027
17. Stojadinović, S., Rastko, V., Petkovic, M., Zekovic, L. (2011) Plasma electrolytic oxidation of titanium in heteropolytungstate acids. *Surf. Coat. Technol.*, 206(**2–3**), 575–581. DOI: https://doi.org/10.1016/j.surfcoat.2011.07.090
18. Sundararajan, G., Rama Krishna, L. (2003) Mechanisms underlying the formation of thick alumina coatings through the MAO coating technology. *Surf. Coat. Technol*., 167(**2–3**), 269–277. DOI: https://doi.org/10.1016/S0257-8972(02)00918-0
19. Brewer, W.D., Bird, R.K., Wallace, T.A. (1998) Titanium alloys and processing for high speed aircraft. *Mater. Sci. and Engin.: A*, 243(**1–2**), 299–304. DOI: https://doi.org/10.1016/S0921-5093(97)00818-6 A 243(1998)299
20. Leyens, C., Peters, M. (2003) *Titanium and Titanium Alloys: Fundamentals and Applications*. Wiley-VCH, Weinheim, Germany. DOI: https://doi.org/10.1002/3527602119
21. Yao, Z.Q., Ivanisenko, Yu., Diemant, T. et al. (2010) Synthesis and properties of hydroxyapatite-containing porous titania coating on ultrafine-grained titanium by micro-arc oxidation. *Acta Biomater*., 6(**7**), 2816–2825. DOI: https://doi.org/10.116/j.actbio.2009.12.053
22. Hench, L.L. (1998) Biomaterials: A forecast for the future. *Biomaterials*, **19**, 1419–1423. DOI: https://doi.org/10.1016/s0142-9612(98)00133-1
23. Jae-Young Rho, Liisa Kuhn-Spearing, Peter Zioupos (1998) Mechanical properties and the hierarchical structure of bone. *Medical Engineering & Physics*, 20(**2**), 92–102. DOI: https://doi.org/10.1016/S1350-4533(98)00007-1
24. Dabdoub, S.M., Tsigarid, A.A., Kumar, P.S. (2013) Patient-specific analysis of periodontal and peri-implant microbiomes. *J. of Dental Research*, 92(**12**), 1685–1755. DOI: https://doi.org/10.1177/0022034513504950
25. Fakhr Nabavi, H., Aliofkhazraei, M. (2019) Morphology, composition and electrochemical properties of bioactive-TiO_2/HA on CP-Ti and Ti6Al4V substrates fabricated by alkali treatment of hybrid plasma electrolytic oxidation process (Estimation of porosity from EIS results). *Surf. Coat. Technol.*, **375**, 266–291, DOI: https://doi.org/10.1016/j.surfcoat.2019.07.032
26. Azmat, A., Asrar, S., Channa, I.A. et al. (2023) Comparative study of biocompatible titanium alloys containing non-toxic elements for orthopaedic implants. *Crystals,* **13**, 467. DOI: https://doi.org/10.3390/cryst13030467
27. Geetha, M., Singh, A.K., Asokamani, R., Gogia, A.K. (2009) Ti based biomaterials, the ultimate choice for orthopaedic implants. A review. *Progress in Mater. Sci.*, **54**, 397–425. DOI: https://doi.org/10.1016/j.pmatsci.2008.06.004
28. Zyman, Z.Z., Rokhmistrov, D.V., Glushko, V.I. (2010) Structural and compositional features of amorphous calcium phosphate at the early stage of precipitation. *J. Mater. Sci. Mater. Med*., 21(**1**), 123–130. DOI: https://doi.org/10.1007/s10856-009-3856-4
29. Furko, M., Balázsi, K., Balázsi, C. (2023) Calcium phosphate loaded biopolymer composites — A comprehensive review on the most recent progress and promising trends. *Coatings,* **13**, 360. DOI: https://doi.org/10.3390/coatings13020360
30. Colombo, P.V., Tanner, A.C.R. (2019) The role of bacterial biofilms in dental caries and periodontal and peri-implant diseases: A historical perspective. *J. Dent. Res*., 98(**4**), 373–385. DOI: https://doi.org/10.1177/0022034519830686
31. Mazinani, A., Nine, M.J., Chiesa, R. et al. (2021) Graphene oxide (GO) decorated on multi-structured porous titania fabricated by plasma electrolytic oxidation (PEO) for enhanced antibacterial performance. *Materials & Design*, **20**, 109443. DOI: https://doi.org/10.1016/j.matdes.2020.109443
32. Arash Fattah-alhosseini, Maryam Molaei, Navid Attarzadeh et al. (2020) On the enhanced antibacterial activity of plasma electrolytic oxidation (PEO) coatings that incorporate particles: A review. *Ceramics Intern.*, 46(**13**), 20587–20607 DOI: https://doi.org/10.1016/j.ceramint.2020.05.206

33. Totosko, O.V., Stukhlyak, P.D., Mykytyshyn, A.H., Levytskyi, V.V. (2020) Investigation of electrospark hydraulic shock influence on adhesive-cohesion characteristics of epoxy coatings. *Functional Materials*, 27(**4**), 760–766. DOI: https://doi.org/10.15407/fm27.04.760
34. Shu-Chuan Liao, Chia-Ti Chang, Chih-Ying Chen et al. (2020) Functionalization of pure titanium MAO coatings by surface modifications for biomedical applications. *Surf. Coat. Technol.*, **394**, 125812. DOI: https://doi.org/10.1016/j.surfcoat.2020.125812
35. Topal, E., Rajendran, H., Zgłobicka, I. et al. (2020) Numerical and experimental study of the mechanical response of diatom frustules. *Nanomaterials*, **10**, 959. DOI: https://doi.org/10.3390/nano10050959
36. Dunleavy, C.S., Golosnoy, I.O., Curran, J.A., Clyne, T.W. (2009) Characterization of discharge events during plasma electrolytic oxidation. *Surf. Coat. Tecnol.*, **203**, 3410–3419. DOI: https://doi.org/10.1016/j.surfcoat.2009.05.004
37. Wang, H.Y., Zhu, R.F., Lu, Y.P. et al. (2014) Preparation and properties of plasma electrolytic oxidation coating on sandblasted pure titanium by a combination treatment. *Mater. Sci. Eng. C. Mater. Biol. Appl.*, **42**, 657–664. DOI: https://doi.org/10.1016/j.msec.2014.06.005
38. Kang, B.S., Sul, Y.T., Johansson, C.B. et al. (2012) The effect of calcium ion concentration on the bone response to oxidized titanium implants. *Clinical Oral Implants Research*, **23**, 690–697. DOI: https://doi.org/10.1111/j.1600-0501.2011.02177.x
39. Wang, M.S., Lee, F.P., Shen, Y.D. et al. (2015) Surface, biocompatible and hemocompatible properties of meta-amorphous titanium oxide film. *Int. J. of Applied Ceramic Technology*, **12**, 341–350. DOI: https://doi.org/10.1111/ijac.12184

ORCID

N.Yu. Imbirovych: 0000-0001-8276-6349,
O.Yu. Povstyanoy: 0000-0002-1416-225X,
K.J. Kurdzydlowski: 0000-0003-3875-4820,
V.V. Tkachuk: 0009-0007-1875-4774

CONFLICT OF INTEREST

The Authors declare no conflict of interest

CORRESPONDING AUTHOR

N.Yu. Imbirovych
Lutsk National Technical University
75 Lvivska Str., 43018, Lutsk, Ukraine.
E-mail: n.imbirovych@lntu.edu.ua

SUGGESTED CITATION

N.Yu. Imbirovych, O.Yu. Povstyanoy, K.J. Kurdzydlowski, V.V. Tkachuk (2024) Formation of porous coatings on titanium alloys by the method of plasma electrolytic oxidation in alkaline electrolytes saturated with phosphates and bio-additives. *The Paton Welding J.*, **12**, 16–22.
DOI: https://doi.org/10.37434/tpwj2024.12.03

JOURNAL HOME PAGE

https://patonpublishinghouse.com/eng/journals/tpwj

Received: 17.07.2024
Received in revised form: 20.11.2024
Accepted: 27.12.2024

DOI: https://doi.org/10.37434/tpwj2024.12.04

RESIDUAL STRESSES INDUCED BY FRICTION STIR WELDING OF HEAT STRENGTHENED ALUMINIUM 2219-T81 ALLOY PLATES

O.V. Makhnenko, O.S. Milenin, V.I. Pavlovsky, V.V. Savitsky, B.R. Tsaryk

E.O. Paton Electric Welding Institute of the NASU
11 Kazymyr Malevych Str., 03150, Kyiv, Ukraine

ABSTRACT

Friction stir welding (FSW) is a relatively new welding process that has already been widely used for joining structures in the aerospace industry, transport and shipbuilding. It is believed that, in comparison with traditional arc welding processes, FSW provides less heating of the joint metal and a reduction in the level of residual stresses and strains. In the work, the features of the distribution of residual stresses induced by FSW in the butt joint of the heat strengthened aluminium alloy are investigated, which is necessary for predicting the strength and service life of welded structures. A mathematical model was built to determine the residual stresses at FSW, and the effect of softening of the aluminium alloy during heating in welding on the residual stresses was considered. The comparison of calculated and experimental data on the distribution of residual longitudinal stresses in FSW specimens showed a satisfactory level of their correspondence. It is shown that the determined level of residual tensile stresses is close to the yield strength of the annealed metal.

KEYWORDS: aluminium alloy, friction stir welding, butt joint, residual stresses, mathematical modelling, experimental measurement

INTRODUCTION

Today, friction stir welding (FSW) technology is widely used to join different structures in the aerospace industry, transport and shipbuilding, etc. [1, 2]. To predict the reliability, service life, strength, and durability of FSW welded structures, an urgent task is to determine the residual stresses and strains [3, 4]. In view of the fact that the process of introducing FSW in the industry of developed countries began not so long ago — the last few decades — the issue of residual stresses and strains at FSW of various structural materials and alloys is still understudied. Therefore, there is no generally accepted idea of the level of maximum values and the nature of distribution of residual stresses and strains, and the existing data are often contradictory. For this purpose, the methods of experimental studies of the stress-strain state of the butt joint of aluminium alloy 2219-T81 plates under FSW welding heating were used [5], and the obtained distributions of residual stresses at FSW with the results of mathematical modelling were compared.

EXPERIMENTAL MEASUREMENT OF RESIDUAL STRESSES AT FSW

The experimental determination of residual stresses in specimens of aluminium alloy 2219-T81 joints, produced using FSW technology, was performed. The residual welding stresses were measured by the following methods:

1. By the method of cutting the welded joint metal into narrow longitudinal strips (templates) to relieve inner stresses in them and measuring the elastic strains obtained in this way (residual welding longitudinal stresses) [9]. For this purpose, a mechanical strain gauge on a 20 mm base was used (Figure 1) and a system of conical holes preliminary drilled on the upper and lower sides of the specimen in the cross-sections in the middle part of the specimens. The measurements were performed by means of a mechanical strain gauge on each measuring base (20 mm) before and after a complete cutting of the specimens into templates to completely relieve the residual stresses. After that, the elastic strain data of each measuring base was converted into residual welding stresses at

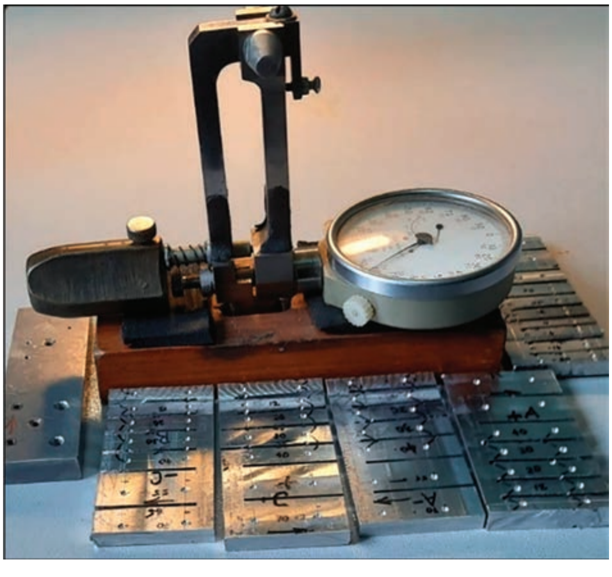

Figure 1. Appearance of mechanical strain gauge on a 20 mm base and cut-out parts of welded specimen (templates) with measuring bases (conical holes) for determination of residual stresses

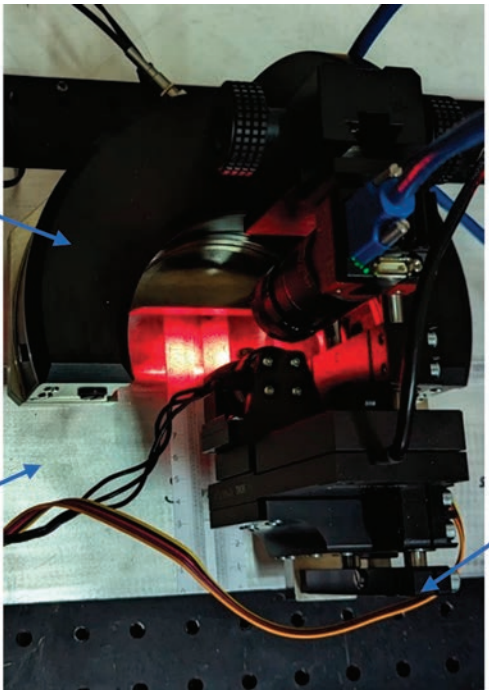

Figure 2. Appearance of ESPI-HD device for measurement of residual stresses

a set point of the specimen. For the aluminium alloy 2219, the modulus of elasticity $E = 75000$ MPa was used in the calculations.

2. By the hole method combined with the registration of displacements resulting from local stress relaxation using laser speckle interferometry (ESPI-HD method) (Figure 2). It does not require surface preparation and can be used to determine residual stresses on a base of 0.5–1.0 mm diameter and up to 1 mm depth. The measurements were performed in the following sequence: the speckle interferometer was placed on the welded joint, after which digital images were recorded, characterising the initial state of the surface before the hole was drilled. After the stress relaxation caused by drilling a 1.0 mm diameter and 0.5 mm depth through hole, another set of speckle images was recorded, that reflected the deformed state. Based on the obtained images, the displacement values in the specimen plane around the hole were calculated using the phase step method, which were used to determine residual stresses [10, 11]. The ESPI-HD method has demonstrated satisfactory agreement of stress measurement results with other traditional methods at the IIW Round-Robin test [12].

The specimen for measuring residual stresses represents a butt joint of two identical plates of 500 mm length, 300 mm width and 8 mm thickness. To measure residual elastic deformations, 26 measuring bases (52 holes) were used in the cross-section on both sides of the specimen (Figure 3).

The results of measuring residual longitudinal stresses in the specimen No. 1 in the central cross-section and in the specimen No. 2 in two cross-sections *A* and *B* (Figure 3) of the FSW butt joint specimen after

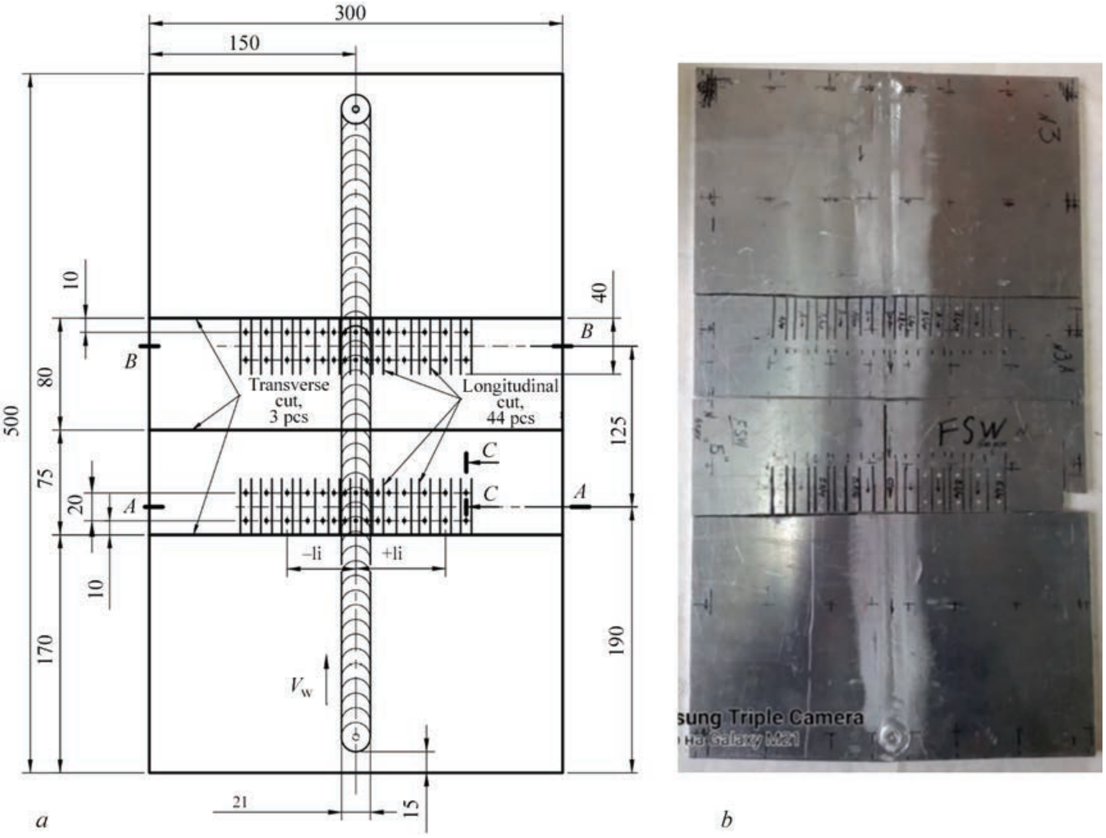

Figure 3. Layout of measuring bases (*a*) and appearance (*b*) of specimen (specimen No. 2) with dimensions of 500×300×8 mm of plates' butt joint according to the FSW technology

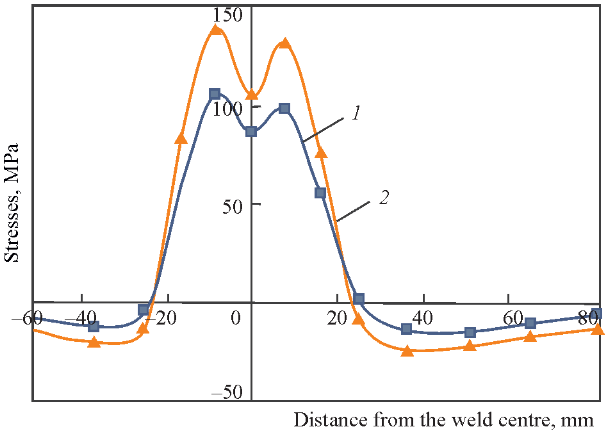

Figure 4. Residual longitudinal stresses in the central cross-section in the specimen No. 1 on the upper ($\sigma_{x,\ \mathrm{upper}}$) (*1*) and lower ($\sigma_{x,\ \mathrm{lower}}$) (*2*) sides of the specimen

a complete cutting of the material into longitudinal templates and measuring elastic deformations showed good repeatability of the results and a maximum level of tensile stresses of up to 180 MPa (Figures 4, 5). A significant difference was found between the level of residual longitudinal stresses on the upper and lower sides of the specimen. On the upper side, the level of measured stresses is noticeably lower: the maximum tensile stresses do not exceed 80–100 MPa, while on the lower side they reach 180 MPa. A significant bending component of the longitudinal stresses across the thickness is confirmed by the presence of a residual longitudinal deflection of the central part of the specimen of up to 2.5 mm.

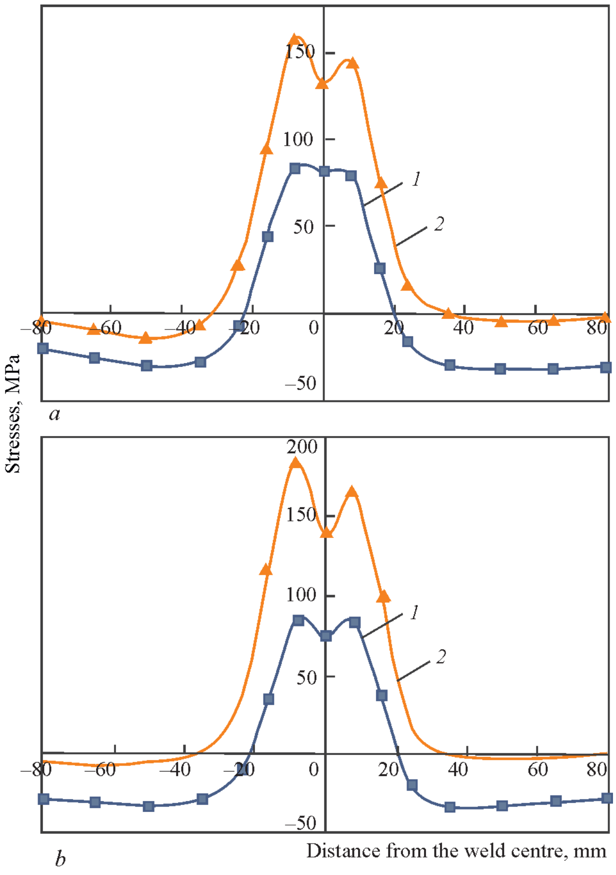

Figure 5. Experimental distributions of residual longitudinal stresses on both upper (*1*) and lower (*2*) sides of the weld specimen No. 2 in the cross-sections *A–A* (*a*) and *B–B* (*b*)

The measurements by the speckle interferometry method (using drilling holes of 1 mm diameter) were carried out on the specimen No. 1 in two cross-sections: section 1 at a distance of 130 mm from the beginning of the weld and section 2 at a distance of 350 mm. In the section 1, the measurements were obtained on the upper and lower sides of the specimen, and in the section 2 — only on the lower side, in the zone of high tensile stresses. The measurement results showed (Figure 6, *a*) that the tensile longitudinal stresses on the upper side do not exceed 120–150 MPa, and on the lower side they reach 200–210 MPa. The remaining components of residual stresses have significantly lower values: transverse tensile stresses on the upper side do not exceed 20–25 MPa, and 50 MPa on the lower side (Figure 6, *b*).

The results of the stress state determination in the specimen No. 1 by two methods showed that at friction stir welding, the values of the maximum residual longitudinal stresses are quite high and close to the yield strength of the aluminium alloy A2219 in the annealed state (up to 150–180 MPa), i.e., taking into account the material softening in the welding heating

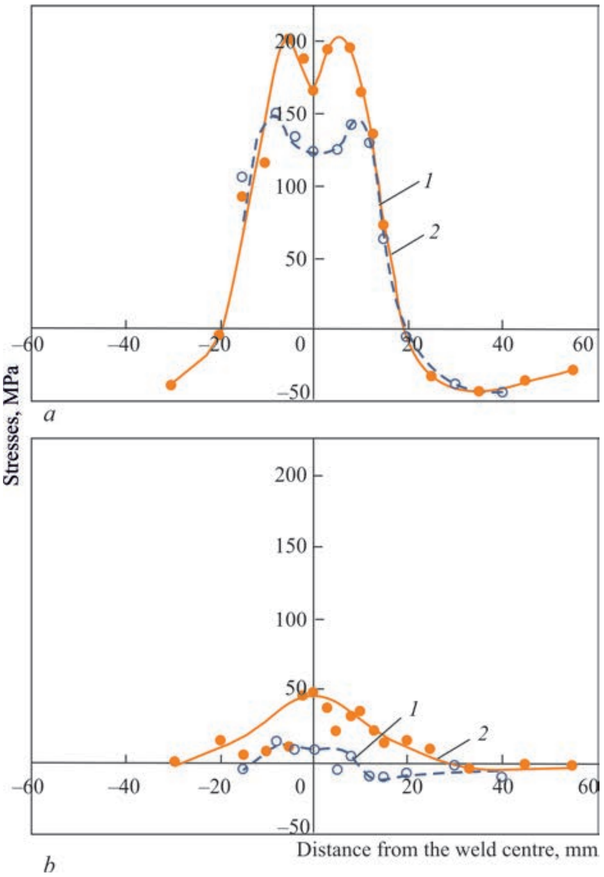

Figure 6. Results of measuring residual stresses by speckle interferometry in the specimen No. 1: *a* — longitudinal component; *b* — transverse component; *1* — upper side of the specimen; *2* — lower side of the welded specimen

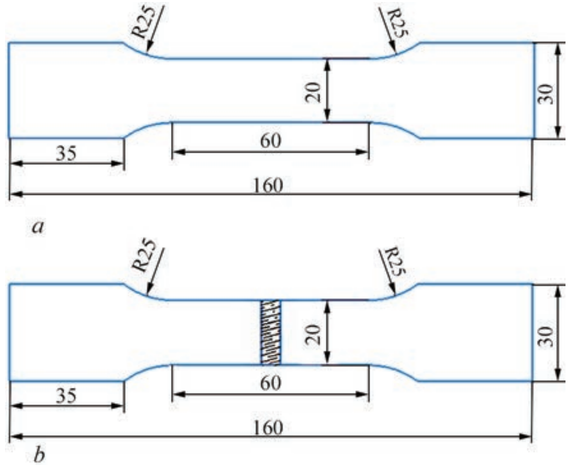

Figure 7. Diagrams of tensile specimens of the base metal (*a*) and welded joint metal (*b*)

zone. At the same time, residual stresses on the lower side of the specimen are significantly higher than those measured on the upper side: longitudinal stresses — by 20–30 %, transverse stresses — by 5 times.

MEASUREMENT OF MECHANICAL CHARACTERISTICS OF WELDED JOINT MATERIAL

The mechanical properties of welded specimens' material were studied. For uniaxial tensile tests, 10 tensile specimens were made from the base material (Figure 7, *a*) in two mutually perpendicular directions to determine the direction of rolled products. The welded joint metal is much less dependent on the direction of rolling due to the weld metal and HAZ recrystallization during the welding process. Thus, 10 specimens were used for these tests (Figure 7, *b*).

The test results showed that the influence of the rolling direction on the mechanical properties of welded specimen material does not exceed 4.5 %. This allows ignoring the material anisotropy when making the relevant expert assessments using the minimum average value ($\sigma_{0.2}$ = 370 MPa, E = 75.3 GPa). In addition, the process of metal recrystallization in the weld area has a significant impact, where a significant softening of the metal occurs: a decrease in the ultimate tensile strength σ_t to 44.4 % and in the true yield strength $\sigma_{0.2}$ to 63.4 % compared to the base material specimen along the rolled product.

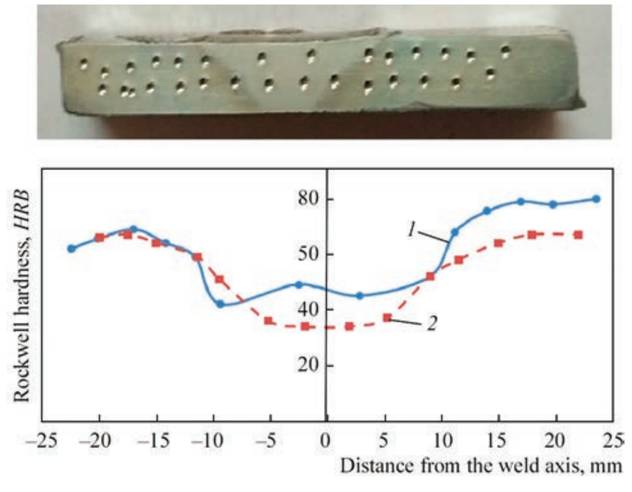

Figure 8. Rockwell hardness distribution in the FSW joint of the alloy A2219-T81 plates: *1* — upper side of the specimen; *2* — lower side of the specimen

According to the results of Rockwell hardness measurements in the cross-section of the test specimen (Figure 8), it was determined that in the welded joint zone in the HAZ, a material softening zone of ~20 mm width was observed, where the hardness characteristics were reduced by almost half, from an average of 70 to 35 *HRB*. This is also agreed with a decrease in the strength characteristics of the material for the alloy A2219-T81 in the HAZ, namely the yield strength from 350 to 160 MPa, determined as a result of mechanical tensile tests of the specimens.

COMPARISON WITH THE RESULTS OF MATHEMATICAL MODELLING OF FSW

For mathematical modelling of residual stresses at FSW of the aluminium alloy, the previously developed model [5] was used, which was supplemented by taking into account the effect of material softening in the weld zone and HAZ.

Temperature model:

$$c\rho\frac{\partial T}{\partial t}=\frac{\partial}{\partial x}\left(\lambda\frac{\partial T}{\partial x}\right)+ +\frac{\partial}{\partial y}\left(\lambda\frac{\partial T}{\partial y}\right)+\frac{\partial}{\partial z}\left(\lambda\frac{\partial T}{\partial z}\right)+W(x,y,z,t), \tag{1}$$

where T is the temperature, °C; c is the specific heat capacity, J/kg·°C; ρ is the density, kg/m^3; λ is the thermal conductivity coefficient, W/m·°C; $W(x, y, z, t)$ is the power of volumetric heat generation, W/m^3.

The peculiarity of the developed model of the heating source at FSW is heat generation due to the friction of the tool relative to the joint material. The tool rotates around a vertical axis with a certain rotational velocity ω, rpm, and is pressed against the plates with an axial force P_n, Pa, which generates a heat flux into the joint material on the tool contact surface, W/m^2:

$$\lambda\frac{\partial T}{\partial n}=\mu P_n\omega r, \tag{2}$$

where μ is the friction coefficient; $r=\sqrt{(x-x_0-v_w t)^2+(y-y_0)^2}$ — is the distance of the considered contact point from the axis of the working tool rotation, $(x_0 + v_w t, y_0)$, v_w is the linear speed of the tool movement.

Then, the heat generation power Q, W, on the corresponding contact surfaces with an area S (Figure 9):

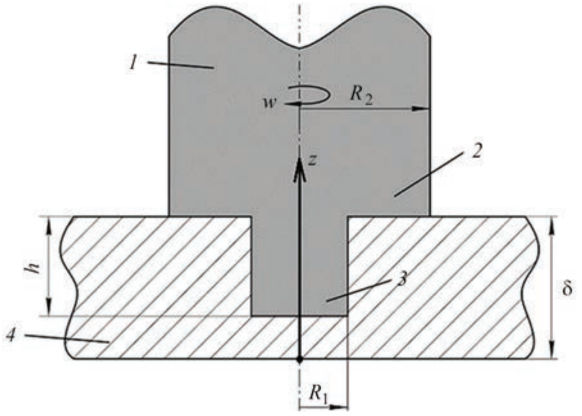

Figure 9. Schematic of FSW working tool: *1* — tool; *2* — shoulder; *3* — pin; *4* — plate

$$Q = \mu P_n \omega \pi \iint_s r dS; \quad (3)$$

arm

$$(z = \delta,\ R_1<r<R_2),\ Q_1 = \frac{2\pi}{3}\mu P_n \omega (R_2^3 - R_1^3);$$

lateral surface of the pin

$$(\delta - h < z < \delta,\ r = R_1),\ Q_2 = 2\pi\mu P_n \omega R_1^2 h;$$

lower end surface of the pin

$$(z = \delta - h,\ 0 > r > R_1),\ Q_3 = \frac{2\pi}{3}\mu P_n \omega R_1^3,$$

where δ is the thickness of the plates to be welded, m; *h* is the length of the pin entering the material, m.

Accordingly, the power of volumetric heat generation $W(x, y, z, t)$, W/m^3, consists of two components. The first is associated with heat generation in the volume V_1 on the upper side of the joining plates under the tool arm $(\delta - dz < z < \delta,\ R_1 < r < R_2)$, dz is the size of the finite element, and the second one is in the volume of the pin V_2 $(\delta - h < z < \delta,\ 0 > r > R_1)$:

$$W(x, y, z, t) = W_1 + W_2;$$

$$W_1 = \frac{Q_1}{V_1} = \frac{\frac{2\pi}{3}\mu P_n \omega (R_2^3 - R_1^3)}{\pi (R_2^2 - R_1^2) dz} = \frac{2\mu P_n \omega (R_2^2 + R_2 R_1 + R_1^2)}{3(R_2 + R_1) dz}; \quad (4)$$

$$W_2 = \frac{Q_2 + Q_3}{V_2} = \frac{2\pi\mu P_n \omega R_1^2 h + \frac{2\pi}{3}\mu P_n \omega R_1^3}{\pi R_1^2 h} = 2\mu P_n \omega \left(1 + \frac{R_1}{3h}\right).$$

The model of thermoplastic deformation of the welded joint material at FSW is based on the assumption that the process of stirring the welded joint material occurs in the weld zone at a sufficiently high temperature and does not significantly affect the overall result of the formation and propagation of plastic deformations in the HAZ material and the weld behind the working tool. Therefore, plastic deformations and residual stresses are formed only as a result of the temperature gradient that occurs when the working tool moves as a source of volumetric heat generation [4]. The proposed mathematical model of thermoplastic deformation of the welded joint material at FSW is presented in more detail in [5].

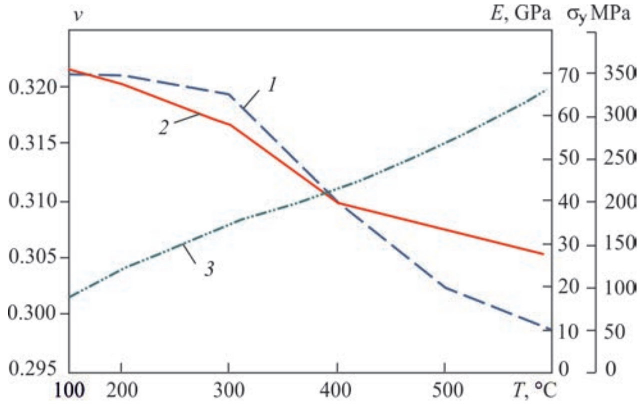

Figure 10. Mechanical properties of the alloy 2219-T81: *1* — $\sigma_y(T)$; *2* — $E(T)$; *3* — $v(T)$

In order to simplify the model, it was assumed that the value of the friction coefficient is independent of temperature and is approximately equal to the average value μ = 0.4 obtained for the aluminium alloy 2219 in the material temperature range of up to 400 °C [8].

Figures 10, 11 show the mechanical and thermophysical properties of the alloy 2219-T81 as a function of temperature [6], which were used in the mathematical modelling.

The analysis of the results of numerical experiments showed that among the factors that can to a greater or lesser extent influence the formation of residual stresses in the welded joint at FSW of aluminium alloys, softening of the material by welding heating has the greatest effect [7].

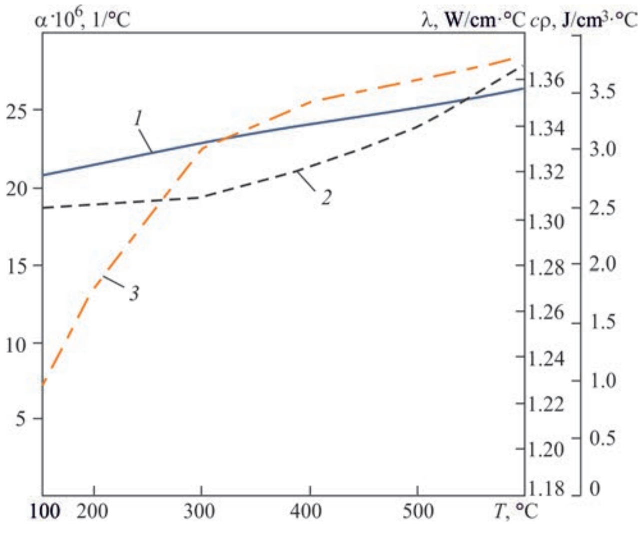

Figure 11. Thermophysical properties of the alloy 2219-T81: *1* — $\alpha(T)$; *2* — $c\rho(T)$; *3* — $\lambda(T)$

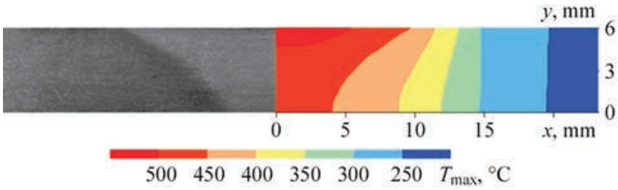

Figure 12. Comparison of the calculated distribution of the maximum temperatures in the cross-section of the FSW welded joint with the HAZ shape on the macrosection

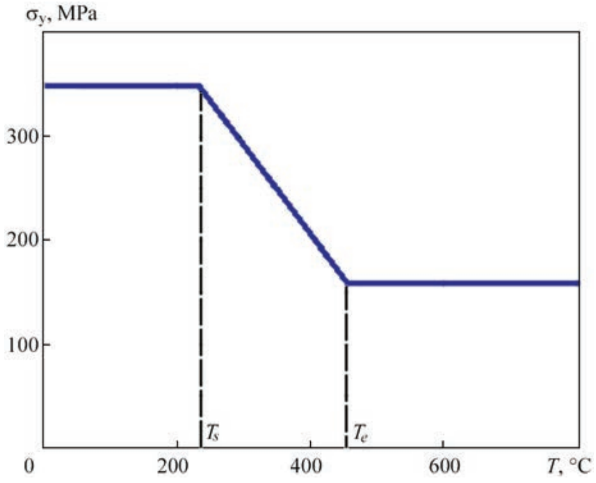

Figure 13. Dependence of the yield strength at 20 °C of the alloy A2219-T81 specimen on the maximum temperature in welding: T_s = 240 °C, T_e = 450 °C, σ_{soft} = 160 MPa, σ_y = 350 MPa

Comparison of the calculated distribution of maximum temperatures in the cross-section of the FSW welded joint of alloy A2219-T81 plates (Figure 12) with the results of hardness measurements (see Figure 8) showed that the width of the softening start zone of 40 mm corresponds to a temperature of T_s = 240 °C, and the zone of the maximum softening on the upper side with a width of ~20 mm and on the lower side with a width of 10 mm determines the temperature of softening end at the level of T_e = 450 °C of the material heating in welding.

The material softening parameters accepted in the model include the yield strength of the softened material σ_{soft} = 160 MPa, as well as the start temperature T_s = 240 °C and the end temperature T_e = 450 °C of softening (Figure 13). In the mathematical modelling of SSS at FSW, disregard of the material softening leads to a significant increase (by more than 30 %) in the maximum longitudinal residual stresses.

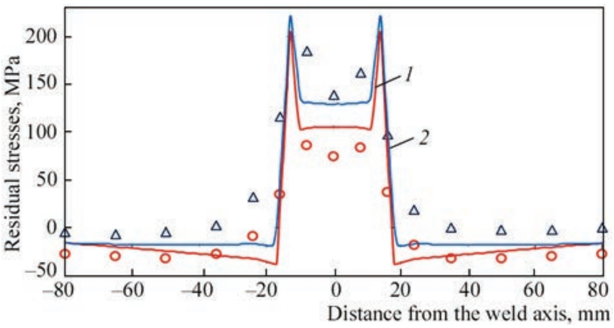

Figure 14. Comparison of experimental data with the results of mathematical modelling of the distribution of residual longitudinal stresses for the FSW specimen: experimental data: 0 — upper side of the specimen; Δ — lower side of the specimen; calculated data: *1* — upper side of the specimen; *2* — lower side of the specimen

Comparing the calculation results and the experimental data obtained on the specimen No. 2, based on the distribution of residual longitudinal stresses at FSW (Figure 14), it can be stated that the nature of the distribution of the calculated residual stresses is close to the experimental one. In the centre of the welded joint, there is a zone of significant reduction in tensile longitudinal stresses, which is associated with the softening effect of the aluminium alloy. The width of the tensile stress zone is approximately 36 mm (–18–+18 mm) and is the same for both experimental and calculated data.

The calculated stress distribution is characterised by sharper gradients and higher stress values in the weld zone. The smoother curve of the experimental residual stress distribution is associated with the sufficiently large step (8 mm) between the measurement points, which leads to an averaging of the stress values.

It is important that the experimental and calculated data are characterised by a significant difference between the stresses on the upper and lower sides of the welded joint — the residual longitudinal stresses are higher on the lower side. In terms of the absolute value of tensile stresses in the centre of the welded joint, this difference reaches 140 according to the experimental data and 130 MPa according to the calculation.

An assessment of the error of the calculated data for FSW shows that in the tensile stress zone (3 central points, –16–+16 mm), the mean square deviation from the experimental values on the lower side of the specimen is 21 %, and on the upper side it is up to 30 %. This error can be considered satisfactory, given the complex nature of the residual stress distribution.

CONCLUSIONS

1. For 8 mm thick specimens of welded butt joints made of the aluminium alloy A2219-T81 by friction stir welding, the measured level of tensile residual longitudinal stresses was quite high (up to 180 MPa), close to the yield strength of the aluminium alloy in the annealed state. At the same time, the residual stresses on the lower side of the specimen are higher than on the upper side (by about 20 %). The transverse tensile residual stresses are significantly lower: on the upper side they do not exceed 20–25 MPa, and on the lower side they do not exceed 50 MPa.

2. The result of mathematical modelling of residual stresses at FSW of aluminium alloys is significant-

ly influenced by considering the material softening model in the welding heating zone, the parameters of which include the yield strength of the softened material σ_{soft}, as well as the temperature range of the start T_s and end T_e of the softening effect. Disregard of the material softening leads to a significant increase (by more than 30 %) in the maximum longitudinal residual stresses.

REFERENCES

1. Hattel, J.H., Sonne, M.R., Tutum, C.C. (2015) Modelling residual stresses in friction stir welding of Al alloys— A review of possibilities and future trends. *Int. J. Adv. Manuf. Technol.*, **76**, 1793–1805. DOI: https://doi.org/10.1007/s00170-014-6394-2
2. Poklyatskyi, A.G., Motrunich, S.I., Fedorchuk, V.Ye. et al. (2023) Mechanical properties and structural features of butt joints produced at FSW of aluminium alloys of different alloying systems. *The Paton Welding J.*, **4**, 3–10. DOI: https://doi.org/10.37434/tpwj2023.04.01
3. Feng, Z., Wang, X.-L., David, S.A., Sklad, P.S. (2007) Modelling of residual stresses and property distributions in friction stir welds of aluminium alloy 6061-T6. *Sci. and Technol. of Welding and Joining*, 12(**4**), 348–356. DOI: https://doi.org/10.1179/174329307X197610
4. Mohammad Riahi, Hamidreza Nazari (2011) Analysis of transient temperature and residual thermal stresses in friction stir welding of aluminum alloy 6061-T6 via numerical simulation. *Int. J. Adv. Manuf. Technol.*, **55**, 143–152. DOI: https://doi.org/10.1007/s00170-010-3038-z
5. Tsaryk, B.R., Muzhychenko, O.F., Makhnenko,O.V. (2022) Mathematical model of determination of residual stresses and strains in friction stir welding of aluminium alloy. *The Paton Welding J.*, **9**, 33–40. DOI: https://doi.org/10.37434/tpwj2022.09.06
6. Abdulrahaman Shuaibu Ahmad, Yunxin Wu, Hai Gong, Lin Nie (2019) Finite element prediction of residual stress and deformation induced by double-pass TIG welding of Al 2219 plate. *Materials*, 12(**14**), 2251. DOI: https://doi.org/10.3390/ma12142251
7. Makhnenko, O.V., Tsaryk, B.R. (2024) Consideration of material softening in the calculated determination of residual stresses at welding of aluminum alloy 2219-T81. In: *Proc. of 14th Int. Sci.-Pract. Conf. on Comprehensive Quality Assurance of Technological Processes and Systems, May 23–24, 2024, Chernihiv*, Chernihiv Polytechnic National University, NU Chernigivska Politekhnika, Vol. 2, 110–111.
8. Aziz, S.B., Dewan, M.W., Huggett, D.J. et al. (2016) Impact of friction stir welding (FSW) process parameters on thermal modeling and heat generation of aluminum alloy joints. *Acta Metal. Sin.*, **29**, 869–883. DOI: https://doi.org/10.1007/s40195-016-0466-2
9. Kasatkin, B.S., Kudrin, A.B., Lobanov, L.M. (1981) *Experimental methods for studying deformations and stresses.* Kyiv, Naukova Dumka [in Russian].
10. Lobanov, L.M., Pivtorak, V.A., Savitsky, V.V. et al. (2005) Express control of quality and stressed state of welded structures using methods of electron shearography and speckle-interferometry. *The Paton Welding J.*, **8**, 35–40.
11. Lobanov, L., Pivtorak, V., Savitsky, V., Tkachuk, G. (2014) Technology and equipment for determination of residual stresses in welded structures based on the application of electron speckle-interferometry. *Mat. Sci. Forum*, **768–769**, 166–173. DOI: https://doi.org/10.4028/www.scientific.net/MSF.768-769.166
12. Wohlfahrt, H., Nitschkepagel, T., Dilger, K. et al. (2012) Residual stress calculations and measurements — review and asessment of the IIW round robin results. *Weld. World*, **56**, 120–140. DOI: https://doi.org/10.1007/BF03321387

ORCID

O.V. Makhnenko: 0000-0002-8583-0163,
O.S. Milenin: 0000-0002-9465-7710,
V.I. Pavlovsky: 0000-0002-5441-3447,
V.V. Savitsky: 0000-0002-2615-1793,
B.R. Tsaryk: 0000-0002-8929-7722

CONFLICT OF INTEREST

The Authors declare no conflict of interest

CORRESPONDING AUTHOR

O.V. Makhnenko
E.O. Paton Electric Welding Institute of the NASU
11 Kazymyr Malevych Str., 03150, Kyiv, Ukraine.
E-mail: makhnenko@paton.kiev.ua

SUGGESTED CITATION

O.V. Makhnenko, O.S. Milenin, V.I. Pavlovsky, V.V. Savitsky, B.R. Tsaryk (2024) Residual stresses induced by friction stir welding of heat strengthened aluminium 2219-T81 alloy plates. *The Paton Welding J.*, **12**, 23–29.
DOI: https://doi.org/10.37434/tpwj2024.12.04

JOURNAL HOME PAGE

https://patonpublishinghouse.com/eng/journals/tpwj

Received: 15.08.2024
Received in revised form: 30.09.2024
Accepted: 27.12.2024

DOI: https://doi.org/10.37434/tpwj2024.12.05

EVALUATION OF THE MECHANICAL CHARACTERISTICS OF CFRP COMPOSITES AND MODELING OF THE DELAMINATION PHENOMENON

A. Savin[1,2], **R. Steigmann**[1], **M.D. Stanciu**[2], **C.I. Moraras**[3], **G. Dobrescu**[1]

[1]Nondestructive testing Department, National Institute of R&D for Technical Physics, Iasi
15 D. Mangeron Blvd, Iasi 700050, Romania
[2]Faculty of Mechanical Engineering, Transilvania University of Brașov
29 Eroilor Blvd., 500036 Brașov, Romania
[3]Faculty of Mechanical Engineering, Technical University Gh. Asachi Iasi, Romania
45 D. Mangeron Blvd, Iasi 700050, Romania

ABSTRACT

In the category of new and advanced materials, carbon fiber reinforced plastic (CFRP) composite materials are used in areas such as structural materials in aeronautics, transport, etc. The bi-phasic structure of CFRP requires knowledge of both fiber and matrix properties. In the conditions where possible delamination's occur during use, these depend both on the properties of the interfaces and of the interlaminate. The appropriate ultrasound (US) techniques allow the determination of the propagation speed of the longitudinal and transverse waves which are used in the evaluation of the elastic modulus E, shear modulus G on the three principal directions. C-scan US using phased array allows the emphasizing and characterization of ones with porosities that appear during composite fabrication or due to local overheating. The results are compared with those obtained by a dynamic mechanical analyzer (DMA), being found a good correlation. These procedures allow also the emphasizing of matrix damages due to high temperature used or establishing maximum temperature for used.

KEYWORDS: CFRP, nondestructive testing, ultrasound, DMA

INTRODUCTION

The weight reduction of the components used in the aeronautical industry as well as that of the motor vehicles aims to reduce energy consumption and recommends composite materials as modular construction elements. The choice and use of composites related to performance and costs [1, 2] it is a direct concern. Increasing the lifespan of vehicles and the impact of vibrations and noises for external insulation as well as shock energy absorption are also problems that concern the car manufacturing industry and not only this one [3]. The applications follow the analysis of the mechanical behavior of these modular components as well as the connections between the composite and metallic structures, aiming to stop the initiation of failure. Carbon fiber reinforced composites (CFRP) are used in most fields and due to their low density, reduced effect of mechanical fatigue phenomena and high strength-to-weight ratio [4, 5]. However, the composites have low impact resistance in the direction normal to the fiber plane, being able to produce fiber delamination/rupture at high energies. The behavior of interlaminar fractures of the composites requires experimental investigation both as reinforcement and matrix. This can be done through non-destructive testing methods based on ultrasound, eddy currents, etc.

Epoxy resin is the most common matrix for CFRP [6], its properties are superior but with the aging process they are susceptible to water absorption [7], due to the polar hydroxyl group inside [8]. Although they are used in a significant amount, they present, like any new material, shortcomings related to performance, processing and costs [9, 10]. There are many researches that analyze the phenomena of delaminations in layered composites, many of them being due to impact, but the stresses inside the materials that appear during their lifetime, permanently monitored, determine the moment when a part, structure or assembly can no longer fulfill its characteristics operation. Sustained stresses of the joint components of composites or in adhesives can be undiagnosed causes that produce crack initiation [11]. The spatial arrangement, as well as the size of the product, can sometimes save the composite structure from failure.

The purpose of the paper is to present the complementary results (using theoretical and experimental methods) obtained in the complex investigation of the elastic properties of composites reinforced with carbon fibers.

MATERIALS AND METHODS

The behavior of CFRP composites under load is useful for understanding how loading affects complex CFRP composite structures, the study being doubled

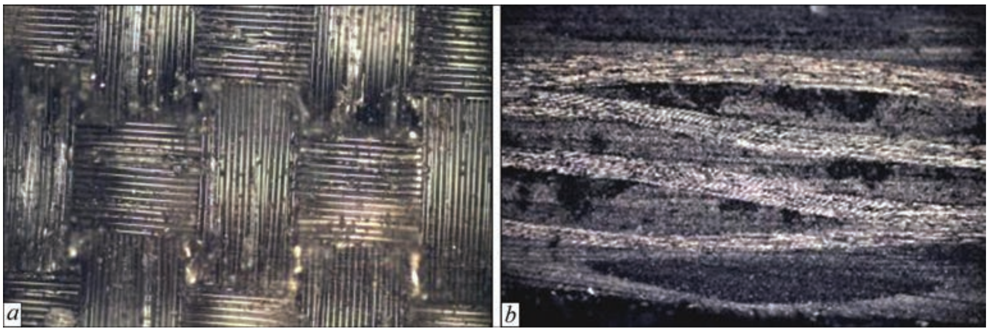

Figure 1. Studied samples: 10× front surface sample (*a*); cross section — optical microscope (*b*)

by analytical modeling to explain the results obtained during the experimental tests [12]. During the tests, large stress concentrators may appear that lead to an unknown mixed loading mode, variable along the sample, which can generate unexpected results.

2.1. SAMPLES MANUFACTURING

The composite materials proposed for theoretical and experimental analysis are CFRP type made using carbon/epoxy laminates manufactured by autoclave processing technology. Studies on the construction behavior of CFRP composites have demonstrated that the properties depend on the applied technology [13, 14]. In [15] the method of obtaining the laminates used in the tests presented in the paper is presented, CFRP with 8 plies of plain weave fabrics GG200P-PL1/1 (SLG group) with fiber diameter 7 μm Torayca T300 fibers [16] with different ply stacking sequences $[0]_8$ and $[(45/0)2]_s$ and ET445 resin. Made in the form of boards with dimensions 295×205 mm^2, thickness of 2.2 mm and volume ratio $V_f = 0.45$, density of 1.58 kg/dm^3, the realized configuration provides the laminate with a quasi-isotropic structure, having a modulus of elasticity of 0.44 ± 0.03.In the case of the analyzed composite, the polymer matrix ensures the adhesion between the fibers and the matrix and gives it a structure that resists until the fibers break. Plain fabric provides a simple repeating pattern Figure 1.

Besides the working conditions and the degree of loading, the architecture of the composite, the polymer matrix and the structure of the fibers can determine microstructural accumulations in the general damage mechanism.

2.2. FINITE ELEMENT ANALYSIS (FEA)

Finite element analysis allows obtaining detailed information on the distribution of stresses and deformations in the composite, following the optimization of the design and its performance. The 3D graphic model made in SolidWorks was imported into Ansys software version R17.0., Figure 2.

For the simulation, the quadrilateral discretization method was used, the table was uniformized and a function of the size of the elements of 1mm was introduced to ensure accuracy, obtaining a geometry of the section having 22505 nodes and 3936 elements. The sample was considered without discontinuities, from its surface (the one caught between the ends) only a portion was used in the study (Figure 2), the simulation was made for the tensile test. Figure 2, *b* shows the stress state in the tensile specimen. One can observe the stress distribution over its entire cross-section throughout its volume with maximum values at the level of the tabs that continue towards the central area.

2.3. METHODS

The presence of porosity in the composite material was analyzed using the ultrasound (US) method, the elastic waves being produced in CFRP with the Phasor XS equipment coupled with a sensor array with central frequency 5 MHz and a delay line. US attenuation in composites is a measure of the degree of porosity. The analysis of US propagation speeds in composites was obtained using transducers connected to a US PR 5073 Pulser Receiver — Panametrics equipment.

As the composite plates are thin for reflected US analysis, a Plexiglas delay line was applied. The compression waves were excited with a G5KB GE trans-

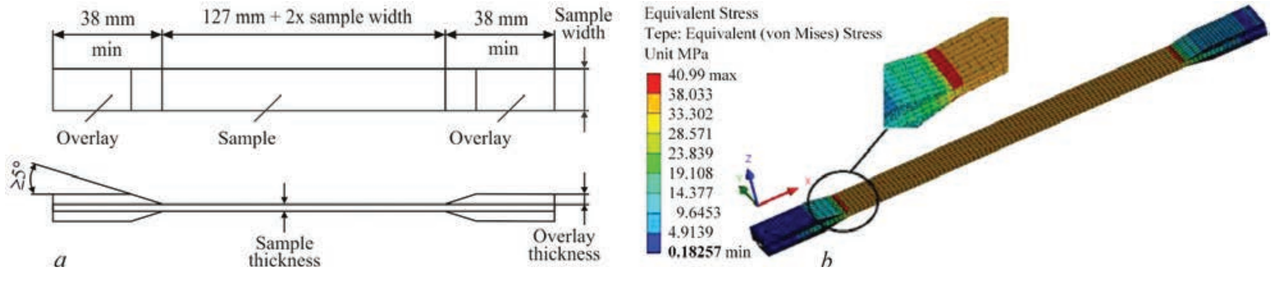

Figure 2. 3D model made in SolidWorks (*a*); the sample with the mesh structure and the analyzed section (*b*)

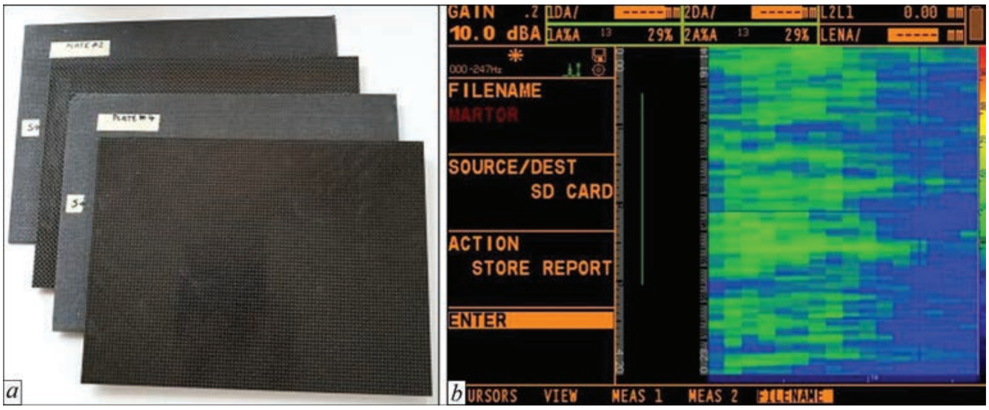

Figure 3. The CFRP specimens (*a*); the propagation C scan modes of US waves (*b*)

ducer with a central frequency of 5 MHz, the shear ones with a MB4Y transducer with a central frequency of 4 MHz, the signals were analyzed on the screen of a Le Croy Wave Runer64Xi digital oscilloscope. The values of the modulus of elasticity and the elastic properties of the composite are determined from the wave propagation speeds,

$$C_T=\sqrt{\frac{E}{\rho}\frac{1}{2(1+\nu)}};$$

$$C_L=\sqrt{\frac{E}{\rho}\frac{1-\upsilon}{(1+\nu)(1-2\nu)}}\ \text{and}\ C_T=\sqrt{\frac{G}{\rho}}. \qquad (1)$$

Knowing that E — elastic modulus; G — the shear modulus; ν — the Poisson coefficient and ρ — the density.

The Dynamic Mechanical Analyzer equipment, DMA 242C — Netzsch Germany, with the 3-point bending device using Protheus software v.4.8.5 was used to determine the main characteristic quantities, elastic modulus along the principally axis (E_x, E_y, E_z). The obtained values were compared with those determined by traction tests by classical procedure using INSTRON E1000 machine with hydraulic fixture.

EXPERIMENTAL RESULTS

The degree of porosity is in linear correlation with the attenuation of US in composites and with the mechanical properties ie shear resistance. The plates thus prepared (&2.1) were scanned with US at a single sweep of the 5 MHz frequency transducer moved with the ENCSTD axial scanner. The procedure applied to the material leads to the analysis of the scan image results shown in Figure 3.

The presence of localized porosity represents a break in the continuity of the environment. It can be observed that in this case the recorded measurements show a material without discontinuities.

Using the US technique to determine the longitudinal and transverse wave propagation speeds in the material, the elasticity modulus E_2 and the shear modulus G_{12} were determined. The average US propagation speed for longitudinal waves was C_l = 2732 and C_t = 1937 m/s for transverse ones.

From the CFRP samples, tested with US to ensure the absence of discontinuities, samples with dimensions of 50×10×2.2 mm^3 were cut for the DMA dynamic mechanical analysis. These samples were analyzed optically, because during the cutting process discontinuities may appear, some lamellas may change their direction

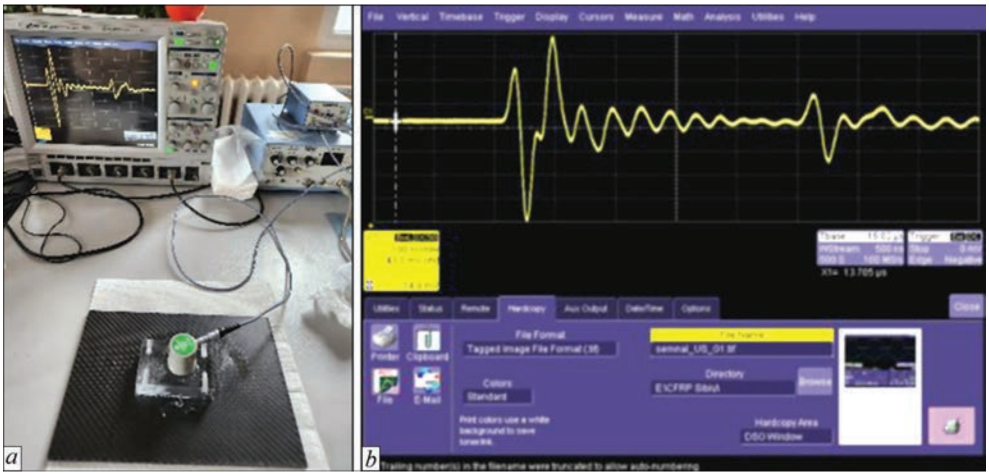

Figure 4. Determination of the speed of ultrasound propagation in the analyzed samples

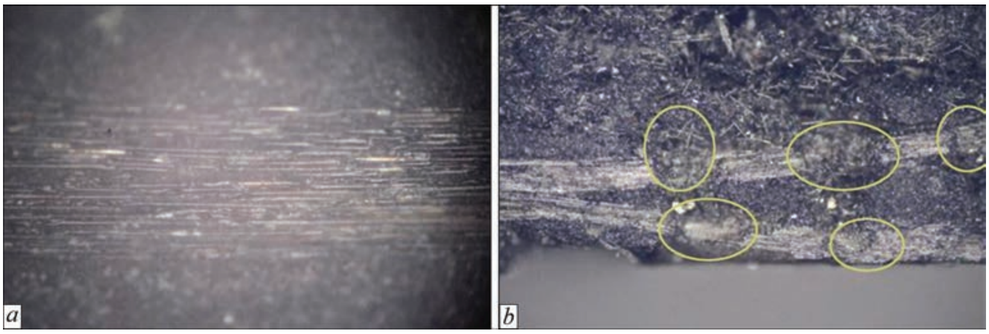

Figure 5. Cross-section microscope images of the DMA tested samples

Table 1. Elastic characteristics of studied samples

E_x, GPa	E_y, GPa	E_z, GPa	ν_{xy}	ν_{yx}	ν_{xz}	G_{xy}, GPa	G_{yx}, GPa	G_{xz}, GPa
42	40	9	0.30	0.3	0.03	8.2	8.4	5.1

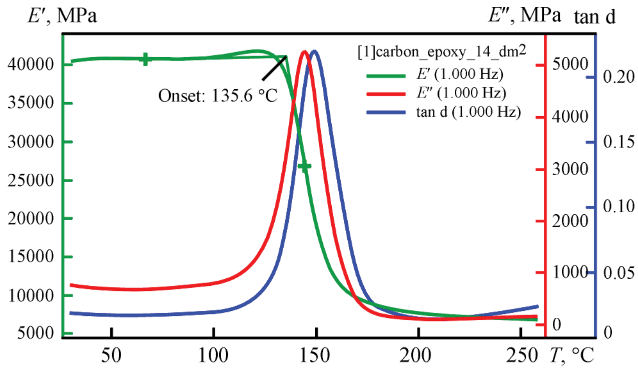

Figure 6. DMA results for sample CFRP

of orientation, some fibers may break, detachments from the lamellas may occur. Samples with this type of defects were removed Figure 5, *b*.

In the DMA analysis, the sample loaded with an oscillating sinusoidal force of 6 N at different preset frequencies provides information on the visco-elastic properties as a function of frequency, temperature and time. The parameters obtained through the tests provide information on vitrification, referred to T_g (glass transition), resulting from the cross-linking reaction. The determinations were made at a single frequency of 1 Hz, temperature range (25–260 °C).

A slight increase in the storage modulus, *E*′, from 40000 to 42000 MPa is observed. After this increase, a maximum of the Young's modulus is reached, followed by a decrease with the same slope of the storage modulus (elasticity modulus), *E*′, so that it remains constant around the value of 180 °C. The mechanisms for changing the elastic and viscoelastic mechanical properties were highlighted: storage modulus (*E*′), behavior over time to temperature changes of the composite, loss modulus (*E*″), loss factor (tan δ), temperature glass transition ($T_g = 135.6$ °C).

The DMA analysis shows the changes in the dynamic modulus of CFRP under the load with temperature as follows: the loss modulus reflects the adhesion of the material; the storage modulus, i.e. the elasticity modulus reflects the rigidity of the material; the ratio between the loss modulus and the storage modulus, i.e. the depreciation of the material $\tan\delta = \frac{E''}{E'}$. δ is the phase angle of stress and strain. The ratio of stress (σ) to strain (ε) under dynamic load is defined as the complex Young modulus of the material (E^*) which can be expressed as

$$E^* = \frac{\overline{\sigma}}{\overline{\varepsilon}} = \frac{\sigma_0}{\varepsilon_0} e^{i\delta} = E' + iE''. \qquad (2)$$

The main mechanical characteristics of the composite samples, E_x, E_y, E_z, were determined from the DMA graphs. Poisson's ratio ν_{xy} and ν_{yx} were determined by measuring US velocities. The shear modulus were calculated only by US procedure. The results are presented in Table 1.

The data obtained through complementary DMA methods and tensile tests completed with those of US allow a complete characterization of composites with polymer matrix reinforced with carbon fibers.

CONCLUSIONS

Characterization of carbon-epoxy composites can be made using ultrasound method complementary with destructive testing using Dynamic Mechanical Analysis. Using C-scan the regions with porosity due to manufacturing can be easily evaluated. For determination of elastic and shear modulus, Poisson's ratio of the composite materials with reinforcement from carbon fiber woven, the use of combined ultrasound methods is proposed, namely impulse-echo for compressional waves, send-receive method for transversal waves. Numerical analyzes and additional tests are required for different CFRP specimens to avoid discontinuities around the fasteners and to predict the evolution of crack propagation in the failure process.

REFERENCES

1. Tran, P., Wu, C., Saleh, M. et al. (2021) Composite structures subjected to underwater explosive loadings: A comprehensive review. *Composite Structures*, **263**, 113684.
2. Ozkan, D., Gok, MS., Karaoglanli, AC (2020) Carbon fiber reinforced polymer (CFRP) composite materials. Their characteristic properties, industrial application areas and their machinability. *Adv. Struct. Mater.*, **124**, 235–253.
3. Mathes, V. (2018) The composites industry: plenty of opportunities in a heterogeneous market. *Reinforced Plastics*, 62(**1**), 44–51.
4. Zorko, D., Tavčar, J., Bizjak, M. et al. (2021) High cycle fatigue behavior of autoclave-cured woven carbon fiber-reinforced polymer composite gears. *Polymer Testing*, **102**, 107339.
5. Othman, R., Ismail, NI, Pahmi, MAAH et al. (2018) Application of carbon fiber reinforced plastics in automotive industry: A review. *J. Mech. Manuf.*, **1**, 144–154.
6. Kaw, AK (2006) *Mechanics of composite materials*. 2nd Ed. Taylor and Francis, NY
7. Sang, L., Wang, Y., Wang, C. et al. (2019) Moisture diffusion and damage characteristics of carbon fabric reinforced polyamide 6 laminates under hydrothermal aging. Composites, Pt A. *Applied Sci. and Manufacturing*, **123**, 242–252.
8. Ortiz, JD, Khedmatgozar Dolati, SS, Malla, P. et al. (2023) FRP-reinforced/strengthened concrete: State-of-the-art review on durability and mechanical effects. *Materials*, 16(**5**), 1990.
9. Hübner, M., Lepke, D., Hardi, E. et al. (2019) Online monitoring of moisture diffusion in carbon fiber composites using miniaturized flexible material integrated sensors. *Sensors*, 19(**8**), 1748.
10. Lei, Y., Kang, Z., Zhang, J. et al. (2022) Effect of freeze-thaw cycling on the mechanical properties of continuous carbon fiber-reinforced polyamide 6 composites. *Polymer Testing*, **114**, 107704.
11. Romanowicz, M. (2012) A numerical approach for predicting the failure locus of fiber reinforced composites under combined transverse compression and axial tension. *Computational Materials Sci.*, 51(**1**), 7–12.
12. Cugnoni, J., Amacher, R., Kohler, S. et al. (2018) Towards aerospace grade thin-ply composites: Effect of ply thickness, fiber, matrix and interlayer toughening on strength and damage tolerance. *Composites Sci. and Technology*, **168**, 467–477.
13. Van de Werken, N., Tekinalp, H., Khanbolouki, P. et al. (2020) Additively manufactured carbon fiber-reinforced composites: State of the art and perspective. *Additive Manufacturing*, **31**, 100962.
14. Bhatt, AT, Gohil, PP, Chaudhary, V. (2018) Primary manufacturing processes for fiber reinforced composites: History, development & future research trends. In: *IOP Conf. Series. Materials Sci. and Eng.*, 330(**1**), 012107. IOP Publishing.
15. Bergant, Z., Savin, A., Grum, J. (2018) Effects of manufacturing technology on static, multi-frequency dynamic mechanical analysis and fracture energy of cross-ply and quasi-isotropic carbon/epoxy laminates. *Polymers and Polymer Composites*, 26(**5–6**), 358–370.
16. Technical Information. Sigrafil® continuous carbon fiber tow. Wiesbaden, SGL Group August 2022.

ORCID

A. Savin: 0000-0001-9863-3110
R. Steigmann: 0000-0003-1618-7650
M.D. Stanciu: 0000-0001-6414-9427
C.I. Moraras:0000-0001-6300-2255

CONFLICT OF INTEREST

The Authors declare no conflict of interest

CORRESPONDING AUTHOR

A. Savin
Nondestructive testing Department,
National Institute of R&D for Technical Physics, Iasi
15 D. Mangeron Blvd, Iasi 700050, Romania
E-mail: asavin@phys-iasi.ro

SUGGESTED CITATION

A. Savin, R. Steigmann, M.D. Stanciu, C.I. Moraras, G. Dobrescu (2024) Evaluation of the mechanical characteristics of CFRP composites and modeling of the delamination phenomenon. *The Paton Welding J.*, **12**, 30–34.
DOI: https://doi.org/10.37434/tpwj2024.12.05

JOURNAL HOME PAGE

https://patonpublishinghouse.com/eng/journals/tpwj

Received: 30.09.2024
Received in revised form: 12.11.2024
Accepted: 25.12.2024

DOI: https://doi.org/10.37434/tpwj2024.12.06

MODERN LEVELS FOR STRUCTURAL STRENGTH ASSESSMENT AND THE ALGORITHM FOR IMPLEMENTATION OF THE RISK ANALYSIS METHODOLOGY IN THE OPERATION OF WELDED METAL STRUCTURES

V.M. Torop

E.O. Paton Electric Welding Institute of the NASU
11 Kazymyr Malevych Str., 03150, Kyiv, Ukraine

ABSTRACT

Three levels of assessment of indices of structural strength, reliability and durability of welded metal structures are considered for the construction of the integrity management system (IMS) of welded metal structures. Level 1 uses the criteria of the limit state of welded metal structures based on safety margin factors and is implemented by us using a failure assessment diagram. Level 2 of probabilistic analysis of safety and reliability involves the formulation and evaluation of the values of probabilistic indices used to assess the structural strength, reliability and durability of welded metal structures in the presence of uncertainty and lack of completeness of input data. For level 3 of the risk analysis of the operation of welded metal structures, an algorithm for its realization is proposed and an implementation option in the form of an IMS is prescribed. The two-criteria failure assessment diagram is the basis of the implementation of all three levels.

KEYWORDS: risk, failure probability, consequences, two-criteria approach, failure assessment diagram, probabilistic safety analysis, risk matrix, integrity management system

INTRODUCTION

Modern high-efficient diagnostic tools, for instance, in-pipe diagnostic technologies, allow detecting and identifying thousands and even hundred thousand defects which are monitored in the main pipeline. After performance of in-pipe diagnostics the question arises about defect classification by the degree of their influence on the reliable and safe service. It is necessary to develop a rational and substantiated procedure for taking improvement measures (repair, revision of operating regulations), planning subsequent inspections (with determination of their terms and scope), and to prioritize areas for repairs. As a large numbers of defects which can be qualified as admissible ones, remain in service, it is probably inappropriate to talk about absolute reliability of such a structure. Under such circumstances there will always be a certain probability of the structure failure. In its turn, the failure probability should be regarded in combination with such an important characteristic as failure consequences, which require expert assessment. It is obvious that at the same failure probability the consequences of failure of the primary circuit pipeline in the power unit of a nuclear power plant (NPP) and of a petroleum processing plant will be different. Thus, different reliability levels should be used for different structural elements within the scope of consideration of one object. The product of failure probability by the index of failure consequences determines the risk which may be used as a universal measure of reliability and effectiveness of the object operation.

The probabilistic risk analysis is usually performed for potentially hazardous productions, chemical and technogenically-hazardous technological processes, to assess the reliability of nuclear power plants and their equipment, as well as in the aerospace industry. There are two causes, which somewhat restrain the introduction of risk analysis ideology: first, a range of factors which may cause a failure or accident, is so wide that it requires computerized object certification, qualified processing of the statistical material and operating with various laws of random value distribution to obtain valid evaluation data of the reliability, and, secondly, the majority of improvement measures aimed at increasing the object safety, which are based on outdated diagnostic methods can be effective even without knowing the real risk, associated with object operation. The latter approach has the right to exist, but it should be the methodological component of the general strategy of management of the reliability and efficiency (also, economic efficiency) of critical objects with rather convincing substantiation of their application.

Considerable activity, observed in the world in the field of ensuring the reliability of engineering systems and introducing the risk analysis ideology [1], is caused, on the one hand, by competition — optimization of the technological process towards lowering its cost, and on the other — by more stringent safety regulations, specified by state regulatory bodies (reg-

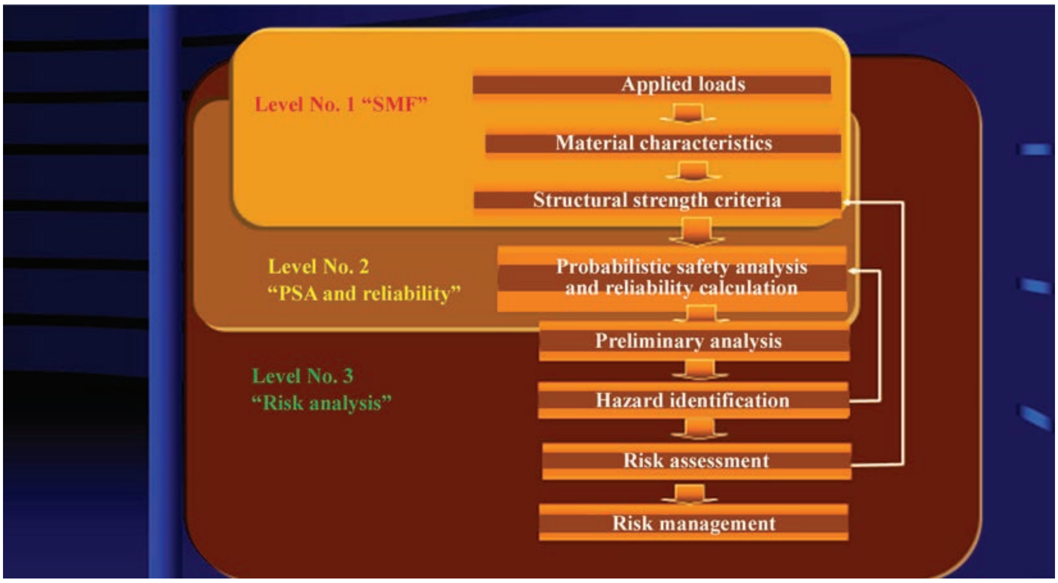

Figure 1. Modern levels of assessment of the indices of structural strength, reliability and durability of welded metal structures

ulator, for instance State Nuclear Regulatory Inspectorate of Ukraine, Derzhgirpromnaglyad, etc.).

It follows from the above-said that in the general case it is necessary to use a three-level approach for assessment of the indices of structural strength, reliability and durability of welded metal structures: pressure vessels, bridges, cylinders, tanks, pipelines, etc. (Figure 1).

LEVEL 1

uses the criteria of limit state of welded metal structures based on the safety margin factor (SMF), and it envisages formulation and use of the traditional deterministic indices of structural strength with determination of the limit state criteria at brittle, quasi-brittle and ductile fracture. On this level we recommend using a two-criteria approach, namely two-criteria failure assessment diagram (FAD) and its expansion [2]. Figure 2, *a* shows a modified FAD, the boundary curve of which is used as the fracture criterion of the main pipelines with defects [3]. A feature of FAD proposed by us and its temperature-load expansion (Figure 2, *b*) is explicit use of point T_b — critical brittleness temperature, which separates the brittle fracture zone from the quasibrittle fracture, and it is uniquely defined by coordinates of point B on FAD as follows B (1; $\xi = 0.7P_{YL}/P_{LL}$) (Figure 2, *a*). The abscissa of the point of quasibrittle transition B, which corresponds to T_t — toughness temperature, in Figure 2, *b* is determined from the condition of breaking load achieving limit load P_{LL}. The ordinate of point B based on the available experimental data corresponds to value $\mu = \dfrac{K_I}{K_{IC}} \approx 0.4 - 0.7$. As one can see from Figure 2, *a*, at $K_r = \dfrac{K_I}{K_{IC}} \prec \mu$ the ductile fracture criterion is realized: $S_r = 1$ or $P = P_{LL}$, where P is the generalized load applied to cracked structural element (CSE).

FAD, which in the general case is a certain boundary area II, separates area I of safe operation of CSE from fracture area III, using the admissible SMF *k*.

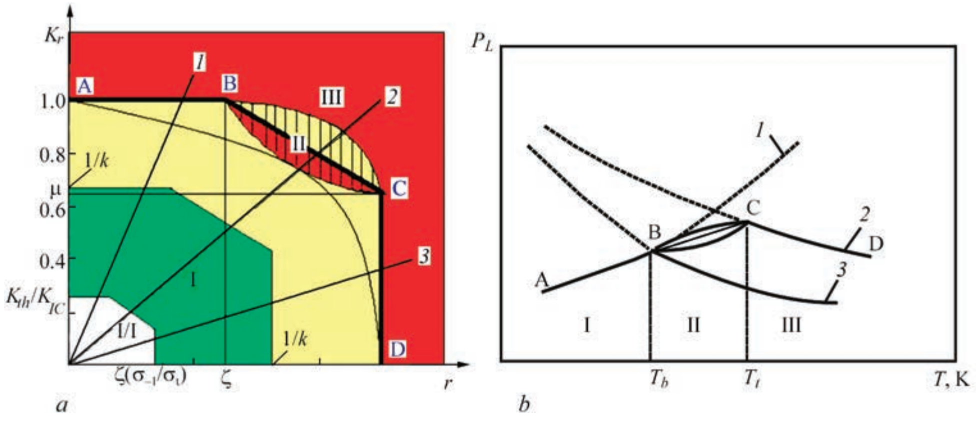

Figure 2. Two-criteria FAD (*a*): $S_r = \dfrac{P}{P_{LL}}$; $\xi = 0.7\dfrac{P_{YL}}{P_{LL}}$ and its loading-temperature expansion (*b*): *1* — P_L (K_{IC}); *2* — P_{LL} (σ_t); *3* — P_{YL} (σ_y), where σ_y is the yield strength and P_{YL} is the value of the load at the yield point of the entire net cross-section of the structure

In area II we will select the boundary line ABCD, in order to, first of all, simplify and perform the engineering assessment of the limit state of the cracked structural element, and secondly, be able to predict the brittle (ray 01 crosses area AB of FAD boundary line in Figure 2, *a*), quasibrittle or mixed (ray 02 crosses area BC of FAD boundary line in Figure 2, *a*) and ductile (ray 03 crosses area CD of FAD boundary line in Figure 2, *a*) fracture mode.

Green colour in Figure 2, *a* highlights admissible area I of CSE operation, which is determined allowing for admissible SMF *k*. Admissible SMF is a normative value by static strength criterion, which is specified by standards, norms, regulations, normative-technical documentation, etc. So, for NPP critical equipment [4] $k = 2.5$, and for main pipelines *k* is specified in keeping with SNiP 2.05.06–85 [5]:

$$k = \frac{0.9 k_1 k_R}{m}, \tag{1}$$

where m is the coefficient of operating conditions; k_1 is the coefficient of reliability, depending on material; k_R is the coefficient of reliability depending on purpose.

Yellow colour in Figure 2, *a* is used to highlight the zone of SMF validity II, requiring application of appropriate improvement measures as to the possibility of further safe operation of this CSE and it corresponds to subcritical controlled crack growth, the red colour shows the inadmissible zone III of CSE operation.

White color in Figure 2, *a* highlights the area IV, which is defined by coordinates $K_r = \frac{K_{th}}{K_{IC}}$ and $S_r = \zeta\left(\frac{\sigma_{-1}}{\sigma_t}\right)$,

where K_{th} is the fatigue crack propagation threshold of stress intensity factor (SIF) at cyclic loading; σ_{-1} is the limit of endurance, σ_t is the tensile strength. This area corresponds to the stage of defect initiation and propagation by the fatigue mechanism up to dimensions controlled by fracture mechanics laws.

LEVEL 2

of probabilistic analysis of safety (PSA) and reliability envisages formulation and assessment of probabilistic indices $\bar{x} = (x_1, x_2, \ldots, x_n)$ in the form of mathematical expectation $M(F,[R])$ and mean-root-square deviation $C(F, [R])$ of the generalized stochastic loading (applied load), scatter of measurements of structural element geometry and interpretation (schematization, classification, description of the geometry and location) of the defects detected by NDT means and scatter of experimental data on the mechanical properties and crack resistance characteristics of the materials and their welded joints.

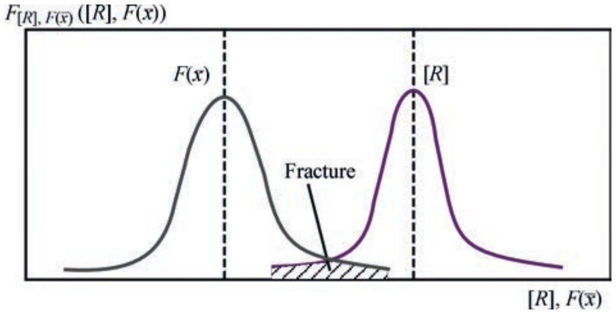

Figure 3. Fracture probability P_f which is determined by the area of intersection of the parameters of the structure stressed state $F(\bar{x})$ with the generalized stochastic fracture resistance $[R]$

In the general case, the function of the metal structure limit state $g(\bar{x})$ can be expressed in the following form:

$$g(\bar{x}) = [R] - F(\bar{x}), \tag{2}$$

where $[R]$ is the generalized stochastic fracture resistance that is characterized by admissible parameters, which are determined by the mechanical properties and crack resistance characteristics, allowing for the normative safety factors (SMF); $F(\bar{x})$ are the maximal, equivalent as to the selected strength criteria stochastic parameters of the structure stressed state, which were established by construction of a computational model and uncertainty analysis.

Then, the probability of metal structure destruction, as illustrated by Figure 3, is calculated by the following equation:

$$P_f = \int\limits_{g(x)\le 0} f_{[R],F(\bar{x})}\left([R], F(\bar{x})\right) dR\, dF(\bar{x}). \tag{3}$$

The following can be used as an integral function for indices of metal structure operation reliability RN^* [9, 10]:

- mathematical expectation and mean-root-square deviation of the appropriate indices of metal structure reliability $M(F,[R])$ and $C(F,[R])$, respectively;
- probability of the value of the respective reliability index *R* not being lower than the specified (normative) value R_{sp}. Let us denote this probabilistic index as $P(R \ge R_{\mathrm{sp}})$.

Depending on the research objectives and tasks solved at the main stages of the structural element life cycle (design, construction (repair) or operation [7]), the conditions of optimality or suitability, which are also called “fitness-for-purpose” criterion, can be imposed on each of the considered indices $M(F, [R])$, $C(F, [R])$, $P(R \ge R_{\mathrm{sp}})$ [11]. So, for $P(R \ge R_{\mathrm{sp}})$ index the fitness-for-service criterion will have the following form:

$$P(R \ge R_{\mathrm{sp}}) \ge P_{\mathrm{g}}, \tag{4}$$

where P_g is the guaranteed probability of the value of the respective reliability index R not being lower than the normative value R_{sp}.

We based the construction of the algorithm of simulation model of metal structure destruction on the indirect method of statistical probabilistic modeling (Monte-Carlo method [8]), which consists of the following steps:

1. In keeping with the known distribution laws $f_i(x_i)$ generate a sample of implementations N: $XN^* = (x_1^*, x_2^*, \dots, x_n^*)_i$, $i = \overline{1,N}$ of random values $x_1, x_2, \dots, x_n$, which belong to the specified range of values (of parameters, characteristics).

2. Substitute the formulated implementations $(x_1^*, x_2^*, \dots, x_n^*)_i$, $i = \overline{1,N}$, into (2) and obtain the respective sample of implementations of reliability indices F, $[R]$: $RN^* = (F_i, [R]_i, i = \overline{1,N})$.

3. Based on the sample of implementations of reliability indices $RN^* = (F_i, [R]_i, i = \overline{1,N})$ obtain a sample of estimated values of the respective probabilistic reliability indices $(M^*(F, [R]), C^*(F, [R]), P^*(R \geq R_{sp}), \dots)_i$, $i = \overline{1,N}$.

4. Proceeding from the sample of estimated values of the respective probabilistic reliability indices $M^*(F, [R])$, $C^*(F, [R])$, $P^*(R \geq R_{sp})$, $i = \overline{1,N}$ make conclusions as to the structural strength and truth of the values of these indices.

Implementation of the first step is based on standard methods of modeling the random values and vectors, using the algorithmic sensors of random values [8].

Special attention in the second step should be paid to application of a correct deterministic fracture model (criterion). We use a two-criteria approach [2] and two-criteria failure assessment diagrams developed on its base.

Implementation of the third step is based on obtaining point estimates of the probabilistic reliability indices $M^*(F, [R])$, $C^*(F, [R])$, $P^*(R \geq R_{sp})$, $i = \overline{1,N}$ using a sample of implementations of deterministic indices $RN^* = (F_i[R]_i, i = \overline{1,N})$. Point values of estimates of the first two indices (mathematical expectation and mean-root-square deviation) are determined as follows:

$$M^*(F,[R]) = \sum_{i=1}^{j} \frac{(F,[R]}{j},\ j = \overline{1,N}; \tag{5}$$

$$C(F,[R]) = \sqrt{D(F,[R]_j},\ j = \overline{1,N}, \tag{6}$$

where $D(F, [R]_j)$ is the estimation of the dispersion of sample values:

$$D(F,[R])_j = \sum_{i=1}^{j} \frac{(F,[R]-M(F,[R]))}{j},\ j = \overline{1,N}. \tag{7}$$

International standard ISO 16708:2006 can be an example of implementation of level 2 for the main oil and gas pipelines [6]. In limit states, when the structure experiences additional loads or loss of quality and violates the safety standards in keeping with the deterministic approach, the deterministic approach proper can no longer be applied to determine if the structure still is sufficiently safe. Limit states in this context are, for instance, material aging, considerable corrosion and additional loads, not allowed for in the initial design.

In this case, a probabilistic approach can be used, calculating the structure failure rate. It was introduced approximately 20 years ago during structure design. Compared to the deterministic approach, failure rate calculation is a complex process. The problem is establishing the generally accepted limitations for the failure rate.

The International Standardization Organization (ISO) has worked on this issue for many years and ISO 16708 standard "Petroleum and natural gas industries — Pipeline transportation systems — Reliability-based limit state methods" [6] was often changed in the draft status for a long period of time. In 2006 it was accepted as DIN EN ISO 16708, as the National Standard of Germany.

The scope of application of DIN EN ISO 16708 standard allows using the deterministic and probabilistic approaches in parallel. The standard has a high level of recognition among the authorities, experts and specialists-engineers.

In modern practice DBN V.1.2-14:2018 [11] is used for ensuring the reliability and structural safety of buildings and constructions, which is applied when searching for, designing, building and liquidation of buildings and structures, irrespective of their purpose. Thus, level 2 of probabilistic safety analysis (PSA) and reliability is applied for complicated issues of uncertainty when compiling the "Objects", "Defects", "Loads", and "Properties" data bases, which are required for construction of a computational model, identifying the potentially critical cross-sections of a welded metal structure and assessment of structural strength, using a two-criteria approach based on Monte-Carlo method [8–10].

LEVEL 3

At this level it is necessary to formulate and assess the above-mentioned probabilistic indices of structural strength, reliability and durability with guaranteed or confidence level, which allow for failure consequences [10, 12].

Selection of a particular level of assessment of the indices of structural strength, reliability, durability of structural elements will depend on such main factors as: importance of the assessed structure; stage of its life cycle under consideration; input data used to obtain the respective estimates of the indices and the level of confidence in them.

In order to introduce the methodology of risk assessment at operation of welded metal structures, it is first of all necessary to develop a risk assessment program. The operator should take into account all the features of his metal structure, operating in a certain system (for instance, a power unit of a nuclear power plant should be regarded as such a system, etc.) and should decide, which of the approaches is the most suitable. The main objective of risk assessment consists in identifying the greatest risks in the system so that the operator could decide how, where and when to take the repair and improvement measures, so that it would increase the integrity of the metal structure of the mentioned system in the most effective manner. The operator should decide which information can be useful for assessment, and how this information should be used, so that the accuracy and effectiveness of the estimates were maximal. A simplified scheme of risk analysis performance is shown in Figure 4 [12, 13].

It is obvious that risk analysis includes three main components: risk analysis, which considers and analyzes the possibility of accidents (destruction) with their consequences; risk assessment, which compares the obtained risk with the available criteria of its admissibility; risk management which envisages and defines the measures for risk reduction.

A substantiated methodology of risk assessment should be:

Structured. Risk assessment procedures usually use the input data of the systems of technical condition monitoring (sensors, controllers, etc.) or are formulated by experts in the field of assessment of strength, corrosion protection, welding, technological production processes, etc. All the methods of risk assessment, however, determine and use the logical schemes in order to determine how the data being considered influence the risk in the terms of probability of an accident or its potential consequences.

Supported by sufficient resources. Sufficient number of staff and adequate time should be allocated to successfully fulfill all the stages and detail the risk analysis.

Based on real experience. The frequency and severity of the consequences of previous events (in this or a similar welded metal structure) should be considered, as well as understanding and taking into account all the improvement measures, implemented to prevent such situations. Risk assessment methods should take into account the specific history of functioning of this welded metal structure.

Predictive. By its nature the procedure should be exploratory, i.e. it should identify the earlier not taken into account threats to the integrity of the welded metal structure. Accident scenarios which had never occurred before in this metal structure, should be considered.

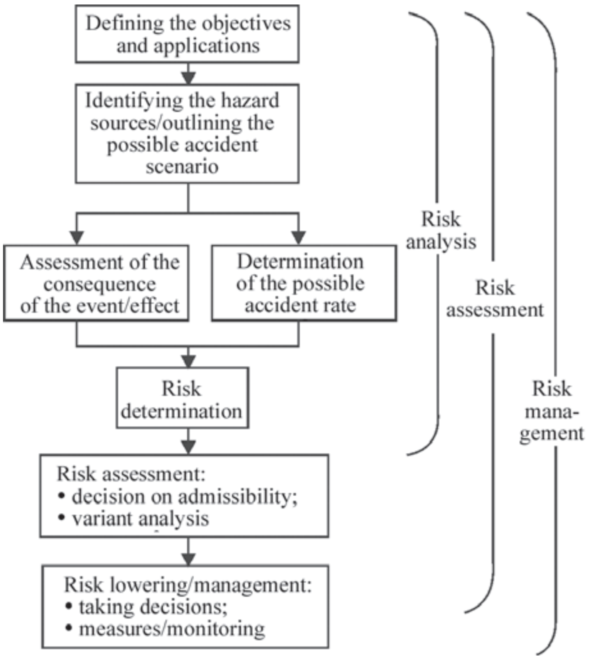

Figure 4. Simplified scheme of risk analysis

Use adequate data. Some risk analysis decisions are just subjective expert statements. Therefore, adequate input data of the systems of monitoring the technical state of the metal structure are just mandatory to take objective decisions and estimates.

Capable of supporting feedback. Risk analysis is an interactive process. Real events and data on the condition of the welded metal structure should be used to confirm or correct the made assumptions.

FIRST STEPS DURING RISK ASSESSMENT

Generally accepted start of the assessment process consists in formation of a representative group of company experts for identification of the events or conditions (risk analysis) which may lead to failure of this metal structure, for assessment of the accident consequences, as well as for determination of the measures, which reduce the risk for this metal structure. This group should include the representatives from the departments of management, operation, units of control of metal, corrosion, safety, engineers from the construction site, representatives of the regulator (supervisory) bodies, etc. The purpose of this group consists in outlining and incorporating the experience of different expert groups into the risk assessment method so that these methods could use the experience and information, not yet taken into account in the data bases of integrity management system (IMS) [1, 7, 13, 14].

The following generally accepted methods can be used to conduct systematic and complete investigation:

- free-form brainstorming technique for potential risk analysis;
- performing segment-by-segment analysis (area-by-area) of the metal structure using geoinformation systems;

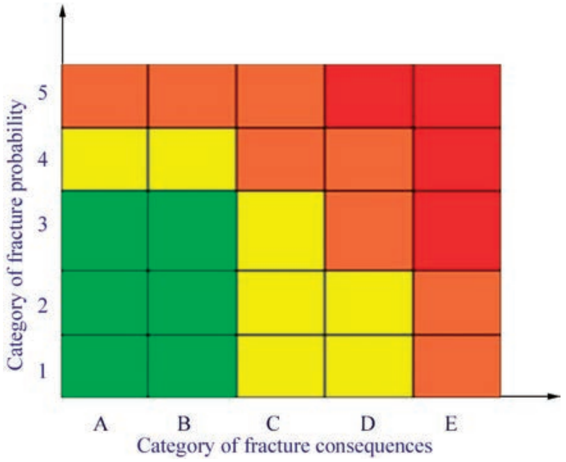

Figure 5. Risk matrix [1, 13]

- use of a list of structured questions, pertaining to the complete list of possible hazards and problems of metal structure integrity;
- application of simple risk matrices, shown in Figure 5 for illustration, for qualitative analysis of the probability and consequences of possible events [1, 13].

MAIN COMPONENTS OF RISK ASSESSMENT METHODOLOGY

Risk assessment is a process of combining the estimates of accident frequency and consequences into a unified risk value. The risk value can be quantitative, qualitative or a combination of the two, depending on the assessment procedure, or the objective set by the operator during IMS development [1, 7, 13, 14]. The sensitivity and accuracy of risk assessment methods is a function of the number of variables used, and the ability to determine the change in the risk along the coordinates of the welded metal structure.

Some methods require the user to assess the risk in individual areas of the metal structure, using similar characteristics, while other take into account the local effects of the change of functioning conditions. For instance, as regards the main pipelines, it can be the values of cathode protection indices, presence of defects, number of diagnostic anomalies, fracture modes, etc. In many methods the event probability is assessed using variable values and indices, pertaining to:

- external corrosion;
- internal corrosion;
- third party damage;
- soil movement (shifts, subsidences, ground undermining in mining areas, etc.);
- design conditions and material characteristics;
- metal structure functioning in the system.

The consequences are assessed using variables belonging to the following categories:

- environmental impact;
- influence on population;
- economic consequences.

The more such variables are used, the more quantitative is the analysis. The quantitative analysis accuracy is enhanced with further specifying of the variables (effect of interaction with the supports, foundation, soil type, age (aging) of the metal structures, protective coating quality, etc.).

RISK VALIDATION AND IDENTIFICATION

Irrespective of the process of risk assessment performance, the operator must analyze the information so as to guarantee that the accepted technology yields the results, which on the whole correspond to analysis purpose. This can be achieved involving either a specialist on risk analysis having experience of analysis of similar systems, or a multifaceted team of specialists on functioning of similar diagnostics objects. If the obtained results do not correspond to the operator's perception of the real risk, he should study the causes for such differences, and if required, revise the methods, input assumptions or data.

After validation of the risk assessment methods, the operator has the necessary information for ranging the risks. The segment with a greater degree of risk should be given greater priority at identification of areas where the improvement measures should be applied (priority of diagnostics, repair, etc.). To reduce the overall risk, the operator first has to analyze the causes for appearance of a high risk in this segment. This can be due either to a high probability of the event (destruction) or significant consequences. This information is important to take decisions as to the scope and list of improvement measures.

RISK MANAGEMENT AND IMPROVEMENT MEASURES

Risk assessment methods are an important tool to support the operator when taking economically and technically sound solutions on reducing the risks for their systems. As soon as the potential risk has been indentified and the means for its reduction have been determined, the methods of risk assessment can be applied again to determine the risk reduction value and obtaining material benefit. These methods can be constantly used at assessment of the rationality of the proposed improvement measures. In combination with analysis of the cost for introduction of these measures, risk analysis allows the company to select the most effective measures which can be applied in this period.

Figure 6 shows the algorithm for introduction of the methodology of risk assessment in welded metal structures, which was implemented by us using program-procedural complex (PPC) "Probabilistic risk analysis" of "Strength" expert system [7, 12].

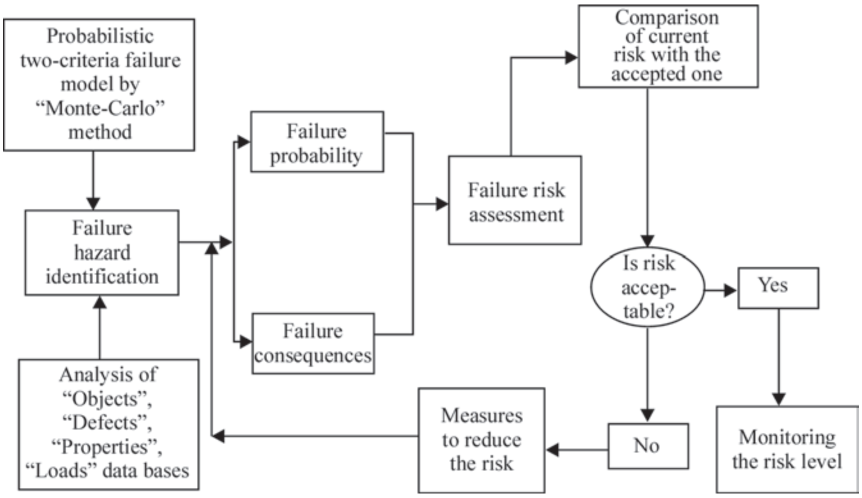

Figure 6. Algorithm for introduction of the methodology of welded metal structure risk assessment

CONCLUSIONS

1. Three levels of assessment of the indices of structural strength, reliability and durability of welded metal structures were considered for construction of an integrity management system, which uses a two-criteria fracture assessment diagram.

2. An algorithm was proposed for introduction of risk assessment methodology based on the system of management of welded metal structure integrity.

REFERENCES

1. Torop, V.M. (2024) Practice of implementing the methodology of risk analysis of the operation of welded metal structures in Ukraine. *Tekh. Diahnost. ta Neruiniv. Kontrol*, **2**, 41–46 [in Ukrainian]. DOI: https://doi. org/10.37434/tdnk2024.02.06
2. Krasovsky, A.Ya., Krasyko, V.N., Torop, V.M., Orynyak, I.V. (1987) Estimation of the ultimate bearing capacity of a body with a crack and determination of brittle-viscous transition temperatures in metals. *Problemy Prochnosti*, **12**, 8–13 [in Russian].
3. DSTU-N B V.2.3-21:2008: *Main pipelines. Directive. Determination of the residual strength of main pipelines with defects* [in Ukrainian].
4. (1989) PNAE G-7-002–86: *Norms of strength analysis of equipment and pipelines of nuclear power plants* [in Russian].
5. (1985) SNiP 2.05.06–85: *Main pipelines. Building regulations* [in Russian].
6. ISO 16708:2006: *Petroleum and natural gas industries — Pipeline transportation systems — Reliability-based limit state methods.*
7. Torop, V.M. (1994) Decision support systems for strength accompaniment of the safe operation of NPP equipment. In: *Proc. of Third Int. Conf. on Material Science Problems in NPP Equipment Production and Operation, St-Petersburg, 17–22 June 1994*, **3**, 740–750.
8. (1951) *Monte Carlo Method*. Applied Mathematics Series, Vol. 12, National Bureau of Standards, Washington D.C.
9. Torop, V.M. (2005) Probability hazard analysis of the operation of pipeline systems, tanks, and pressure vessels. Pt 1. Algorithm of construction of the probability model. *Strength of Mater.*, **37**, 174–179. DOI: https://doi.org/10.1007/s11223-005-0030-1
10. Torop, V.M. (2005) Probability hazard analysis of the operation of pipeline systems, tanks, and pressure vessels. Pt 2. Method for the evaluation of the functional fitness of a structural element according to the restricted statistical data. *Strength of Mater.*, **37**, 298–303. DOI: https://doi.org/10.1007/s11223-005-0042-x
11. DBN V.1.2-14:2018: *The fundamental principles of ensuring reliability and constructive safety of life and disputes.*
12. Torop, V.M., Torop, O.V. (2004) Implementation of risk analysis in the system of ensuring the integrity of main pipelines. In: *Proc. of 14th Int. Business Meeting on Diagnostics 2004, Moscow*, 81–85.
13. (2016) *Risk based inspection technology codes API 581*. Ninth Edition. API, Washington, D.C, API Publ. Services.
14. DSTU ISO 31000:2014: *Risk management. Principles and guidelines*. New version from 2018. https://online. budstandart.com/ua/catalog/doc-page.html?id_ doc=80322

ORCID

V.M. Torop: 0000-0002-8807-9811

CORRESPONDING AUTHOR

V.M. Torop
E.O. Paton Electric Welding Institute of the NASU
11 Kazymyr Malevych Str., 03150, Kyiv, Ukraine.
E-mail: v.torop@gmail.com

SUGGESTED CITATION

V.M. Torop (2024) Modern levels for structural strength assessment and the algorithm for implementation of the risk analysis methodology in the operation of welded metal structures. *The Paton Welding J.*, **12**, 35–41.
DOI: https://doi.org/10.37434/tpwj2024.12.06

JOURNAL HOME PAGE

https://patonpublishinghouse.com/eng/journals/tpwj

Received: 02.05.2024
Received in revised form: 27.06.2024
Accepted: 20.11.2024

DOI: https://doi.org/10.37434/tpwj2024.12.07

STUDIES OF EDDY CURRENT PROBES FOR INSPECTION OF ALUMINIUM ALLOY STRUCTURE WELDS USING SMARTPHONE-BASED FLAW DETECTOR

G. Mook[1], **V. Uchanin**[2], **Ju. Lysenko**[2]

[1]Otto-von-Guericke-Universität Magdeburg, Universitätsplatz 2, 39106 Magdeburg, Germany
[2]G.V. Karpenko Physico-Mechanical Institute of the NASU
5 Naukova Str., 79060, Lviv, Ukraine
[3]National Technical University of Ukraine “Igor Sikorsky Kyiv Polytechnic Institute”
37 Prosp. Beresteiskyi, 03056, Kyiv, Ukraine

ABSTRACT

Features of the design and capabilities of the smartphone-based eddy current flaw detector with the EddySmart software application are presented, which in the future can provide a remote inspection with the wireless transmission of inspection results via mobile communication channels for the further analysis and storage. The perspectives of application of eddy current probes (ECP) of double differential type for inspection of structure welds made of aluminium alloys are considered. The characteristics and results of studies of low-frequency double differential MDF 0801 and MDF 1001M type eddy current probes with operational diameters of 8 and 10 mm, respectively, designed for detection of defects in aluminium alloy welds are presented. It is shown that to detect extended and local defects in aluminium alloy structure welds at a greater depth, the preference should be given to the improved eddy current probe of MDF 1001M type with an operational diameter of 10 mm, which provides a higher level of signals and better noise resistance.

KEYWORDS: non-destructive inspection, eddy current probe, smartphone-based flaw detector, weld, aluminium alloy

INTRODUCTION

Today, pocket smartphones have become an integral part of our live. Smartphones differ from conventional mobile phones in that they have a full-fledged operating system open to software development, unlike mobile phones that have a closed operating system. In addition, smartphones have the features of a personal computer with permanent data storage, random-access memory and relatively powerful central and graphics processors. A modern smartphone can have a variety of sensors (including accelerometer, gyroscope, magnetometer, light sensor, barometer, thermometer, Hall sensor and fingerprint scanner), which improves its functional versatility and the ability of using it not only for communication or entertainment. The use of a smartphone as a measuring device is somewhat unconventional. There are examples of creating a fully functioning microscope based on a smartphone using a rubber attachment for a camera with a 1 mm diameter lens. The resolution of such a microscope was about 1.5 μm. Another interesting example is the implementation of a smartphone-based spectrometer for analysing light waves.

There are also examples of the implementation of smartphone-based full-fledged systems of non-destructive inspection (NDI), technical diagnostics and monitoring [1–9]. In [1–3] an ultrasonic flaw detector, created at the Igor Sikorsky Kyiv Polytechnic Institute is described, which consists of an electronic unit with an ultrasonic sensor and a smartphone. The exchange of information between the sensor unit and the smartphone is performed via wireless networks using Bluetooth technology. The flaw detector operation algorithm is implemented using special software that runs on the Android operating system. A similar approach is implemented in the development of the French Company LECOEUR ELECTRONIQUE [4]. Another example concerns a system for vibration monitoring of the technical condition of structures [5]. The authors have developed a system application for Android that can easily turn several smartphones into a wireless vibration monitoring system for structures. A server-client architecture was used, where one smartphone is designated as a remote control system for all other smartphones, allowing the server smartphone to quickly and easily connect multiple smartphones with sensors to create a wireless network. A method for synchronising different smartphones to simultaneously measure the vibration of structures was also proposed.

A successful implementation of a smartphone-based NDI device is an eddy current flaw detector (ECFD) with the EddySmart application, which has been successfully used primarily for student education [10, 11]. But already today, the ambitions of this development go beyond the tasks defined at the initial stage of its creation. In [12], it is considered as a sprout for the creation of promising technologies within the framework of the NDI 4.0 concept. The authors, in particular, draw attention to the possibility of wireless transmission of inspection results via mobile communication channels for the further analysis and storage. The smartphone-based ECFD with the EddySmart application was effectively used to demonstrate the capabilities of new eddy current technologies for detection of inner defects in aircraft and space structures, which eliminated the need in using bulky traditional ECFDs.

Low-frequency double differential eddy current probes (ECPs) have been widely used to detect surface and inner defects in structures made of nonmagnetic materials [13]. Their peculiarity is high sensitivity to local defects compared to traditional ECPs. Therefore, double differential ECPs are promising for creating technologies for detecting weld defects, especially when inspection becomes more complicated due to noise signals created by the inhomogeneity of the specific electrical conductivity and changes in geometry (reinforcement bead, edge warping, etc.) in the weld zone. Here, it is necessary to use signal interpretation methods applying the ECFD's integrated display plane [14]. Double differential ECPs have already found their use, including for the detection of lacks of fusion and pores in welds [15, 16]. In the extended welds of the shells in space structures of aluminium 1201 alloy made by electron beam welding, surface defects of lack of fusion (adhesion) type were successfully detected. Defects of this type can be formed when the electron beam deviates from the butt of parts to be welded. Due to the partial diffusion bonding (adhesion) of welded edges, this type of defect is extremely difficult to detect using conventional NDI methods. Another example concerns the problem of detecting welded surface and inner defects of various types in the welds of space structures made of AMg-5 and AMg-6 type alloys, produced by arc welding. Inspection technologies based on the use of low-frequency ECPs ensured the detection of not only surface defects, but also subsurface defects such as pores, lacks of fusion, inclusions and oxide films, despite the lift-off created by the inhomogeneity of the weld geometry. The results of the further studies have shown the possibility of improving and optimizing the ECP for welds inspection in order to reduce the sizes of the ECP with a corresponding improvement in the resolution, at the same time increasing the depth of inspection, which will allow detecting extended and local defects at a greater depth.

This work presents the features of the design and capabilities of a smartphone-based ECFD and studies carried out by improved low-frequency double-differentiation ECPs for detecting inner defects in welds of aluminium alloy.

1. DESIGN, MAIN FUNCTIONS AND CAPABILITIES OF A SMARTPHONE-BASED EDDY CURRENT FLAW DETECTOR

Let us consider the main functions that need to be implemented to create a smartphone-based ECFD using a generalized block diagram of a typical ECFD (Figure 1). The creation of a primary sinusoidal electromagnetic field of the required operating frequency is performed by a controlled generator *1* and a power amplifier *2*, which provide the required current level in the ECP generator winding *3*, which interacts with the test object (TO) *4*, inducing eddy currents in it. The resulting electromagnetic field of the TO *4* generates a signal in the measuring ECP winding *3*, which carries components caused by the unbalance of the ECP (signal of the measuring winding during its placing on a defect-free part of the TO) and the influence of a defect in the TO during scanning of its surface. The appearance of a defect during scanning changes the distribution of eddy currents, which affects the ECP input signal, performing modulation of the output ECP signal at the operating frequency. The ECP output signal is fed to the input cascade *5*, which provides its improvement by amplification to the required level and HF-filtering. Then the signal is fed to phase-sensitive detectors *6* and *7*, which perform the

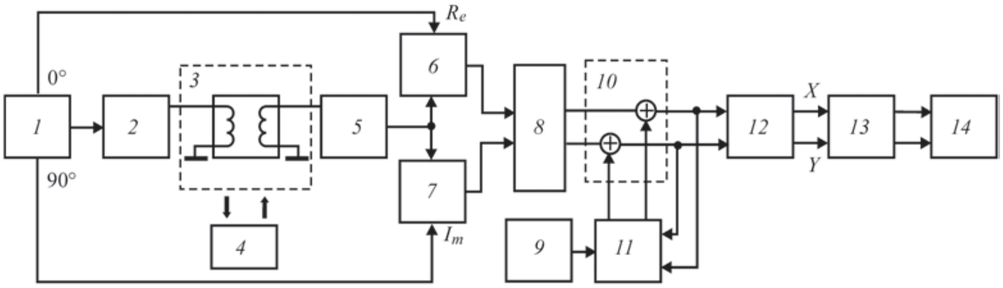

Figure 1. Block diagram of a typical ECFD composition: *1* — generator; *2* — power amplifier; *3* — ECP; *4* — TO; *5* — input cascade; *6* and *7* — phase-sensitive rectifiers; *8* — filters; *9* — adder; *10* — circuit for unbalance compensation signal formation with a start button *11*; *12* — phase shifter; *13* — amplifier of *X* and *Y* components; *14* — display

ECP signal demodulation operation, generating DC signals at the output corresponding to real and imaginary components of the ECP output signal. Further, the output signals of phase-sensitive detectors *6* and *7* through filters *8* are fed to adders *9* for compensation of the ECP unbalance, the other input of which receives the signals necessary for compensation of unbalance from the unbalance compensation signal generation circuit *10* with a start button *11*. To reduce the noise influence, low-pass (LP) or high-pass (HP) filters with adjustable cutoff frequencies are used. When both filters are used simultaneously, a band-pass filter mode is provided. To compensate for the ECP unbalance signal, the ECP is placed on a defect-free part of the sample, and then the operator starts the balancing process by pressing the button *11*. Thus, real and imaginary components of the signal eliminate the components, corresponding to the ECP position on a defect-free part of the sample (TO). This operation allows selecting components that correspond only to the defect influence. Then, the obtained components are fed to the phase shifter *12*, which rotates the complex plane of the ECFD by an angle of 0–360°, which allows manipulating the signal hodographs in the complex plane of the ECFD during scanning of the TO surface, directing the useful signal, for example, in the vertical direction of the display. From the output of the phase shifter *12* through the amplifier *13*, the horizontal *X* and vertical *Y* components are fed to the ECFD display, which displays changes in the ECP signal in the complex plane (*Y/X* mode) or changes in real or imaginary components of the ECP signal in the time scan mode (*Y/t* or *X/t* mode).

A modern smartphone contains all the components required for building an eddy current device with the above functions (Figure 1). Its audio interface allows simultaneous transmission and reception of signals with a frequency of up to 20 kHz, which is sufficient for operation in the low-frequency range of eddy current inspection. Thus, the main idea of the development is to use the audio system of a smartphone to build an eddy current device, unlike ultrasonic smartphone-based systems, when the units necessary for creating a flaw detector (in particular, generators and signal processing circuit elements) are made in a separate unit [10, 11]. In this case, ECPs are connected directly to the smartphone's audio jack, which provides a signal strong enough for its operation, where additional power amplifier is not required. The quality of the 4-pin audio jack plays an important role, so it is necessary to choose a version with gold-plated contacts. For such a connection, the ECP cable is equipped with an electronic circuit that simulates a headset. The flaw detector designed by the Otto von Guericke University Magdeburg requires the use of an Android OS smartphone, in particular, of the Samsung Galaxy series.

The generalized structure of the EddySmart software application is shown in Figure 2, which also shows the correspondence of the displayed control results and adjustment operations to different areas of the smartphone touch screen. Hence, it is seen, that most of the functions of the ECFDs shown in Figure 1, are implemented by the software.

The background process simultaneously processes the ECP signal buffers (output excitation and input measurement). It fills the two-channel buffer with a sinusoidal excitation signal and empties the single-channel input signal buffer, which contains a mixture of excitation and measurement signals. The measurement signal is separated in the received signal and demodulated with respect to the ECP excitation signal. This process is implemented without participation of the user (flaw detector operator).

The user interface provides indication of inspection results, amplification to intensify the obtained

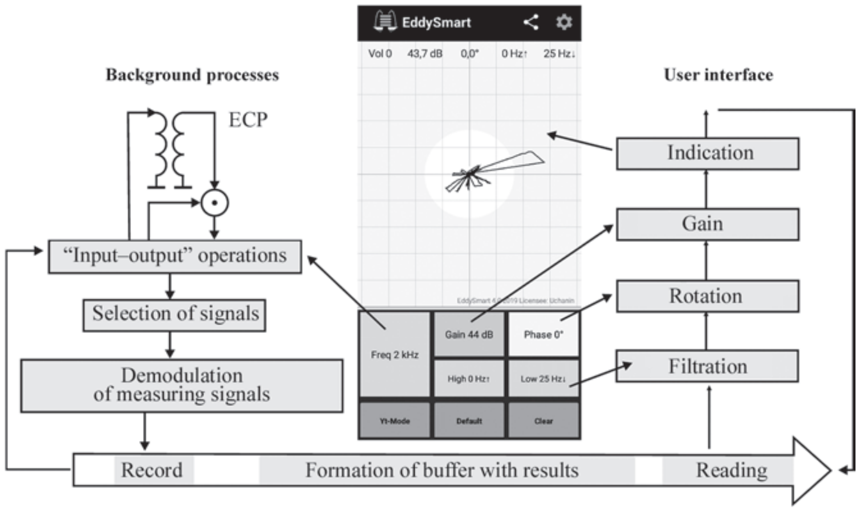

Figure 2. Generalized structure and appearance of the EddySmart software application display

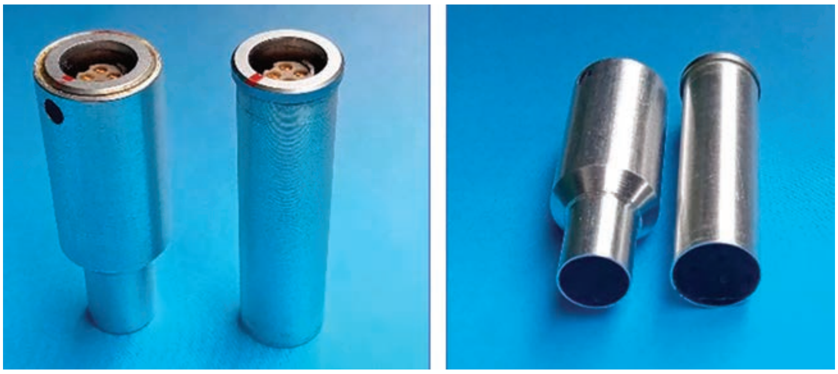

Figure 3. Studied double differential MDF 0801 and MDF 1001M type ECPs

hodographs and their rotation in the complex plane, as well as filtering. The selection of these parameters is controlled by the flaw detector operator using the touch screen of a smartphone.

The upper line of the smartphone display shows the audio signal level, which is adjusted by the corresponding smartphone button, as well as the gain level, complex frequency rotation angle and cutoff frequencies of the LP- and HP-filters. Most of the smartphone display is used to indicate the inspection results, which can reflect hodorgaphs of the signals from defects in the complex plane or changes in the signal from a defect in the time scan mode. This part of the display is also used to adjust the gain and rotation of the complex plane by means of manipulations easy to understand for the operator [10, 11]. The lower third of the touch screen display is used to select modes and inspection parameters using the corresponding buttons, including selection of the operating frequency (Freq — upper left), switching to the time scan mode (Yt-mode — lower left), switching on the gain (Gain dB — upper in the middle line), selection of the high-pass filter cut-off frequency (High Hz — middle), default operation (Default — lower in the middle line), phase selection (Phase — upper in the right line), selection of low-pass filter cut-off low frequency (Low Hz — middle in the right line) and selection of screen record or clear mode (Record or Clear — lower in the right line).

The presented capabilities of a smartphone-based ECFD allow it to be used to select the optimal operating frequency and study the sensitivity of ECP to various types of subsurface defects.

2. STUDY OF LOW-FREQUENCY DOUBLE DIFFERENTIAL ECPS FOR DETECTION OF WELD DEFECTS IN ALUMINIUM ALLOY STRUCTURES

2.1. STUDIED ECPs, SAMPLES AND RESEARCH TECHNIQUES

Experimental prototypes of two low-frequency double differential MDF 0801 and MDF 1001M type ECPs with the working surface diameters of 8 and 10 mm, respectively (Figure 3), designed to detect defects in welds of aluminium alloys were studied. The peculiarity of the MDF 0801 type ECP is the higher resolution required to detect not only extended defects such as cracks, but also local defects of a sufficiently small diameter such as pores or inclusions. The advantage of the MDF 1001M type ECP is an increased depth of inspection due to an increased winding diameter. The parameters of the experimental ECPs are given in Table 1, where: D_{ECP} is the ECP diameter; D_f is the ferrite core diameter; w_{ew} and w_{mw} are the quantity of turns of excitation and measuring windings, respectively; L_{ew} and L_{mw} are the inductances of excitation and measuring windings, respectively.

To study the influence of the flaw depth, regardless of its size, assembled standard specimens (SS) were used, each of which allows simulating a defect of the same depth for two discrete values of the flaw depth (Figure 4). Two SS parts are assembled in such a way that after their combination, a rectangular plate of a thickness T is formed with the buttt of the two parts perpendicular to the SS surface, which reproduces a subsurface defect of a depth a. From the different SS surface, the flaw depths of a defect h_{f1} and h_{f2} are different according to the ratio $h_{f1} + h_{f2} + a = T$. Two SSs made of aluminium D16 T alloy were used for

Table 1. Parameters of studied ECPs

ECP type	D_{ECP}, mm	D_f, mm	w_{ew}	w_{mw}	L_{ew}, μH	L_{mw}, μH
MDF 0801	8.0	1.85	215	416	940	3.7
MDF 1001M	10.0	2.9	125	420	310	1.4

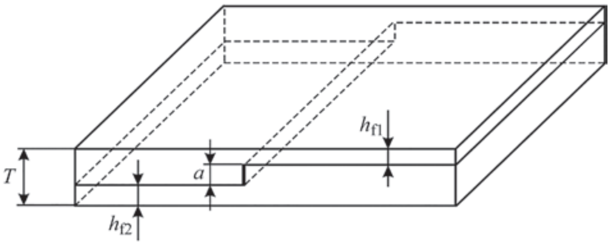

Figure 4. Assembled SS for reproduction of two discrete values of defect flaw depth

the studies, the parameters of which are presented in Table 2.

Thus, the presented SSs allow obtaining four discrete values (1.0, 2.0, 3.0 and 4.0 mm) of the flaw depth of location for a subsurface crack-type defect of the same size and studying the influence of the flaw depth of location on the ECP signal regardless of defect sizes.

2.2. COMPARATIVE ANALYSIS OF ECP SIGNALS FROM SUBSURFACE DEFECTS

Figure 5 shows the MDF 0801 type ECP signals from SS defects with different flaw depths in the complex plane at an operating frequency of 2 kHz, which turned out to be optimal for these defects.

Figure 6 shows the MDF 1001M type ECP signals from SS defects with different flaw depths in the complex plane at an operating frequency of 2 kHz.

The analysis of the ECP signals in Figures 5 and 6 shows that the MDF 0801 and MDF 1001M type ECPs allow detecting all SS defects with a flaw depth of up to 4 mm, although for both ECPs the amplitude of the signals from defects significantly decreases with an increase in their flaw depth. Simultaneously with an increase in the flaw depth, the direction of the hodograph from a defect (signal phase) in the complex plane expands clockwise, which can be used to determine the flaw depth in the future. At the same time, the MDF 0801 type ECP requires more signal amplification. In particular, to detect a defect with a depth of 4 mm by the MDF 0801 type ECP, 70 dB amplification is required, and only 56 dB is required when using the MDF 1001M type ECP. This indicates that the MDF 1001M type ECP has greater capabilities when it is required to detect subsurface defects, since the level of noise grows with an increase in amplification, as is seen from the comparison of signals in Figures 3 and 4. However, it should be kept in mind that the MDF 0801 type ECP may have a potential advantage in terms of resolution and the ability to detect local defects of smaller size due to the significantly smaller diameter of the used ferrite cores (see Table 1).

To study the signals from subsurface local defects, a 6 mm thick plate of D16 T aluminium alloy with two

Table 2. SS parameters for studying the influence of flaw depth of location

SS type	SS thickness T, mm	Flaw depth α, mm	Flaw depth of location, mm	
			h_{f1}	h_{f2}
SOP 7.2.2-3	7.0	2.0	2.0	3.0
SOP 7.2.1-4			1.0	4.0

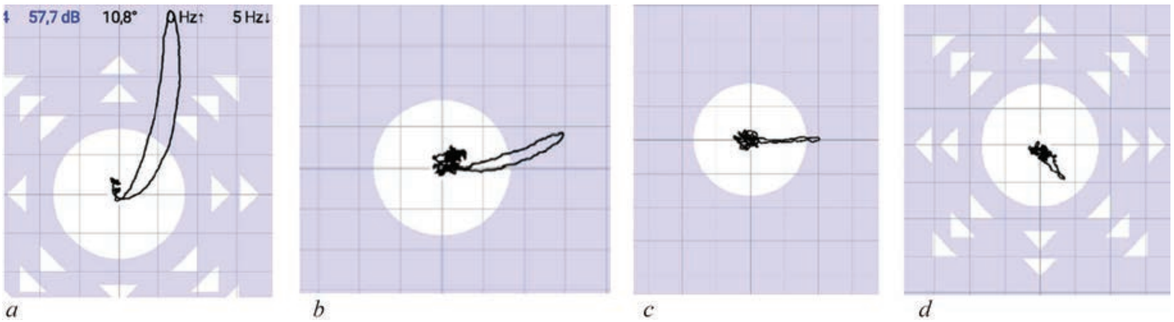

Figure 5. Signals of the MDF 0801 type ECP at an operating frequency of 2 kHz from SS defects (Figure 2) with a flaw depth of location, mm: 1 (*a*); 2 (*b*); 3 (*c*), 4 (*d*); gain ratio for defects with different flaw depths of location, dB: 58 (*a*); 64 (*b*); 70 (*c*, *d*)

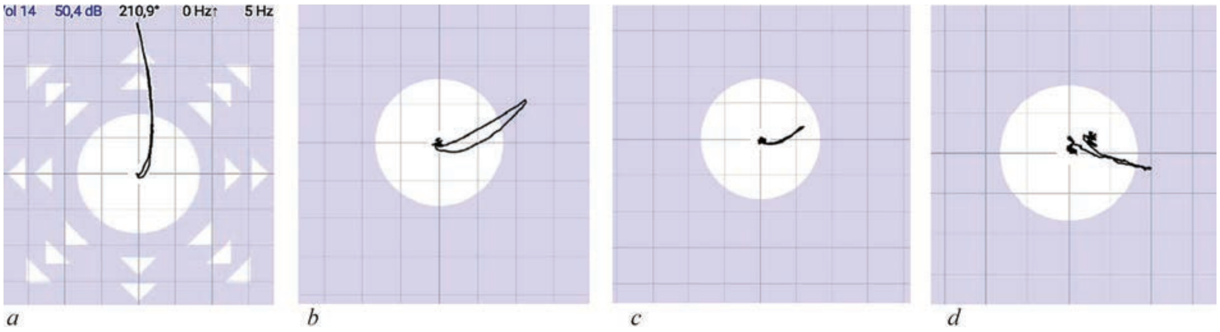

Figure 6. Signals of the MDF 1001M type ECP at an operating frequency of 2 kHz from SS defects (Figure 2) with a flaw depth of location, mm: 1 (*a*); 2 (*b*); 3 (*c*), 4 (*d*); gain ratio for defects with different flaw depth of location, dB: 50 (*a*); 56 (*b*–*d*)

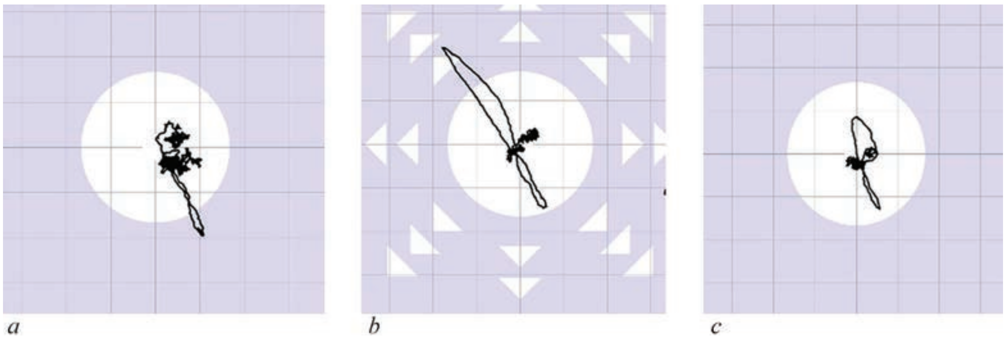

Figure 7. Signals of MDF 0801 (*a*) and MDF 1001M type ECP (*b*, *c*) at an operating frequency of 2 kHz from subsurface local defects of 1.0 mm diameter with a flaw depth of location of 0.6 mm (*a*, *b*) and 1.0 mm (*c*); gain ratio for defects with different flaw depth of location, dB: 66 (*a*); 62 (*b*, *c*)

flat-bottomed holes of 1.0 mm in diameter at different depths was used to simulate subsurface local defects with a flaw depth of location of 0.6 and 1.0 mm. The corresponding signals for the MDF 0801 and MDF 1001M type ECPs at an operating frequency of 2 kHz are shown in Figure 7.

The obtained signals (Figure 7) show that the MDF 0801 and MDF 1001M type ECPs provide detection of a local defect with a diameter of 1 mm. However, the ECP of MDF 0801 type allows identifying only a defect with a flaw depth of location of 0.6 mm (Figure 7, *a*). At the same time, here the signal from a defect is distorted by a high level of noise compared to the signal of the MDF 1001M ECP type from the same defect (Figure 7, *a*).

Summing up the results obtained in Figures 6, 7, it should be noted, that if it is necessary to detect extended and local defects at a greater depth, the preference should be given to the improved MDF 1001M type ECP, which provides a higher level of signals generated by subsurface defects and better noise resistance.

CONCLUSIONS

The features of the design and capabilities of a smartphone-based eddy current flaw detector with the EddySmart application are considered, which in the future can provide remote inspection with wireless transmission of inspection results via mobile communication channels for the further analysis and storage. The prospects for the use of double differential eddy current probes for the inspection of aluminium alloy structure welds were analyzed. The characteristics and results of studies of low-frequency double differential MDF 0801 and MDF 1001M type ECPs with working surface diameters of 8 and 10 mm, respectively, designed to detect defects in welds of aluminium alloys are presented. It is shown that to detect extended and local defects in welds of aluminium alloy structures at a greater depth, the preference should be given to the improved ECP of the MDF 1001M type, which provides a higher signal level and better noise resistance.

REFERENCES

1. Petryk, V., Protasov, A., Galagan, R. et al. (2020) Smartphone-based automated non-destructive testing devices. *Devices and Methods of Measurements,* 11(**4**), 272–278. DOI: https://doi.org/10.21122/2220-9506-2020-11-4-272-278
2. Petryk, V., Protasov, A., Syeryy, K., Povshenko, O. (2019) Use of serial mobile devices in design of portable flaw detectors. *Vcheni Zapysky TNU, Seriya: Tekhnichni Nauki,* 6(**2**), 12–16 [in Ukrainian]. DOI: https://doi.org/10.32838/2663-5941/2019.6-2/03
3. Petryk, V., Protasov, A., Syeryy, K., Ukrainec, S. (2017) Wireless data transmission in ultrasonic nondestructive testing. *Scientific Proc. of STUME, NDT Days 2017, Sozopol*, 216(**1**), 121–123.
4. https://www.lecoeur-electronique.net/us-web.html
5. Zhang, D, Tian, J, Li, H. (2020) Design and validation of android smartphone based wireless structural vibration monitoring system. *Sensors*, 20(**17**), 4799. DOI: https://doi.org/10.3390/s20174799
6. Xie, B., Li, J., Zhao, X. (2019) Research on damage detection of a 3D steel frame model using smartphones. *Sensors,* 19(**3**), 745–762. DOI: https://doi.org/10.3390/s19030745
7. Yu, Y., Han, R., Zhao X. et al. (2015) Initial validation of mobile-structural health monitoring method using smartphones. *Inter. J. of Distributed Sensor Networks,* 11(**2**), 1–14. DOI: https://doi.org/10.1155/2015/274391
8. Meiqin, Z., Weiguo, G., Zhenghao, L., Liu-yang, Z. (2007) Design of remote monitoring system for household applicances and home security based on smartphone. *Measurement and Control Technology*, 26(**8**), 72–75.
9. Felice, M., Heng, I., Udell, C., Tsalicoglou, I. (2021) Improving the productivity of ultrasonic inspections with digital and mobile technologies. In: *Proc. of Conf. on NDE 2019*, *Dec 5–7, Bengaluru, India*. https://www.ndt.net/article/nde-india2019/papers/CP227
10. Mook, G., Simonin, Y. (2018) Eddy current notebook and smartphone. In: *Proc. of 14th Inter. Conf. of the Slovenian Society for NDT*, *Sep 4–6, 2017, Bernardin, Slovenia*. https://www.ndt.net/article/ndt-slovenia2017/papers/135.pdf
11. Mook, G., Simonin, Y. (2018) Smartphone turns into eddy current instrument. In: *Proc. of 12th Europ. Conf. on NDT*, *Gothenburg, Sweden, June 11–15*. https://www.ndt.net/article/ecndt2018/papers/ecndt-0079-2018.pdf
12. Udell, C., Maggioni, M., Mook, G., Meyendorf, N. (2022) *Improving NDE 4.0 by networking, advanced sensors, smartphones, and tablets*: Handbook of Nondestructive Evaluation 4.0. Springer, Cham. Eds by N. Meyendorf, N. Ida, R. Singh, J. Vrana. DOI: https://doi.org/10.1007/978-3-030-73206-6_53

13. Uchanin, V. (2023) Surface eddy current probes of double differential type as an effective tool to solve non-destructive inspection problems. *The Paton Welding J.*, **2**, 46–55. DOI: https://doi.org/10.37434/tpwj2023.02.07
14. DSTU ISO 17643:2015: *Non-destructive testing of welds. Eddy current testing of welds by complex-plane analysis*.
15. Uchanin, V. (2008) Eddy current testing of welded joints. *Tekh. Diagnost. i Nerazrush. Kontrol*, **4**, 71–80 [in Russian].
16. Uczanin, W. (2013) Badania nieniszczące złączy spawanych z wykorzystaniem metody prądów wirowych. *Przegląd Spawalnictwa,* 85(**7**), 25–33 [in Polish].

ORCID

V. Uchanin: 0000-0001-9664-2101,
Ju. Lysenko: 0000-0001-9110-6684

CONFLICT OF INTEREST

The Authors declare no conflict of interest

CORRESPONDING AUTHOR

V. Uchanin
G.V. Karpenko Physico-Mechanical Institute
of the NASU
5 Naukova Str., 79060, Lviv, Ukraine.
E-mail: vuchanin@gmail.com

SUGGESTED CITATION

G. Mook, V. Uchanin, Ju. Lysenko (2024) Studies of eddy current probes for inspection of aluminium alloy structure welds using smartphone-based flaw detector. *The Paton Welding J.*, **12**, 42–48.
DOI: https://doi.org/10.37434/tpwj2024.12.07

JOURNAL HOME PAGE

https://patonpublishinghouse.com/eng/journals/tpwj

Received: 05.07.2024
Received in revised form: 24.09.2024
Accepted: 26.12.2024